Evaluation of the PM4SAND Constitutive Model for the Prediction of Earthquake-Induced & Static Liquefaction in Hydraulic Fills

Master of Science Thesis

By

Aristotelis Tziolas

Student Number: 4631722

Delft, July 9, 2019

Delft University of Technology

Faculty of Civil Engineering and Geosciences

Section Geo-Engineering

TUDelft   **PLAXIS**   Boskalis

Graduation committee:

Prof. dr. M. A. Hicks

Delft University of Technology

Dr. Ir. R.B.J. Brinkgreve

Delft University of Technology

Dr. Ir. C. Kasbergen

Delft University of Technology

Dr. Ir. R. de Jager

Boskalis B.V.

Contents

Acknowledgements

The current report includes the thesis project I conducted at Delft University of Technology to graduate as a Master of Science in Geotechnical Engineering. I would like to take this opportunity to thank several persons who have played a significant role in both the completion of the project and to my professional and academic guidance.

First of all, I would like to thank Boskalis for offering me the opportunity to perform the current master thesis project. Moreover, I would like to thank the committee members starting from my daily supervisor, Richard de Jager, for his valuable advice and for guiding me towards the right direction especially when things were not going as planned. His continuous support played an important role in the proper completion of this project. I would also like to thank Ronald Brinkgreve for providing me with proper instructions and clarifying my questions and doubts regarding the Plaxis software along the entire thesis journey. Furthermore, I would like to thank both Michael Hicks and Cor Kasbergen. Their expertise and professional instructions helped me to raise this project on a higher level.

Finally, I want to thank my parents, my friends from TU Delft and especially my flatmates, Luka and Uros, for their invaluable support and for being always there for me, throughout all good and bad moments of the entire TU Delft journey.

Aristotelis Tziolas,

Delft, July 2019

Abstract

The earthquake-induced liquefaction is a high-risk phenomenon for dredging industries, which need to set strict requirements in order to avoid potential disastrous effects for the project. Different types of liquefaction exist which can be triggered over a wide range of soil types and for different loading conditions. The liquefaction triggering due to an earthquake event is dependent on the soil behaviour under undrained cyclic loading.

The assessment of the liquefaction hazard during an earthquake is mainly based so far on empirical procedures. The most common used in practise is the NCEER method (Youd & Idriss, 2001) which is established according to empirical evaluation of field observations and in-situ testing. However, the NCEER method can be inaccurate for the design primarily due to its empirical nature as it is capturing different soil types and loading conditions. For that purpose, advanced constitutive models can provide more precise assessments as they can be calibrated for specific site conditions. Such a model is the PM4Sand, which is very attractive for practical applications because there are only a few model parameters to be determined in the calibration process.

The first part of the current thesis project includes the validation of the PM4Sand model for both earthquake-induced and static liquefaction according to undrained Cyclic Direct Simple Shear ($CDSS$) tests and undrained Direct Simple Shear (DSS) respectively, performed on Ottawa F-65 Sand. The influence of the model parameters is examined throughout a parametric assessment analysis. It was observed, that the model approximates well the general features of both cyclic and static loading. Regarding cyclic loading, it produced similar responses in terms of excess pore pressures generation and stress paths even though it slightly overpredicts the cyclic resistance for small number of loading cycles and underpredicts the cyclic resistance for large number of loading cycles. Regarding static liquefaction, even if the model had initially overestimated the response, it was able to simulate successfully the static liquefaction behaviour after a recalibration process was established.

The next part of the project includes the performance of the PM4Sand model for the prediction of earthquake-induced liquefaction in hydraulic fills, which are analysed for several different seismic motions. The fill is placed over a different range of relative densities and it is modelled in Plaxis software as a 1-D soil column. The fill layers that are prone to liquefy, are modelled with the PM4Sand model while the layers that are not susceptible to liquefaction are modelled with Hardening Soil Small (HSS) model. The PM4Sand layer is calibrated according to factors that are accounting for the in-situ state of the fill and the magnitude of the earthquake motions. The dynamic analyses are performed with and without consolidation and the lateral boundaries used are tied degrees of freedom. The results in terms of excess pore pressures generation are examined throughout the whole earthquake motion. Moreover, the onset of liquefaction in the hydraulic fill is captured when the excess pore pressure ratio has reached a value of around 1.0 ($r_u \approx 1$).

It is shown, that the PM4Sand model is indeed applicable for the prediction of earthquake-induced and static liquefaction in hydraulic fills. The effect of the in-situ state of the fill, in particular the relative density, has a critical role on the liquefaction susceptibility, which is a lot representative to what has been observed in reality. According to PM4Sand model, the loosely-packed fills ($D_R = $

30% and $D_R = 40\%$) are indeed more susceptible to liquefaction compared to the densely-packed fills ($D_R = 50\%$ and $D_R = 60\%$) which showed less or even no liquefaction potential due to the earthquake events. On the other hand, the largest drawback of the NCEER method it its empirical nature, as for the current project it is proved to be conservative for the design. More specifically, it predicted liquefaction for almost all the hydraulic fills ($D_R = 30\%$ to $D_R = 60\%$) analyzed for all different earthquake motions.

Regarding the dynamic analyses with consolidation, the results related to the earthquake-induced liquefaction of the fills are more representative to realistic conditions as there is a better distribution of excess pore pressures along the soil column with respect to the dynamic analyses without consolidation. For the latter type of analysis, in the loosely-packed fills ($D_R = 30\%$ and $D_R = 40\%$) there is a better diffusion of excess pore pressures more for the signals of low dominant frequencies regardless the peak ground acceleration values of the input signal. In the densely-packed fills ($D_R = 50\%$ and $D_R = 60\%$) the same phenomenon takes pace more for the signals of high dominant frequencies. However, a localization of liquefied zones is observed in distinct parts along the fill layer for the rest of the signals.

Chapter 1: Introduction

1.1 Problem Definition

Liquefaction has been so far one of the major concerns in the area of geotechnical engineering. Loose granular soils tend to contract under cyclic loading induced by earthquake shaking. If the soil is saturated and highly unable to drain, the resulting rearrangement of soil particles can transfer normal stresses from the sand skeleton to pore water. The inability of pore water to flow out causes significant development of excess pore pressures. The result is a reduction in the effective confining stress within the soil and an associated loss of strength and stiffness that contributes to deformations of the soil deposit (Idriss & Boulanger, 2008).

The earthquake-induced liquefaction in hydraulic fills is a well-recognized high-risk phenomenon. Dredging industries need to set strict requirements in order to cope with these risks as liquefaction triggering duo to a seismic event can cause devastating effects to the project. Such a requirement is the high degree of compaction which can result in an over-conservative design and raise significantly the cost of the project. Consequently, in the industry there are several gaps in knowledge on how to achieve optimum design in hydraulic fills. The key question that arises from this master thesis project is how to optimise the design of hydraulic fills subjected to earthquake loading and in order to improve the reliability and overall safety of the structure using finite element software. Better design approaches can minimize the costs and reduce the time required for the completion of the project.

One of the most important available case histories that gave significant insight in the liquefaction triggering of hydraulic fills under seismic loading is the upstream flow failure of the Lower San Fernando Dam. In 1971, after the San Fernando earthquake stroke, a major slide occurred due to liquefaction (loss in strength) of a zone of hydraulic sand fill located within the lower sections of the upstream shell. The fill was mainly consisted of young deposits (looser packing, lower stiffness). A significant remark from this case history is that: very young, very loose, non-plastic or low-plastic soils tend to be more susceptible to significant and rapid strength loss than older, denser, and/or more plastic soils (Robertson P. , 2009).

Another well-documented case history that attracted considerable interest amongst companies regarding the rational design and safe performance of hydraulic fills is the failure of the Nerlerk berm failure. The Nerlerk berm is an underwater hydraulic fill structure designed under inclination to support an offshore drilling platform in the Beautfort Sea. The construction started in 1982 but suddenly interrupted before the berm had reached its required elevation by a rapid failure including the formation of five slides. Hicks & Boughrarou (1998) after performing finite element analysis, concluded that failure occurred under static liquefaction of the berm which is triggered by a combination of rapid sand deposition and limited movements in the weak underlying clay layer. However, what caused much confusion about the berm failure is how liquefaction occurred since its state was not especially loose.

Later, Hicks & Onisiphorou (2005) performed stochastic analysis and found out that a liquefaction failure mechanism triggered due to the arrangement of looser zones within the fill in what was, on average, predominantly dilative. Hence, an important lesson learned is that a dilative fill may also liquefy due to the presence of semi-continuous loose zones arising from deposition-induced anisotropy (Hicks & Onisiphorou, 2005).

The assessment of the liquefaction hazard during an earthquake is mainly based on empirical methods. The most widely used framework for that purpose was provided in the 1996 NCEER and 1998 NCEER/NSF workshops (Youd & Idriss, 2001). This procedure is based on empirical evaluation of field observations and in-situ testing which provides a useful tool for the evaluation of liquefaction susceptibility. However, the largest drawback of the NCEER method is its empirical nature as it is applied for conditions that cover the aforementioned empirical data. Thus, due to the fact that these data account for varying loading condition and different soil types, the NCEER method may be inaccurate and unconservative for the design.

In order to overcome the aforementioned limitations, Finite Element Method programmes appear to be a powerful tool. The FEM software allows for modelling of complex geometries and gives a clear insight in the failure mechanisms and the resulting deformations at both, prior and post failure conditions. The last years several FEM software are being developed for the evaluation of liquefaction potential under seismic loading (e.g PLAXIS UBC3D-PLM) but certain limitations in the accuracy of the solution is encountered.

The PM4Sand is a constitutive model, which as implemented in Plaxis software, is a very useful and powerful tool for that purpose. The PM4Sand model is a sand plasticity model (Boulanger & Ziotopoulou, 2015) which can simulate with high accuracy the response of sands under earthquake loading, including the pore pressure generation and liquefaction phenomena. One of the major advantages of advanced FEM software designed for dynamic loading, such as the PLAXIS PM4Sand, is that they are able to conduct a site-specific analysis.

1.2 Research Questions

The main question of the current master thesis project is:

What are the possibilities of designing hydraulic fills more efficiently against earthquake induced liquefaction by using the PM4Sand constitutive model?

What are the capabilities and the limitations of the PM4Sand model?

The key questions of this project are:

➢ **Is the PM4Sand** model **applicable** for the simulation of <u>earthquake-induced liquefaction</u> in hydraulic fills?

➢ **Is the PM4Sand** model **applicable** for the simulation of <u>static liquefaction</u> in hydraulic fills?

➢ What are the **effects of the in-situ conditions** on the liquefaction triggering in hydraulic fills?

➢ What are the **capabilities and limitations** of PM4Sand model?

Chapter 2: Literature study

2.1 Liquefaction Hazard

2.1.1 Introduction

The liquefaction hazard is a high-risk phenomenon for dredging industries which need to set strict requirements in order to avoid potential disastrous effects for the project. Different types of liquefaction exist which can be triggered over a wide range of soil types and for different loading conditions. In this chapter, the concept of critical state is introduced and the state parameter is presented which gives a clear insight of whether a soil can be susceptible or not to liquefaction. The liquefaction triggering due to an earthquake event is dependent on the soil behaviour under undrained cyclic loading. Accordingly, the criteria used to define liquefaction in laboratory testing are classified either with respect to reaching a specific percentage of shear strain at a given number of loading cycles or based on excess pore pressure evolution after a certain value is reached. The assessment of the liquefaction hazard during an earthquake is so far mainly based on empirical procedures. The most common used in practise is the NCEER method (Youd & Idriss, 2001) which is based on field observations from case histories that suffered from liquefaction. However, the NCEER procedure can be inaccurate due to its empirical nature as it is established with respect to different soil types and loading conditions. For that purpose, advanced constitutive models can provide more precise assessments as they can be calibrated for specific site conditions. Such a model is the PM4Sand which is based on previously developed sand plasticity model by (Dafalias & Manzari, 2004) by incorporating the core of NCEER method. In the PM4Sand version the multiaxial formulation implemented by (Dafalias & Manzari, 2004) is simplified for 2D applications and the model is developed for plane-strain conditions. As a result, there are some limitations which will be investigated along with the capabilities of PM4Sand later on throughout this thesis project.

2.1.2 Types of Liquefaction

In literature, the liquefaction phenomena are mainly divided into two groups: *flow liquefaction* and *cyclic mobility*. These definitions provide important information concerning the conditions of liquefaction triggering.

Flow liquefaction: This type of liquefaction is related to enormous instabilities, known as flow failures and can lead to the most detrimental effects concerning liquefaction phenomena. Such instabilities can be present in sloping grounds. Flow liquefaction is triggered when the static shear stress of a soil body (τ_{static}^{B}) required to sustain equilibrium exceeds the shear strength of the soil in its liquefied state (τ^{D}) (Figure 2.1b). In that case, the large deformations produced by flow liquefaction are actually driven by static shear stresses (Kramer, 1996). This type of liquefaction is characterized by its sudden development where the failure can be extended over large distances.

Cyclic mobility: In contrast to flow liquefaction, cyclic mobility can happen when the static shear stress of a soil mass is lower than the shear strength of the soil in its liquefied state. This

type of liquefaction can occur in granular soils for different in-situ relative densities (loose to dense) and results into large deformations during a seismic event. The produced deformations at failure develop incrementally during earthquake shaking as a result of both static and cyclic loading. The excess pore pressures are evolving until p'=0 is reached (Figure 2.1a). A common type of cyclic mobility is lateral spreading which can develop on gently sloping ground or on virtually flat ground surfaces. If structures are present extreme damage can be caused (Kramer, 1996).

Another type of cyclic mobility is level-ground liquefaction. In that case, static horizontal shear stresses that could cause lateral permanent deformations are absent. The excess pore pressures induced by shaking dissipate by the upward movement of water causing excessive settlements and sand boils. This type of liquefaction is dependent on the time required to reach hydraulic equilibrium and thus, can occur also after the seismic event stops (Kramer, 1996).
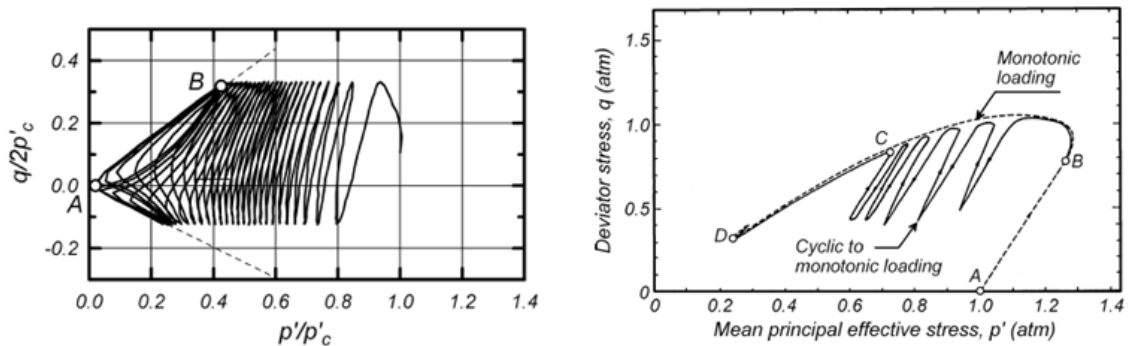
Figure 2.1 a,b: Two different types of liquefaction: a) Cyclic mobility is described by the accumulation of excess pore pressures until p'=0. b) Flow liquefaction is described as sudden loss of shear strength driven by static shear stresses (τ_{static}^{B}> τ^{D}) (Idriss & Boulanger, 2008)

2.2 Principles of Liquefaction

2.2.1 Critical Void Ratio

The determination of critical void ratio (e_{cs}) is of high importance in order to be able to explain the soil behaviour under monotonic (Chapter 2.2.3) and cyclic loading (Chapter 2.2.4). In particular, the state parameter (Ψ) (Chapter 2.2.2) is defined as a function of e_{cs} which will determine whether the soil is susceptible to liquefaction.

The behaviour of sands under monotonic shearing is based on the concept of critical-state theory (Casagrande, 1936). This theory refers to the condition that exists in sand when it is being sheared continuously and no further changes in volume or stress are occurring (Idriss & Boulanger, 2008). The void ratio at this condition is the critical void ratio (e_{cs}) and is uniquely related to the effective confining stress (p'). The relationship between e_{cs} and p' is described by the locus of points which represent all possible combinations between both parameters, named as Critical State Line (CSL) (Figure 2.2). It is important to note that the CSL is not unique but varying for different types of sand.
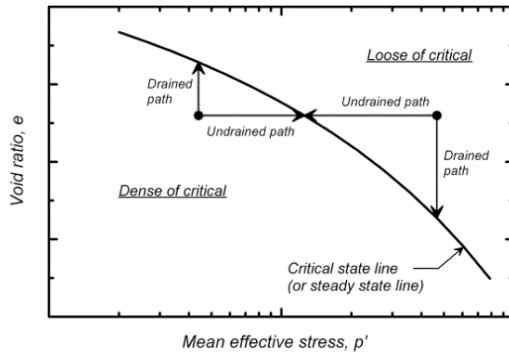
Figure 2.2: Monotonic drained (constant mean effective stress) and undrained (constant void ratio) stress paths towards the critical state line for loose of critical and dense of critical sands (Idriss & Boulanger, 2008)

2.2.2 State Parameter

A common measure for assessing the liquefaction susceptibility of the soil is the state parameter (Ψ) introduced (Been & Jefferies, 1985). The state parameter is defined as $\Psi = e - e_{cs}$ where e is the current void ratio and e_{cs} is the void ratio of the CSL at the same mean effective normal stress (p') (Figure 2.3). In this way, the soil state can be expressed with respect to its CSL. Loose-of-critical soils (contractive) have positive Ψ and may be susceptible to liquefaction (flow liquefaction) while dense-of-critical soils (dilative) have negative Ψ may not be susceptible to liquefaction (nevertheless, cyclic mobility can occur).
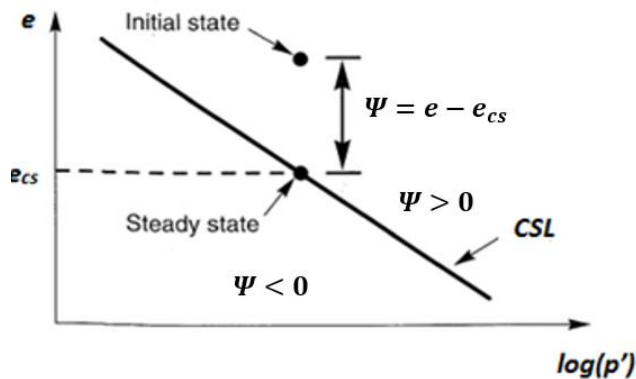
Figure 2.3: State parameter (Kramer, 1996)

2.2.3 Monotonic Loading

In monotonic loading, liquefaction is defined according to the monotonic undrained stress-strain responses (Figure 2.4). The susceptibility of the soil to liquefaction is depending on the sate parameter Ψ. Soil states with $\Psi > 0$ (Figure 2.4 - A) are susceptible to flow liquefaction only if the static shear stress required to sustain equilibrium ($\tau^{(i)}$) exceeds the shear strength

of the soil in its liquefied state ($\tau^{(ii)}$) (Chapter 2.1.2). On the other hand, cyclic mobility can occur in soils with $\Psi < 0$ (Figure 2.4 - B, C).

The representative stress-strain responses for liquefaction under monotonic undrained loading are depicted in Figure 2.4, in which three different failure modes are illustrated: liquefaction (A), dilation (B) and limited liquefaction (C) (Kramer, 1996). The failure mode (A) is also named 'flow liquefaction' in which the soil (very loose) is reaching the peak undrained strength at very low shear strain levels. After this point of instability (i), the response is followed by a sudden collapse and subsequent flow to large strains at a constant liquefied strength under low effective confining stress (critical state). On the other hand, dilation (dense) (B) is characterized by an initial contractive response followed by dilation in which the effective confining stresses are increased for larger shear strains. Apparently, in this failure mode there is no liquefaction occurrence. The failure mode for intermediate densities (C), is named 'limited liquefaction' in which the soil, after reaching the peak undrained strength at low strain levels (point of instability i) is followed by a short period of strain-softening response after which dilation occurs at intermediate strains.
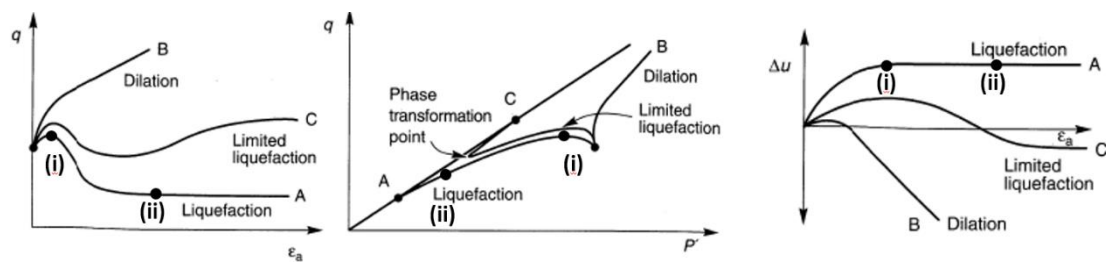
Figure 2.4: Three different types of monotonic undrained failure: Liquefaction (A), Dilation (B) and Limited Liquefaction (C), (Kramer, 1996)

2.2.4 Cyclic Loading

The liquefaction triggering of a soil under cyclic undrained loading arising from a sudden earthquake event is dependent on the soil behaviour throughout this event. The behaviour is dominated by the soil density, as loose granular soils are highly prone to liquefaction. For loose soils ($\Psi > 0$), the liquefaction triggering implies continuous contractive behaviour which is restrained by the phase transformation line (PT) (Chapter 2.7.1). When the stress state is reaching that line, the behaviour switches from contractive to dilative. After this point, there is a significant loss of stiffness and a gradual shear strain accumulation.

In laboratory testing, the liquefaction triggering under cyclic loading is defined according to two criteria. The first one indicates, that liquefaction is triggered after a specific percentage of strain is reached. An axial strain of 5% double-amplitude (ε_α^{DA}) is commonly adopted for Cyclic Triaxial tests (ICU) whereas in Cyclic Direct Simple Shear (CDSS) tests, a shear strain of 3% single-amplitude is used. The second criterion is based on the r_u parameter which is

defined as the generation of excess pore water pressure (Δu) normalized by the minor effective consolidation stress (σ'_{3c}) in a triaxial test.

$$r_u = \frac{\Delta u}{\sigma'_{3c}} \qquad (2.1)$$

For Cyclic Direct Simple Shear (CDSS) tests, the definition of r_u is similar in which the consolidation stress from eq.(2.1) is replaced by the vertical effective stress.

The r_u parameter can reach a maximum value of 1.0 when the excess pore pressure is approaching 100% of the initial confinement ($\Delta u = \sigma'_{3c}$). At that point, the shear strength of the sand specimen is diminished and ''initial liquefaction'' occurs (Seed & Lee, 1996). However, the $r_u = 1.0$ condition cannot be reached for all type of soils. In sandy silts or silty sands the r_u can reach a value of 0.90 to 0.95 resulting in a significant softening response ($>$ 5% axial strains of double-amplitude) which corresponds to 'initial liquefaction' (Ishihara, 1996). Moreover, in dense sands, the $r_u = 1.0$ condition may never be reached as it is less prone to liquefy due to higher strength.

It is important to note that the aforementioned values are not used as strict measures but as an index to define liquefaction and therefore can vary in the literature.

For the evaluation of the liquefaction potential, the cyclic induced shear stress is commonly expressed in terms of Cyclic Stress Ratio (CSR). In Cyclic Triaxial tests, CSR is defined as the maximum cyclic shear stress ($q_{cyc}/2$) divided by the isotropic consolidation stress (σ'_{3c}).

The cyclic shear strength of sands can be described by the Cyclic Resistance Ratio (CRR) which is termed as the CSR required to reach liquefaction for a specified number of loading cycles. In general, CRR depends on the amplitude and the frequency of loading. A larger CRR implies that fewer number of loading cycles are required to trigger liquefaction ($r_u = 100\%$ or $\gamma_{cyc} = 3\%$) (Figure 2.5)

Furthermore, in laboratory testing, the fabric of the soil sample plays an important role in the liquefaction triggering under cyclic loading (Nemat & Tobita, 1982). The fabric depends on the preparation method (inherent anisotropy) and on whether or not the sample has been pre-strained. If the strain levels under drained cyclic loading are such that volumetric expansion occurs, the sample shows decreased liquefaction resistance in cyclic undrained loading. In addition, the sample preparation method (fabric) combined with a particular loading path may result in different liquefaction resistances (e.g higher CRR in triaxial loading and significantly lower CRR in simple shear loading).
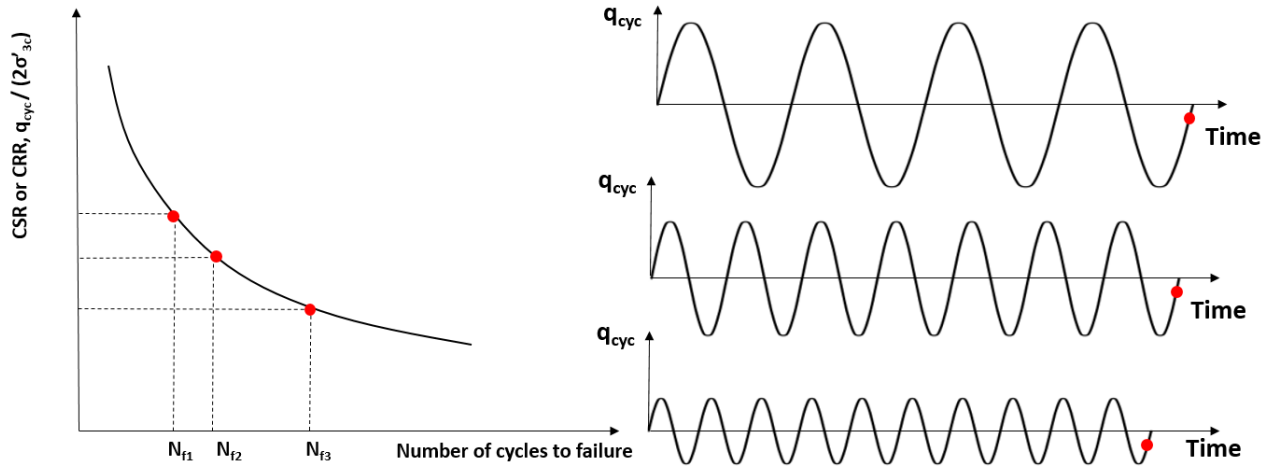
<u>Figure 2.5:</u> Cyclic strength curve of sand (left) after the conduction of three cyclic triaxial tests of the same volumetric and stress state (D_R, σ'_{3c}). The tests are performed for different cyclic stress amplitudes (right).

2.3 Simplified Procedure for the Simulation of Earthquake Loading

2.3.1 Introduction

In the 1996 NCEER and 1998 NCEER/NSF workshops (Youd & Idriss, 2001), a widely used method for the assessment of the liquefaction resistance of soils under level to gently sloping ground was constituted. The procedure is based on empirical evaluation of field observations, laboratory and in-situ testing. The NCEER method requires the determination of two parameters in order to evaluate the cyclic resistance of soils: the Cyclic Stress Ratio (CSR) (Chapter 2.3.2) and the Cyclic Resistance Ratio (CRR) (Chapter 2.3.3).

The shear stresses induced by earthquake loading in a soil body below a depth z can be estimated using the simplified procedure proposed by (Seed & Idriss, 1971). The subsurface is simplified as a soil column of unit width and length which behaves as a rigid body (Figure 2.7). The earthquake induced shear stresses are calculated by the following expression:

$$\tau_{max} = F = ma = \frac{W}{g}a_{max} = \frac{\gamma z}{g}\alpha_{max} = \sigma_{vo}\frac{\alpha_{max}}{g} \qquad (2.5)$$

where F: horizontal seismic force, m: total mass of soil column, a_{max}: maximum horizontal acceleration at the ground surface, W: weight of the soil column, γ: average total unit weight of the soil above depth z and σ_{vo}: total vertical stress at the same depth.

It is clear, that the simplified procedure assumes a constant distribution of both peak horizontal acceleration (a_{max}) and stress ratio (τ_{max}/σ'_{vo}) along the soil column (Figure 2.6). However, this assumption is not the case in reality because it does not take into account the subsurface ability to deform.
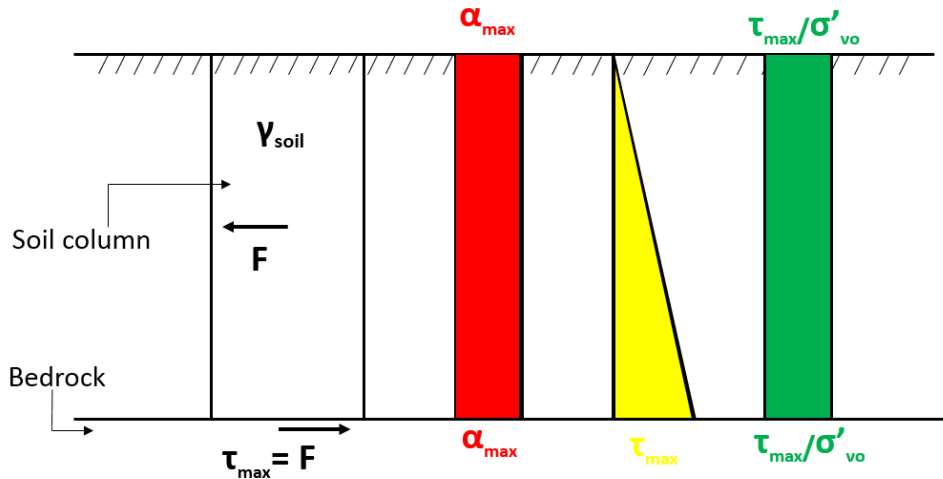
Figure 2.6: Simplified representation of earthquake loading along a soil profile

2.3.2 Cyclic Stress Ratio (CSR)

The CSR represents the dynamic stress conditions induced by the earthquake and is calculated as the normalized cyclic horizontal shear stress (τ_{cyc}) by the vertical effective overburden stress (σ'_{vo}):

$$CSR = \frac{\tau_{cyc}}{\sigma'_{vo}} \qquad (2.6)$$

The CSR can be calculated by the following expression (Idriss I. , 1999)proposed by (Seed & Idriss, 1971):

$$CSR = \frac{\tau_{cyc}}{\sigma'_{vo}} = 0.65 \frac{\tau_{max}}{\sigma'_{vo}} = 0.65 \frac{\sigma_{vo}}{\sigma'_{vo}} \frac{\alpha_{max}}{g} r_d \qquad (2.7)$$

where τ_{max} is the peak cyclic shear stress induced by earthquake, σ_{vo} and σ'_{vo} are the vertical total and effective overburden stress respectively, α_{max} is the maximum horizontal acceleration at the ground surface, g is the gravity acceleration and r_d is a stress reduction coefficient. The variation of r_d with depth for earthquakes with different magnitude can be calculated based on expressions proposed by (Idriss I.M, 1999)(Appendix A.2)

2.3.3 Cyclic Resistance Ratio (CRR)

The CRR is described as the capacity of soil to resist liquefaction or as the cyclic stress ratio required to trigger liquefaction. In particular, CRR is the required CSR to trigger liquefaction at a certain number of loading cycles.

The Cyclic Resistance Ratio (CRR) against liquefaction triggering is most commonly estimated based on in-situ tests with case-history-based liquefaction correlations (Idriss & Boulanger, 2008). The CRR curve is described as the boundary line that separates the figure into two areas that are indicating either liquefaction or non-liquefaction occurrence (Figure 2.7).

The CRR curve is illustrated in terms of either SPT or CPT penetration resistance. In the first case, it is represented as a function of the parameter $(N_1)_{60}$ (Seed & De Alba, 1986) which stands for an SPT blow count normalized to an overburden pressure of approximately $100 kPa$ and a hammer efficiency of 60%. Regarding Cone Penetration Tests, the CRR curve is determined from the normalized, dimensionless and corrected CPT resistance q_{c1N} (Robertson & Wride, 1998) for clean sands. It is important to note, that these are standard curves and correction factors need to be applied (see following sections).
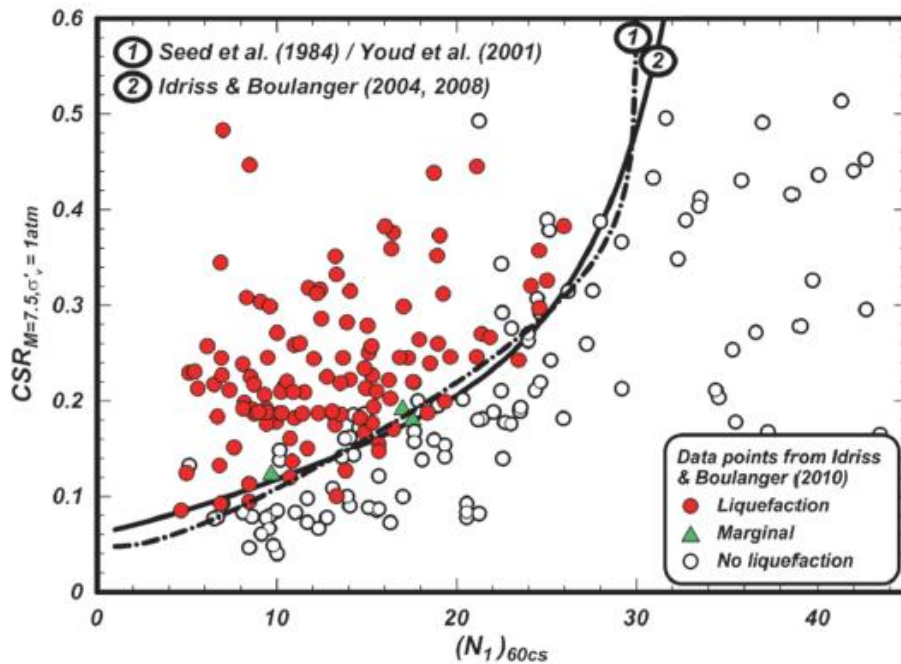
Figure 2.7: Liquefaction curve representing the boundary regarding occurrence and non-occurrence of liquefaction for different combinations of Cyclic Resistance Ratio (CRR) based on SPT data for different combinations of CRR and $(N_1)_{60}$. (Idriss & Boulanger, 2008) for an earthquake of 7.5 magnitude.

2.3.4 Correction Factors

MSF correction factor

In order to convert the CRR curves to a magnitude different than 7.5, (Idriss, 1999) proposed the following relation that connect the so-called Magnitude Scale Factor (MSF) for sands to the earthquake magnitude M:

$$MSF = 6.9\exp\left(-\frac{M}{4}\right) - 0.058 \leq 1.8 \quad (2.8)$$

K_σ correction factor

The CRR of sand depends on the effective confining stress (σ'_{vc}) because the latter accounts for the tendency of sand to contract or dilate. Based in previous research (Vaid & Sivathayalan, 1996), it is proven that that the CRR is decreased with an increasing confining

stress for a given value of relative density (or for a given value of relative state parameter in Chapter 2.2.2).

This effect of overburden stress can be captured by the K_σ correction factor introduced by (Seed, 1983) as:

$$K_\sigma = \frac{CRR_{\sigma'_{vc} \neq 1\,atm}}{CRR_{\sigma'_{vc} = 1\,atm}} \quad (2.9)$$

where σ'_{vc} is the effective confining stress.

$\underline{K_\sigma\ \text{correction factor}}$

The CRR of sand is highly affected by the presence of initial static shear and can be captured by the following correction factor proposed by (Seed, 1983):

$$K_\alpha = \frac{CRR_{\alpha \neq 1}}{CRR_{\alpha = 0}} \quad (2.10)$$

where α is the static shear stress ratio defined as:

$$a = \frac{\tau_s}{\sigma'_{vc}} \quad (2.11)$$

where τ_s is the horizontal shear stress

Later, Boulanger (2003a) showed that K_α can be related to the sand's state as it depends on both relative density (D_R) and confining stress (σ'_{vc}) which are both accounting for the dilative tendency of sand (Figure 2.8). The effect of relative density is attributed to the fact that sand is more strongly dilatant in shear as D_R is increased (at the same σ'_{vc}). The effect of confining stress (σ'_{vc}) is attributed to the fact that sand is more strongly dilatant in shear at the lower confining stresses (for the same D_R).

Hence, the correction factor K_α bridges cyclic and monotonic behaviour, or cyclic mobility and flow liquefaction. This factor, which is applied when the presence of initial static shear stress is presented, is used e.g in slope geometries. In case of very loose sands, for an increasing slope angle the failure is dominated by flow liquefaction as the soil is becoming weaker. On the other hand, in case of very dense sands, the failure is dominated by cyclic mobility as the soil is becoming stronger.

2.3.5 Simplified Liquefaction Triggering Assessment

The susceptibility of a soil to liquefaction can be assessed according to (Seed & Idriss, 1971) in terms of the factor of safety (FS). This factor is defined as the ratio between the liquefaction resistance (CRR) to the seismic induced loading (CSR) as:

$$FS = \frac{CRR}{CSR} \quad (2.12)$$

In case $FS < 1$, the soil's potential to liquefaction is high. In the aforementioned equation, the CRR is dependent on factors concerning the earthquake magnitude (MSF), the confinement level (K_σ) and sloping ground effects (K_α) as:

$$CRR = CRR_{7.5} \cdot MSF \cdot K_\sigma \cdot K_\alpha \quad (2.13)$$

2.4 Correlation between CRR from Lab Tests to Field Conditions

The different states of consolidation stress measured in Cyclic Simple Shear and Cyclic Triaxial (ICU) tests are the cause of differences in the measured CRR. The CRR of anisotropically consolidated specimens ($K_o \neq 1$) can be related to the CRR of isotropically consolidated specimens ($K_o = 1$) by the relationship proposed by (Isihara, 1985) (Appendix A.1 – eq.(A.9)).

The relation between the CRR from a simple shear test to the CRR from the Triaxial test (ICU) can be calculated according to (Idriss & Boulanger, 2008) (Appendix A.2 – eq.(A.10)).

When a second direction of cyclic loading is added, the CRR decreases by $10 - 15\%$, as summarized by (Pyke , Chan, & Seed, 1974) and (Isihara, 1996). For level ground conditions, the earthquake loading is best approximated as a two-directional simple shear loading, so the CRR from a unidirectional simple shear test would be reduced by 10% to represent in-situ conditions. The relationship between in-situ CRR_{field} and either CRR_{TX} or CRR_{SS} can be computed according to (Appendix A.2 – eq.(A.11-A.12)).

2.5 Hydraulic Fill Structure

2.5.1 Introduction

Land reclamation is generally defined as the process of raising the elevation of a seabed or riverbed to a level in which water is being replaced by dry soil in order to create a new land (Van't Hoff & Nooy van der Kolff, 2012). This method has been undertaken in different parts of the world aiming to substantially increase the amount of land that is available for various activities due to significant increase in world's population, rise of sea levels (global warming) and upraising energy demand. Land reclamation can be implemented in various projects ranging from onshore to offshore applications. Related examples are the expansion of commercial and industrial activities such as ports (Port of Rotterdam), airports (Kansai International Airport in Japan) and the construction of artificial islands on the ocean (Palm Island in Dubai).

There are many different methods that can be used for land reclamation purposes. These methods can be divided mainly into two types, the *filling* and *non-filling*. The filling type can be categorized into *dry earth movement* and *hydraulic filling*. The current research is mainly focused on the *hydraulic filling* method.

The hydraulic filling method can be achieved either underwater or above water. Underwater placement methods provide a lower relative density ($D_R < 50\%$) than the placement methods used above the water level ($D_R > 50\%$). Hence, for underwater placement the fill can be more susceptible to liquefaction (looser-packing, lower stiffness).

2.5.2 Hydraulic Filling Method

The hydraulic filling method aims to create new land by raising the ground level from below water to a surface with dry land. This procedure of new land creation is achieved by applying the following steps (Van't Hoff & Nooy van der Kolff, 2012):

- Acquisition of the fill material (mainly granular soil) from either borrow or dredging area which is proximate to the site. The latter case is undertaken by floating equipment (dredgers)
- Transportation of the fill mass from the borrow area to the project site by dredger, barge or pipeline
- Placement of the construction material based on soil flow. The flow is accommodated by the use of (processed) water by which a soil mixture is created. This mixture can be pumped and lied on the seabed according to the current conditions

2.5.3 In-situ Conditions of the Reclamation Structure / In-situ Volumetric State (D$_r$)

It is of high importance to determine the in-situ conditions and the intrinsic properties of the hydraulic fill structure. The anticipated geometry as well as the in-situ relative density need to be assessed. This will provide the appropriate information to be used as an input in the PM4Sand model.

The most common framework used for the assessment of the relative density is the indirect methods based on in-situ testing (CPT and SPT). Over the years, several correlations have been established to relate the cone resistance (q_c) as well as the blow counts (N_{SPT}) with the relative density. For Standard Penetration Tests (SPT), the number of blow counts (N_{SPT}) is used to estimate the relative density of sands or gravels according to British Standard classification (Table 2.3).

Description	BS5930 N_{SPT}		ISO14688 D_r	
	From	To	From	To
Very loose	0	4	0	15
Loose	4	10	15	35
Medium dense	10	30	35	65
Dense	30	50	65	85
Very dense	50	-	85	100

Table 2.3: Relative density in relation to N_{SPT} (Van't Hoff & Nooy van der Kolff, 2012)

The relative density of a hydraulic fill before compaction is highly influenced by its placement method. The disposal energy plays an important role in the resulting density of the fill. In particular, higher densities can be achieved by raising the disposal energy which leads to better compaction. In Table 2.4 several placement methods with the corresponding ranges of relative densities for silica sands are indicated.

Placement methods	Relative density D_r (%)
Saturated soil	
Discharged under water (spraying)	20-40
Discharged under water (dumped)	30-50
Discharged under water (overflow)	20-40
Discharged under water (rainbowing)	40-60
Discharged over water (free flow through pipe)	60-70
Discharged over water (rainbowing)	60-80
Inside a big hopper	30-50
Inside a small hoper	10-30
Dry soil	
On dump truck (filled from a funnel)	10-20
On the discharge area (compacted by bulldozers)	50-60
On the discharge area (compacted by compacting equipment)	Up to 100

Table 2.4: Relative densities of a hydraulic fill achieved over different placement methods (Van't Hoff & Nooy van der Kolff, 2012)

2.5.4 Placement Methods

The procedure of hydraulic fill placement can be divided into four types. Each type is briefly described in this section. More detailed information about technical specifications regarding fill placement can be seen in the book: ''Hydraulic fill manual'' (Van't Hoff & Nooy van der Kolff, 2012)

Underwater placements in bulk of fill material (dumping) (Dr=30-50%)

The filling process is guided by $TSHDs$ vessels or barges. The soil is loaded into the vessels and subsequently transported to the reclamation area. Then, the soil mixture is dumped through the bottom doors of the $TSHD$ and consequently falls down towards the seabed. After this step, the surrounding water will dilute the mixture during its route to the seafloor, hence lowering its concentration and increasing the seabed area that will be covered by dumped material. It is important to note, that due to the low relative densities provided by this placement method, the fill material may likely be susceptible to liquefaction

Rainbowing (Dr=40-60% under water, Dr =60-80% over water)

This technique is often preferred in shallow locations where water depths are limited for access by $THSDs$. In that case, a suction hopper dredger can rather approach the designated area. The fill mixture is pumped and sprayed from the dredger resulting in a rainbow arch

which can reach distances up to $150m$. Beach replenishment/recreation, port expansion and artificial islands are the major reclamation applications related to this method.

Placement of fill material using a discharge pipeline (Dr=60-70% over water)

The discharging pipeline method is the most common technique used for reclamation. Pumping through steel pipelines is applied for reclamation above water in areas which are out of reach of rainbowing. The pipeline may be assisted by pontoons or floating jackets with the latter connecting the transportation vessels with the reclamation area (Van't Hoff & Nooy van der Kolff, 2012). The fill material is gently distributed towards the seabed.

Spraying (Dr=20-40% under water)

This method is applied in case of soft subsoil conditions where lower shear strengths are present. The soil mixture is sprayed smoothly, preventing mud wave formation, instabilities or inclusions of soft soil deposit and within the fill structure. Spraying is also used when the sand has to be placed accurately within predefined boundaries according to slope design requirements. In the present research, this method is not considered as fill is underlain by bedrock.

Figure 2.21: The rainbowing method of placement (Van't Hoff & Nooy van der Kolff, 2012)

2.6 A Sand Plasticity Model Accounting for Fabric Change Effects

2.6.1 Model Description

PM4Sand is a stress-ratio controlled, critical state compatible, sand plasticity model applied for earthquake geotechnical engineering as described by (Boulanger & Ziotopoulou, 2015). The formulation of the model is based on previous works from (Dafalias & Manzari, 2004) which incorporates the dependence of fabric and fabric evolution on previous loading history. One of the main assumptions is that only changes in stress-ratio can produce plastic strains.

Moreover, PM4Sand is an effective stress model which accounts for the generation of excess pore pressure under undrained cyclic loading and the progressive increase in shear strain accumulation after a specific value of excess pore pressure ratio is reached. In the following sections a short introduction regarding the formulation of the model from (Dafalias &

Manzari, 2004) is elaborated and in Chapter 2.7 the PM4Sand model is described as implemented in Plaxis 2D software. The detailed description of the (Dafalias & Manzari, 2004) model can be found in Appendix B. It is important to note, that PM4Sand is a simplification of the aforementioned model and has some limitation as it is implemented for 2D applications only.

2.6.2 Conceptual Desription

The elastic response of the (Dafalias & Manzari, 2004) model is defined with respect to the yield surface. The yield surface is represented as a linear wedge in the $q - p$ space (Figure B.1). The elastic response is depending on the density and the stress state below the yield surface through the elastic modulus. (eq. B.1-B.4)

The model also embodies bounding (M^b), dilatancy (M^d) and critical surfaces (M) (Figure B.1). These surfaces are defined in such a way that are dependent on the soil state through the state parameter Ψ (Chapter 2.2.2). During the loading process the quantities M^b and M^d are varying according to the soil state in order to have $M^b = M^d = M$ when the critical state condition is reached (Chapter 2.2.1). Moreover, for a denser-than-critical state $(\Psi < 0)$ one has $M^d < M < M^b$ while for a looser-than-critical state $(\Psi > 0)$ one has $M^d > M > M^b$ (eq. B.7-B.8)

The bounding surface (M^b) represents the onset of softening behaviour and the progressive soil shearing towards critical state. In dense sands, the stress state is reaching the bounding surface to represent the explicit peak in hardening which is followed by sudden softening. On the other hand, in loose sands, the bounding surface lies on or close to the critical surface (M) so as to show hardening behaviour towards failure without any dilation.

The dilatancy surface (M^d) represents the boundary between contractive and dilative volumetric behaviour, also called as phase transformation line (PT) (Chapter 2.2.4). In dense sands, this surface lies below the critical surface (M) in which the dilation leads to a peak behaviour. On the other hand, in loose sands, the dilatancy surface lies close or on to the critical surface because there is no dilation.

The critical state surface (M) represents the stress ratio at which $\Psi = 0$ (or $e = e_c$)(eq. B.6). After this state is reached, the soil deforms continuously under constant volume which represents an ultimate strength state for large strains (Chapter 2.2.1).

The model accounts for hardening and softening by kinematic rotation of the yield surface in the stress space. This is accompanied by the plastic modulus H (Chapter B.5). For stress states above the bounding surface $(H < 0)$ softening occurs whereas for stress states below the bounding surface $(H > 0)$ hardening occurs. The amount of hardening or softening is depending on the distance of the current stress state to the bounding surface (eq. B.10). More specifically, the larger the distance, the higher the amount of hardening or softening.

Monotonic Loading

In order to get a better understanding on how the model works, both drained (TSP) and undrained (ESP) stress paths for a dense-of critical ($\Psi < 0$) and a loose-of-critical ($\Psi > 0$) soil element confined under mean effective stress p'_o are illustrated in Figure 2.22.

In monotonic drained loading (TSP), as long as the stress state η lies inside the yield surface only elastic strains are produced for a change in stress-ratio ($d\eta \neq 0$). When the stress state crosses the yield surface with $d\eta > 0$, then plasticity occurs. Meanwhile, the stress state is lying below the bounding surface ($H > 0$), so hardening behaviour is observed.

Initially, the quantity H is large since the distance of the stress state to the bounding surface is also large and therefore, the plastic strains are limited. The dense-of critical element has a higher H since from eq.(B.11) the void ratio e is lower. As the loading increment $d\eta$ further increases, H is decreasing (increasing void ratio) which represents less hardening behaviour towards critical state. Furthermore, the yield surface is moving upwards (increase in a) so as η to remain on $f = 0$ (kinematic and isotropic hardening) and the absolute value of Ψ is decreasing for both soil elements (eq. B.6).
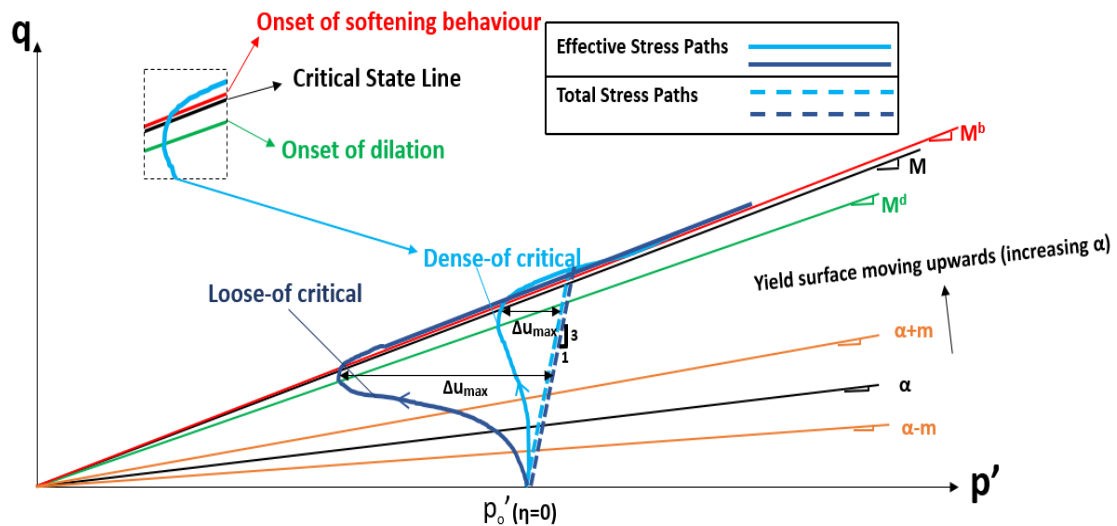
Figure 2.22: Monotonic stress paths for dense-of-critical and loose-of-critical soil element.

Similarly, the response is only elastic for stress states inside the wedge until the yield surface is crossed again where plasticity occurs. As the yield surface is moving towards critical state the amount of induced plastic strains is increasing since the distance between the bounding surface (M^b) and the stress state is becoming smaller. During the aforementioned stages, the response is contractive since the stress state is below the dilatancy surface (M^d). When the stress state crosses the dilatancy surface M^d the response transitions from contraction to dilation. Furthermore, at the point where the stress state overpasses the bounding surface M^b, $H < 0$ and thus, softening behaviour is observed. If the loading is to be continued, critical state is reached as $\Psi \to 0$ and $M^b, M^d \to M$.

In monotonic undrained loading (ESP) the same logic applies for elasticity and plasticity in the stress paths. However, the rate with which the plastic strains are being generated is different. The reduction of mean effective stress dp' is larger in the loose-of-critical element as a result of higher excess pore pressure generation. The plastic modulus H is reduced more rapidly because the stress state is approaching faster the critical state line than in the dense-of-critical element. Therefore, the loose-of-critical element produces plastic strains faster.

<u>Fabric Effects</u>

One of the main limitations of the previous version of the (Dafalias & Manzari, 2004) model is that the decrease of effective stresses towards $p' = 0$ during cyclic loading was not well captured with the stress-path loops being disturbed before reaching that state. That is because the model didn't account for the significant changes in fabric during the dilatant phase of plastic deformation, which has a significant effect on the contractive response upon reversal of loading (Dafalias & Manzari, 2004).

The latest addition of the model enhances to overcome this limiation by introducing the fabric dilatancy tensor $\boldsymbol{z}$ which evolves as follows:

$$dz = -c_z \langle -d\varepsilon_v^{pl} \rangle (sz_{max} + z) \tag{2.14}$$

Also the parameter A_d that accounts for dilatancy d (eq. B.12) is modified as:

$$A_d = A_o(1 + \langle sz \rangle) \tag{2.15}$$

where z_{max} is the maximum value of z, c_z controls the evolution of z, A_o is a constant, $s = \pm 1$ according to $\eta = a \pm m$, $z = 0$ (initially) and $<>$ are MacCauley brackets setting negative values to zero.

In undrained loading (eq. B.13), for a given K and H, an increase in the reduction of p requires an increase in d. This increase in d is required for the proper simulation of effective stress reduction and modulus degradation under undrained cyclic loading (Dafalias & Manzari, 2004).

<u>Cyclic Loading</u>

During loading from $\eta = 0$ with $d\eta > 0$ (Figure 2.23), the response is contractive ($d\varepsilon_v^{pl} > 0$) as long as $\eta < M^d$. This yields $dz = 0$ because $\langle -d\varepsilon_v^{pl} \rangle = 0$. When $\eta > M^d$, considering eq.(B.12) and eq.(B.2)$_2$, the response is switching to dilative ($d\varepsilon_v^{pl} < 0$) and eq.(2.14) is activated giving $dz = -c_z |d\varepsilon_v^{pl}|(z_{max} + z) < 0$. As long as the stress state is at $\eta = \alpha + m$, eq.(B.4) yields $A_d = A_o$ because $\langle sz \rangle = \langle +z \rangle = 0$. When a loading reversal occurs (i.e $d\eta < 0$ at $\eta = \alpha - m$), then $s = -1$ and $\langle sz \rangle = \langle -z \rangle = |z|$ which gives $A_d = A_o(1 + |z|)$. This increase in A_d will enhance the dilatancy d in eq.(B.12) and result in the reduction of p in eq.(B.13). At the same time, $d\eta < 0$ will produce plastic strains according to eq.(B.2).

Upon new reversal (i.e $d\eta > 0$ at $\eta = \alpha + m$) the response is contractive ($d\varepsilon_v^{pl} > 0$) and similarly $z < 0$ and eq.(2.14) is once again deactivated yielding $dz = 0$ until the next dilative response in triaxial extension. Hence, in each increment of $d\eta$ upon reversal which exhibits dilative behaviour, A_d is increased from A_o to $A_o(1 + |z|)$, then decreased back to A_o and eventually increased again due to the evolution of the fabric-dilatancy tensor z. Note that, A_d will remain constant for any loading in the contractive region ($d\varepsilon_v^{pl} > 0$).
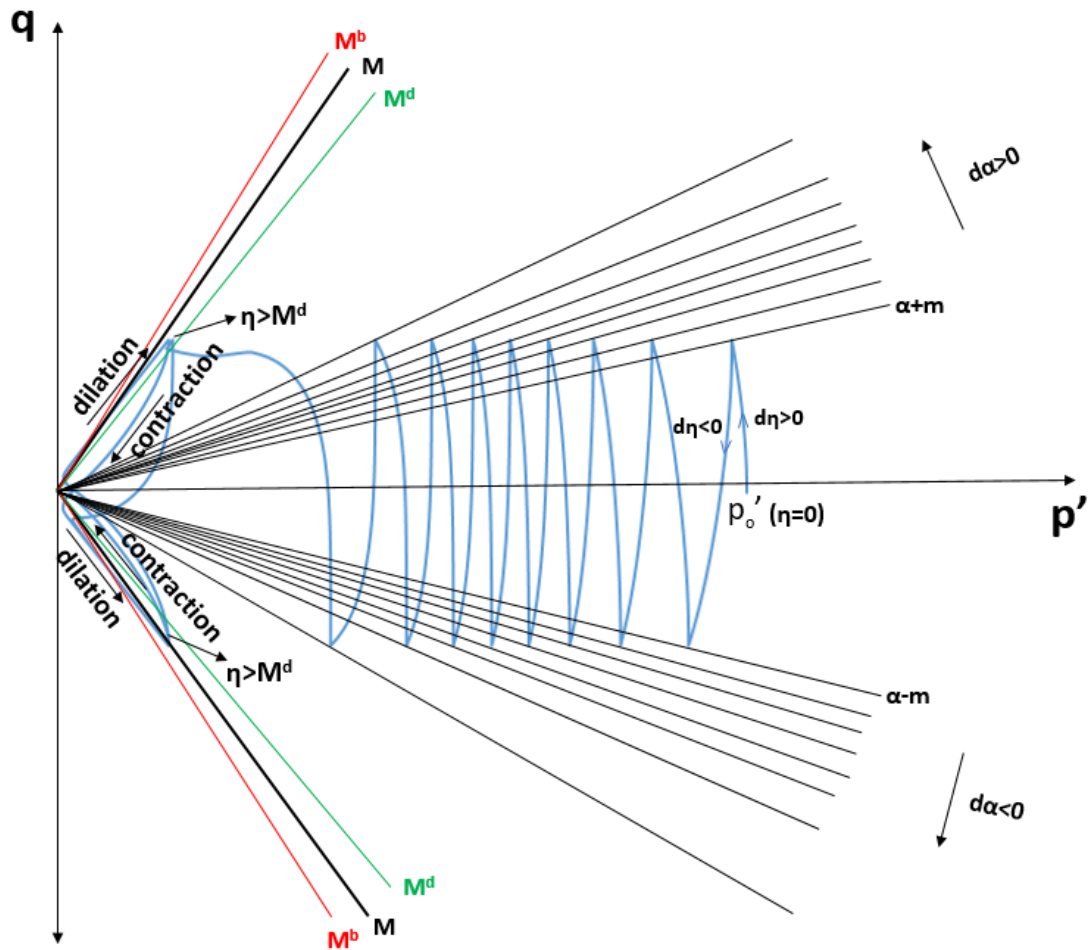
Figure 2.23: Cyclic undrained stress path of a soil element.

Multiaxial Formulation

The bounding surface model implemented by (Dafalias & Manzari, 2004) can capture loading conditions in triaxial compression and extension in which the major principal stress direction is vertical and horizontal respectively. However, it is known that the principal stress direction within a soil mass is different from element to element. After the construction of an embankment (Figure 2.24), the major principal stress direction (σ_1) is varying from vertical

(triaxial compression) to horizontal (triaxial extension) along the slip surface.   The aforementioned principal stress rotation is accompanied during an earthquake event as well.
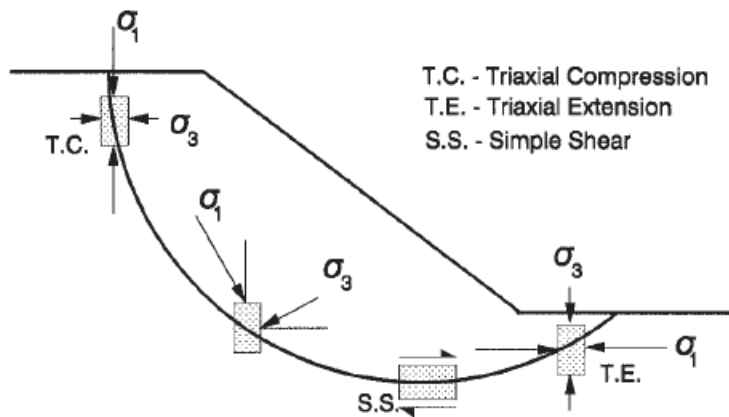
Figure 2.24: Limiting equilibrium stress conditions in an embankment.

Furthermore, most sands have anisotropic strength characteristics (Saada, 1988) also known as stress-induced anisotropy.   Under three-dimensional stress conditions, this type of anisotropy is dependent on many factors such as: the major (σ_1), intermediate (σ_2) and minor (σ_3) principal stresses, the inclination of the major principal stress direction (σ_1) to the vertical, the deviator stress $(\sigma_1 - \sigma_3)$ and the mean normal stress $\left(\frac{\sigma_1+\sigma_2+\sigma_3}{3}\right)$ (Uthayakumar & Vaid, 1998).

In order to capture the three-dimensional stress conditions, the model is generalized in multiaxial stress space (Dafalias & Manzari, 2004).   In this formulation, the stress-ratio is generalized by the deviatoric stress ratio.

2.7 PM4Sand Constitutive Model

2.7.1 Model Description

The PM4Sand model is a simplification of the multiaxial formulation of the sand plasticity model developed by (Dafalias & Manzari, 2004) and is implemented in plain-strain conditions (2D model). The surfaces (Figure 2.25) are simplified by removing the Lode angle dependency in such a way that the same friction angles are used for both compression and extension. Consequently, the model has some limitations and is only applicable to plane-strain problems as the various relationships are implemented in terms of in-plane stress only.

2.7.2 Critical State Soil Mechanics Framework

The PM4Sand model is implemented according to critical state soil mechanics framework (Bolton, 1986). In this formulation, the relative state parameter ξ_R (Boulanger, 2003a) is used instead of the parameter Ψ (Been & Jefferies, 1985). The ξ_R is the state parameter Ψ (eq.(B.6)) normalized by the difference between the maximum void ratio (e_{max}) and the

minimum void ratio (e_{min}) that are used to define relative density (D_R). This provides improved correlation regarding the shearing behaviour of sands (Konrad, 1988).

Therefore, the critical state line is 'empirically' determined according to the following equation:

$$D_{R,CS} = \frac{R}{Q - ln\left(100\frac{p'}{p'_A}\right)}$$

(2.16)

The relative state parameter ξ_R is simply defined as the difference between the relative density at critical state ($D_{R,CS}$) and the current relative density (D_R) as:

$$\xi_R = D_{R,CS} - D_R$$

(2.17)

Regarding eq.(2.16) and eq.(2.17): p' is the current mean effective stress and p_A is the atmospheric pressure. The parameters Q and R were shown by (Bolton, 1986) to be about 10 and 1.0 respectively, for quartzitic sands. The parameter Q defines the mean stress level at which the CSL shifts sharply downwards due to considerable particle crushing (Boulanger, 2003a). By increasing the value of R to 1.5 a better approximation is provided for Direct Simple Shear (DSS) tests (Boulanger & Ziotopoulou, 2015). An example of the critical state line in the D$_R$-p plane with the parameters $Q = 10$ and $R = 1.5$ and the effect of changes in Q and R on the critical state line are illustrated in Figure 2.25 and Figure 2.26 correspondingly.
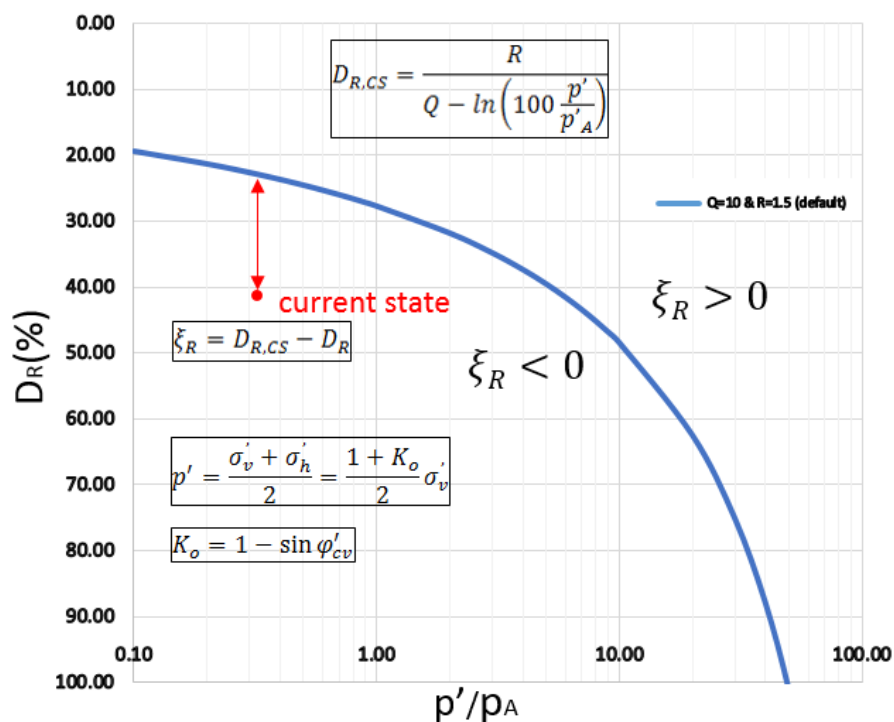
Figure 2.25: Illustration of the CSL in the $D_R - p'$ space for $Q = 10$ and $R = 1.5$.
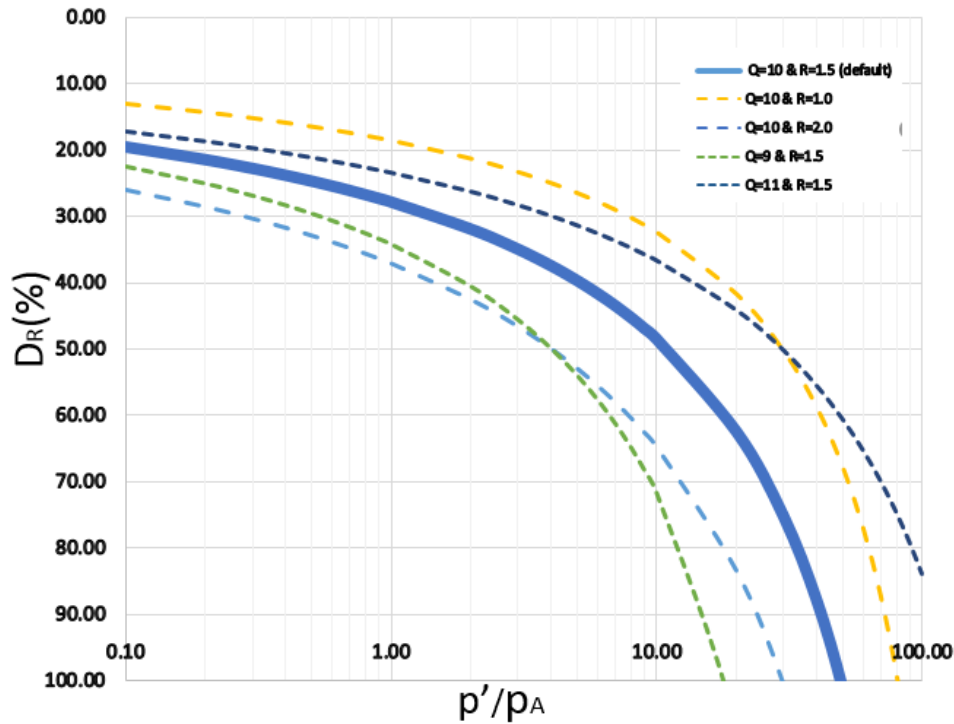
Figure 2.26: influence of Q and R on the position of the CSL.

2.7.3 Fabric Effects

The fabric-dilatancy tensor proposed by (Dafalias & Manzari, 2004) in eq.(2.14) is modified for the present model (eq.C.15-C.16). This modification was included so as the fabric tensor to evolve with plastic shear strain rather than plastic volumetric strain that occurs during dilation only. Moreover, the influence of fabric history and the cumulative fabric term are included in the present formulation.

The rate of evolution of fabric tensor in eq.(C.15) is decreasing with increasing values of the cumulative fabric term in eq.(C.16) which disables the undrained cyclic stress-strain response to lock-up into a repeating stress-strain loop and enables the progressive accumulation of shear strains (Boulanger & Ziotopoulou, 2015).

2.7.4 Model Parameters

The model parameters are grouped into two categories:

- a primary set of parameters (D_{Ro}, G_o, h_{po}) that are most important for model calibration
- a secondary set of parameters that may be modified from the recommended default values in special circumstances

Primary Model Parameters

Apparent relative density(D_{Ro}): This parameter accounts for the dilatancy and stress-strain responses of the model. The input value of D_{Ro} determines the tendency of the soil for contraction or dilation.

The apparent relative density defines initial bounding (M^b) and dilatancy (M^d) surfaces in relation to critical (M) surface through the relative state parameter (ξ_R) according to eq.(2.16) and eq.(2.17). The distance between M^b and M^d with respect to M is increasing for higher values of D_R (larger M^b and lower M^d) which corresponds to a more dilative response.

It is important to note, that the input value of D_{Ro} is referred as an "apparent relative density" rather than a strict measure and can be adjusted as part of the calibration process. The term "apparent" is used because there may be situations where the user need to modify D_R in order to improve the calibration according to relationships or test data.

Shear modulus coefficient G_o: This parameter controls the elastic shear modulus G for small strains according to:

$$G = G_{o,PM4} = G_o p_A \sqrt{\frac{p}{p_A}} \qquad (2.18)$$

Contraction rate parameter h_{po}: This parameter controls the evolution of plastic volumetric strains during contraction. During calibration its value can be adjusted to match specific Cyclic Resistance Ratio (CRR) values from in-situ tests (SPT, CPT, v_s) based on liquefaction triggering correlations (Idriss & Boulanger, 2008) or laboratory tests. For example, for in-situ tests, this parameter can be calibrated to match the CRR corresponding to $\gamma = 3\%$ in direct simple shear loading at $N_c = 15$ loading cycles over a range of relative densities (eq.(C.45-C.46)) for an earthquake of 7.5 magnitude.

Secondary Model Parameters

The secondary set of parameters can be found in Appendix C.8.

Chapter 3: Validation of the PM4Sand Model for Cyclic Loading

3.1 Introduction

The PM4Sand is a constitutive model which is able to simulate successfully the undrained behaviour of sands during earthquake loading, including the generation of pore pressures and liquefaction phenomena. What makes this model very attractive for practical applications is that there are mainly three primary model parameters to be determined in the calibration process: the apparent relative density D_{Ro}, the shear modulus coefficient G_o and the contraction rate parameter h_{po} while the secondary parameters are suggested to be used with default values. However, the user can modify the secondary parameters in the calibration process for particular loading conditions.

The response of the model varies for different cyclic stress levels and in-situ conditions thus, it has to be examined and compared to what has been observed in real practice. Therefore, the PM4Sand model, which is implemented in Plaxis 2D software, is investigated at element level to evaluate whether it can reproduce similar responses with respect to what has been observed in laboratory tests.

For the evaluation process, Cyclic Direct Simple Shear ($CDSS$) tests performed on Ottawa F-65 Sand are analysed. Then, the PM4Sand model is calibrated according to the cyclic strength curves obtained from these tests and the responses for different loading conditions and confinement levels are assessed. Moreover, the influence of the parameters in the response of the model is examined by performing a parametric assessment analysis.

3.2 Data Interpretation

The validation of the PM4Sand model is investigated by analysing undrained Cyclic Direct Simple Shear ($CDSS$) tests performed on Ottawa F-65 Sand (https://datacenterhub.org/resources/ottawa_f_65). The evaluation of the model's performance on the aforementioned type of sand has already been investigated by (Bastidas, 2016) using single-element numerical simulations in FLAC 2D. In this study, the validation is accomplished using element tests in Plaxis software.

The Ottawa F-65 sand is classified as a white grained silica sand with rounded grains and a quartz content of 99.7%. Its index properties are given in Table 3.1. The samples are prepared by the dry funnel deposition method and the tests were performed in a GEOTAC Direct Simple Shear apparatus (Bastidas, 2016).

Index properties	
Specific gravity (G_s)	2,65
Medium grain size (D_{50}, mm)	0,20
Maximum void ratio (e_{max})	0,83
Minimum void ratio (e_{min})	0,51
Critical state friction angle (ϕ'_{cv})	33,00

Table 3.1: Index properties of Ottawa F-65 Sand

The tests were performed for loose samples normally consolidated under vertical effective stresses of $50kPa$, $100kPa$ and 400kPa. The samples are loaded under various cyclic stress levels and prepared under different relative densities (Table 3.2). For the sake of convenience, the average values of relative densities over the three ranges is adopted (40%, 40% and 45%). Then, the cyclic strength curves for each confining level can be constructed from the different combinations of Cyclic Stress Ratio (CSR) and number of cycles (N) to reach a 3% peak shear strain in direct simple shear loading (Figure 3.2). The exponential relationships ($CSR = aN^{-b}$) between the CSR and N are also depicted.

D_R (%)	Average D_R (%)	σ'_{vc} (kPa)	CSR
37-46	40	50	0.080-0.107
34-47	40	100	0.086-0.114
37-48	45	400	0.087-0.115

Table 3.2: Relative density, confining stress, Cyclic Stress Ratio for the CDSS tests.
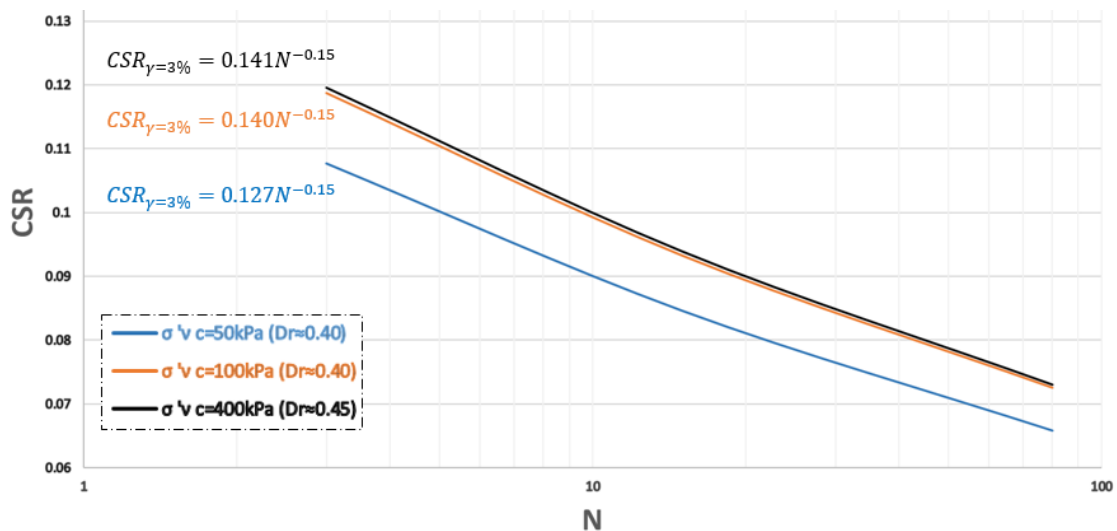
Figure 3.1: Cyclic strength curves obtained from CDSS tests performed on Ottawa Sand (Bastidas, 2016) for confining stresses of 50kPa, 100kPa and 400kPa.

At this point an important observation is that normally one would expect a reduction in the CRR by increasing the confining stress level under the same (or similar) relative density level (Chapter 2.3.4). However, according to the test results for Ottawa F-65 Sand, the reverse effect is observed. The cyclic resistance curves obtained from the laboratory are increasing with an increasing consolidation stress. In particular, the CRR is increasing by 11% from $\sigma'_{vc} = 50kPa$ to $\sigma'_{vc} = 100kPa$ and at $\sigma'_{vc} = 400kPa$ the CRR is the same as at $\sigma'_{vc} = 100kPa$ (Figure 3.1).

3.3 Input Model Parameters

The primary model parameters D_{Ro}, G_o and h_{po} can be calibrated according to laboratory or in-situ test data while the secondary model parameters can be used with its default values. The relative density D_{Ro} accounts for the dilatancy and the stress-strain responses of the model as it defines the tendency of the soil for contraction or dilation through the relative state parameter (Chapter 2.8.4). The shear modulus coefficient G_o controls the elastic shear modulus G at small strains (eq.(2.18)) while the contraction rate parameter h_{po} governs the evolution of plastic volumetric strains and can be calibrated to match specific Cyclic Resistance Ratio (CRR) values.

In this thesis project, the apparent relative density D_{Ro} is determined from laboratory data while the shear modulus coefficient G_o is estimated from correlation since there is no information about the dynamic soil properties of Ottawa F-65 Sand (e.g the shear wave velocity profile). The contraction rate parameter h_{po} can be calibrated according to two criteria. The first one indicates that the onset of liquefaction is captured after reaching a specific percentage of shear strain ($e.g$ $\gamma = 3\%$) in direct simple shear loading for a certain number of loading cycles (N_c). The second one indicates that liquefaction is triggered when the pore pressure ratio ($r_u = \Delta u / \sigma'_{vc}$) is reaching a value of about 1.0 for a specified number of loading cycles (N_c).

In this study, the h_{po} parameter is calibrated with respect to both criteria. Initially, according to $\gamma = 3\%$ as implemented by (Bastidas, 2016) in order to evaluate any differences between the responses from FLAC and Plaxis and with the aim to get a first insight about the overall response of the model. Secondly, it is calibrated according to $r_u = 1.0$ as this criterion is regarded as the most representative for the prediction of earthquake induced liquefaction in hydraulic fills (Chapter 5.6).

Apparent Relative Density $\mathbf{D_R}$

This parameter is determined as the value of relative density measured in the laboratory. Thus, for the specimens confined under vertical effective stresses of $\sigma'_{vc} = 50kPa$, $\sigma'_{vc} = 100kPa$ and $\sigma'_{vc} = 400kPa$ the relative density is defined as $D_R = 0.40$, $D_R = 0.40$ and $D_R = 0.45$ respectively. The 'apparent' value of D_R means that the aforementioned quantities are an initial estimation for the calibration and the user can adjust them later on in order to better approximate the responses of interest.

Shear Modulus Coefficient $\mathbf{G_o}$

Due to the lack of available dynamic soil test data (e.g the shear wave velocity profile) from which to calibrate G_o, this parameter can be related over a range of relative densities according to the following equation which is a combination between eq.(C.45) and eq.(C.49) as:

$$G_o = 167\sqrt{46D_R^2 + 2.5} \qquad (3.1)$$

Contraction rate parameter h_{po}

This parameter can be calibrated either according to reaching a specific percentage of shear strain ($e.g\ \gamma = 3\%$) in direct simple shear loading for specified number of loading cycles (N_c) or in order to reach a pore pressure ratio ($r_u = \Delta u / \sigma'_{vc}$) of about 1.0. The $r_u = 1.0$ condition represents the onset of liquefaction in which shear strains exceed the elastic shear strain threshold.

The h_{po} parameter is initially calibrated according to the $\gamma = 3\%$ criterion at $N_c = 15$ loading cycles for the CRR curve at an overburden stress of 100kPa. In this way, having an initial estimate about the set of model parameters, the performance of the PM4Sand model is evaluated for all confining stress levels ($\sigma'_{vc} = 50kPa$, $\sigma'_{vc} = 100kPa\ and\ \sigma'_{vc} = 400kPa$) (Figure 3.2). In addition, the h_{po} parameter is recalibrated with respect to the pore pressure ratio ($r_u \approx 1$) which is the most relevant criterion for the prediction of earthquake induced liquefaction in hydraulic fills in real practice.

Plaxis Soil Element Tests

The performance of the PM4Sandmodel for the liquefaction triggering is verified by reproducing undrained Cyclic Direct Simple Shear ($CDSS$) tests in the Plaxis SoilTest facility at element level. The coefficient of earth pressure at rest is defined as: $K_o = 1 - \sin(\varphi'_{cv}) = 1 - \sin 33^o = 0.46$.

The apparent relative density D_R for the confining stress levels of $\sigma'_{vc} = 50kPa$, $\sigma'_{vc} = 100kPa$ and $\sigma'_{vc} = 400kPa$ is taken as $D_R = 0.40$, $D_R = 0.40$ and $D_R = 0.45$ respectively (Table 3.2). The shear modulus coefficient G_o is calculated according to eq.(3.1) as $G_o = 524$, $G_o = 524$ and $G_o = 624$ correspondingly. The contraction rate parameter h_{po} is adjusted ($h_{po} = 0.37$) to match the CRR corresponding to $\gamma = 3\%$ ($CRR = 0.093$) at $N_c = 15$ loading cycles from Plaxis element tests at the confining stress of $\sigma'_{vc} = 100kPa$ (Figure 3.2). In the study from (Bastidas, 2016) the only difference is that the contraction rate parameter h_{po} had a slightly lower value of 0.33. Then the ability of the model to reproduce the other cyclic strength curves at different levels of CSR and at different overburden stresses ($\sigma'_{vc} = 50kPa, \sigma'_{vc} = 400kPa$) is evaluated.
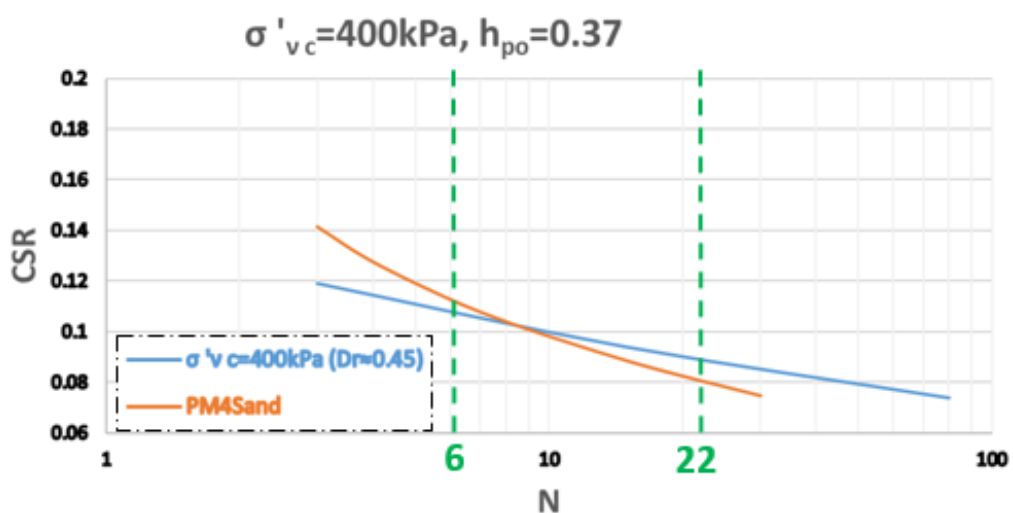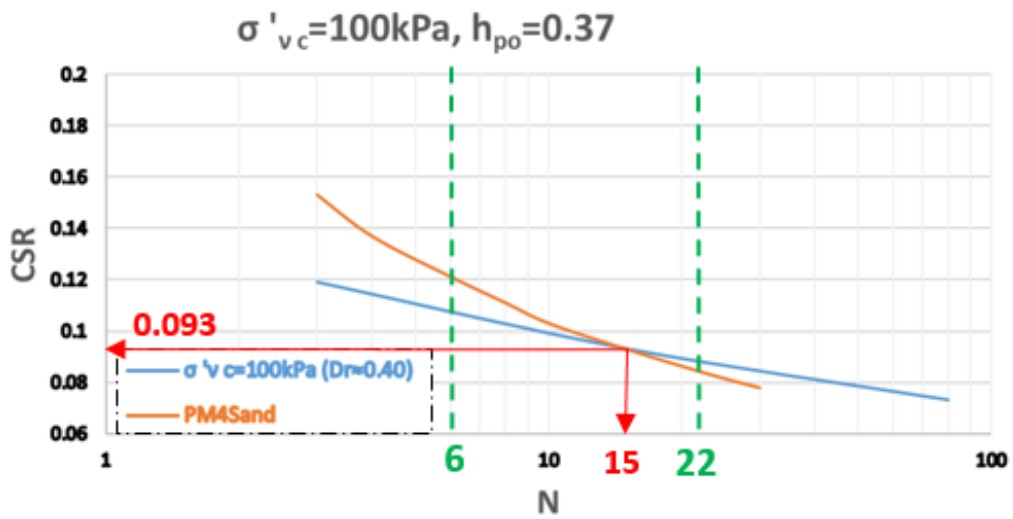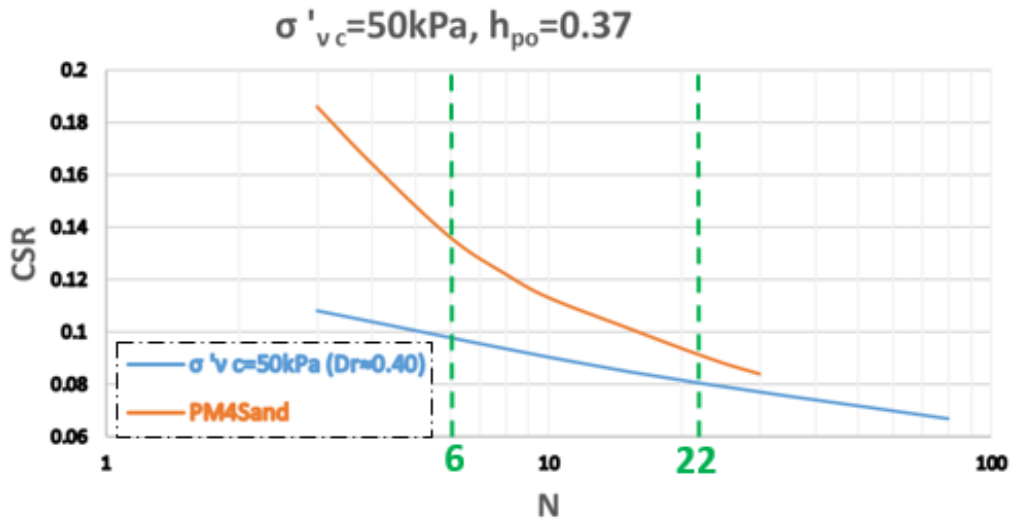
Figure 3.2: Comparison of cyclic strength curves obtained from CDSS tests performed on Ottawa Sand to the simulated response from Plaxis PM4Sand model

It is observed, that the cyclic strength curves produced by the PM4Sand are steeper than the experimental responses, especially for the lower confinement of $50kPa$ (Figure 3.2). Consequently, even though the model was calibrated to match a specific liquefaction criterion ($\gamma = 3\% \ at \ N_c = 15$), it is not able to reproduce the same conditions at different CSR levels. In general, the model overestimates the cyclic resistance for small number of loading cycles and underestimates the cyclic resistance for large number of loading cycles. This effect is decreased with an increasing overburden stress. The aforementioned conclusion does not mean that the model is not capable of reproducing the general features of cyclic loading as in real practice, there is a certain $CRR - N$ range that is of interest rather than the whole part of the CRR curve. Related to the study from (Bastidas, 2016) the cyclic strength curves obtained by Plaxis approximated well the corresponding responses from FLAC.

In earthquake design it is important to define which part of the $CRR - N$ curve (Figure 3.2) is of high significance. In general, the majority of seismic events are having a magnitude (M_w) between 6 and 8. Thus, in terms of uniform loading cycles, this range is corresponding to a range between 6 and 22 cycles (Figure A.21) (Appendix A.2). Thus, from now on, this range will be examined as one can assume that higher or lower values are not relevant for common design purposes (Figure 3.2).

The evolution of excess pore water pressures (Figure 3.4) along with the stress-strain responses (Figure 3.3) produced by PM4Sand are compared to the experimental results for $D_R = 0.40$ and $\sigma'_{vc} = 100kPa$ performed at a $CSR = 0.086$.

The PM4Sand simulations accumulate a lower r_u than the experimental responses during the first two loading cycles ($N_c = 2$) (Figure 3.4). After $N_c = 2$, the rate of r_u accumulation is similar to the experimental responses until $N_c = 14$. After $N_c = 14$, the simulations accumulate r_u more rapidly and between $N_c = 17$ and $N_c = 18$, the shear strains exceed the elastic shear strain threshold with the r_u being increased from 0.6 to about 1.0. However, the increase of r_u is occurring more gradually in the experiments reaching a value of about 1.0 at $N_c = 25$.
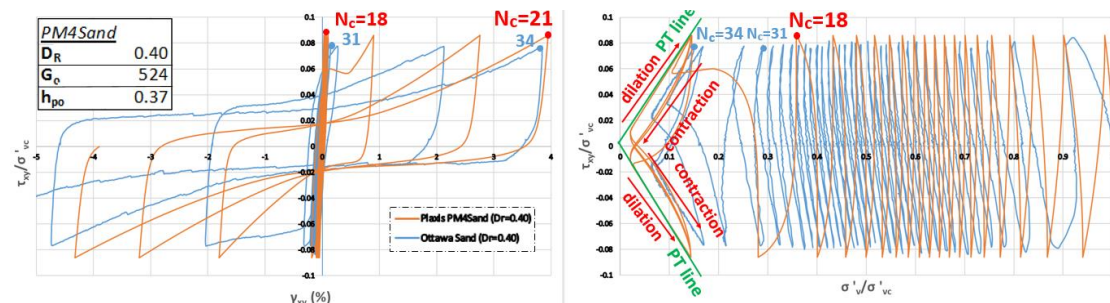
Figure 3.3 a, b: Simulated and experimental stress-strain responses and stress path
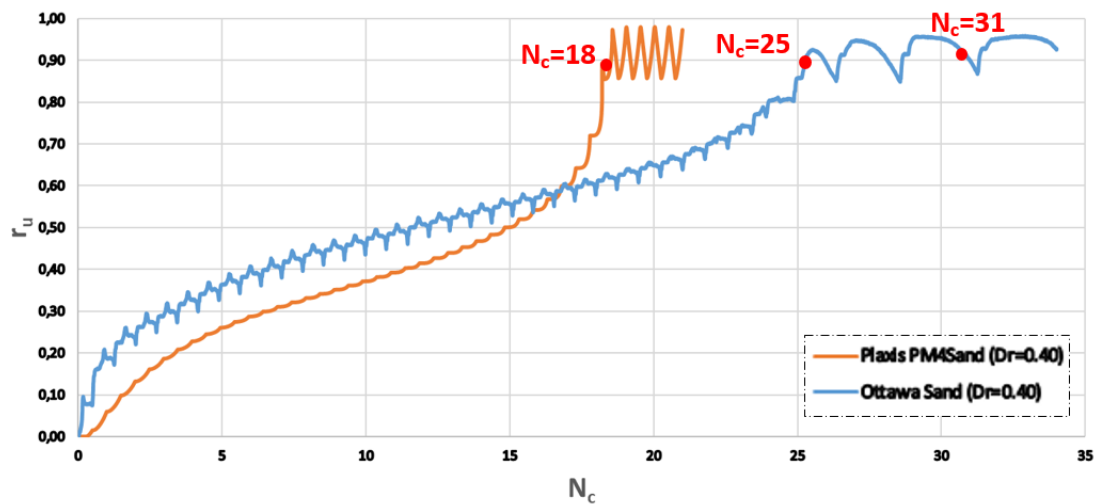
Figure 3.4: Simulated and experimental excess pore pressure generation.

Related to the excess pore pressure generation (r_u), the decrease of effective stresses in the simulated stress path during the first two loading cycles is more restraint than in the experiment (Figure 3.3 b) which is translated to a lower contraction per loading cycle. Between $N_c = 2$ and $N_c = 14$ soil densification is observed in both simulated and experimental responses. At the point of elastic shear strain threshold exceedance ($N_c = 18$), rapid soil degradation is observed in the simulations which leads to significant stiffness and strength reduction, as the accumulations of shear strains increase considerably due to cyclic mobility (Figure 3.6 a). This temporary condition occurs under an isotropic stress state. During this condition, the samples are having dilative tendencies when loaded leading to an increase in vertical effective stresses and contractive tendencies when unloaded leading to an decrease in vertical effective stresses (Figure 3.3-b). On the contrary, at the point where the experimental responses are reaching an excess pore pressure ratio (r_u) of about 1.0 ($N_c = 25$) the aforementioned soil degradation effect is absent. It takes about 6 more cycles (Figure 3.3a - $N_c = 31$) for the specimens to present significant stiffness reduction.

Regarding the aforementioned results, the PM4Sand model well approximated the general features of cyclic loading in terms of stress-strain responses, stress path and excess pore pressure generation while better approximated soil behaviour can be obtained after gaining deeper insight into the model performance. For that purpose, the possibility of reducing the steepness of the $CRR - N$ curves is examined in the following section by using different set of parameters. Moreover, a parametric assessment is performed in order to evaluate the influence of the model parameters to the soil response and the possibility of better approximating the $r_u - N$ response (Figure 3.4) is examined by recalibrating the contraction rate parameter h_{po} for different values of primary and secondary model parameters.

3.4 Influence of the Primary Model Parameters

3.4.1 Influence of D_R

The influence of the apparent relative density D_R with respect to the $CRR - N$ response and to the evolution of excess pore pressures (r_u) is evaluated by testing seven new set of parameters (Table 3.2). The first pair includes the variation of D_R by keeping all the other parameters constant. In the following two sets, the recalibration of the contraction parameter h_{po} is performed according to the first liquefaction criterion ($\gamma = 3\%$ at $N_c = 15$ $cycles$) while the last three are about the recalibration of the parameter h_{po} parameter according to the second liquefaction criterion ($r_u = 1.0$ at $N_c = 25$ $cycles$) at a CSR of 0.086.

| | i | γ=3% at $N_c = 15$ | | | | $r_u = 1.0$ | | |
		ii	iii	iv	v	vi	vii	viii
D_R	0.40	0.35	0.45	0.35	0.45	0.40	0.35	0.45
G_o	524	524	524	524	524	524	524	524
h_{po}	0.37	0.37	0.37	0.65	0.21	0.515	0.90	0.295

Table 3.2: Parametric assessment of $\boldsymbol{D_R}$ in the model response by using different set of parameters.
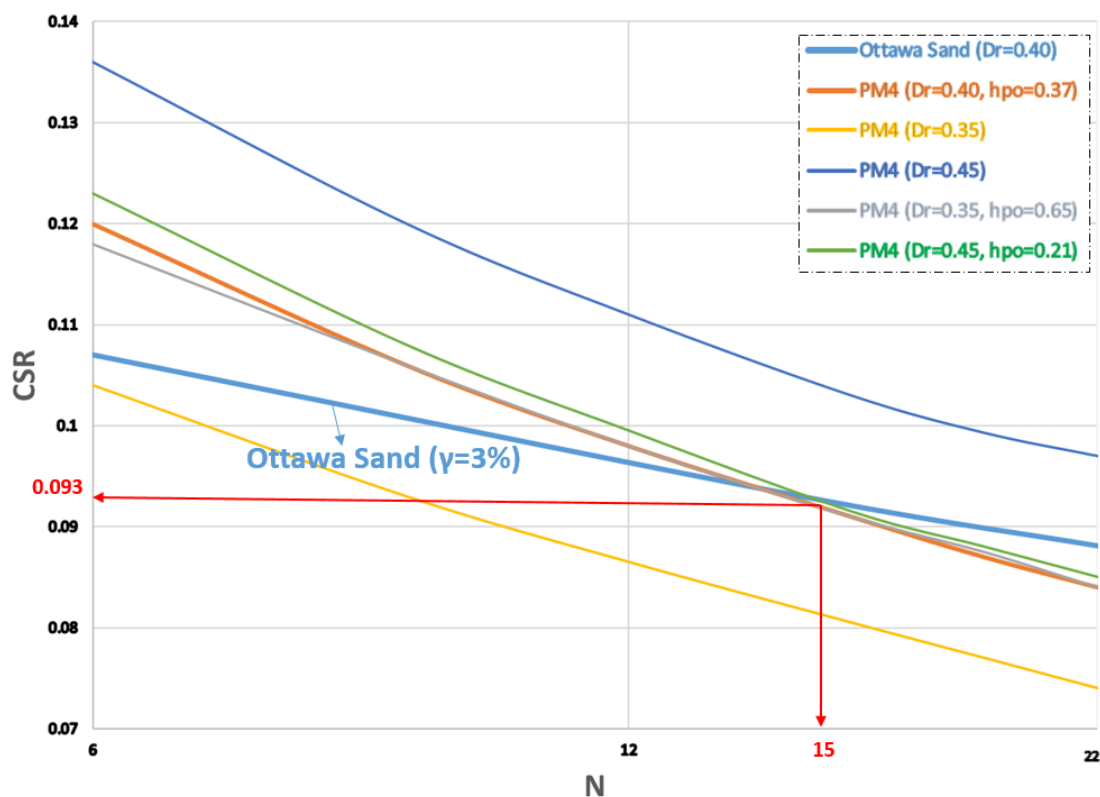
Figure 3.5: Influence of the apparent relative density $\boldsymbol{D_R}$ on the $CRR - N$ curves.

It is observed, that the apparent relative density D_R has a direct influence in the $CRR - N$ response (Figure 3.5). Without recalibration of h_{po}, by using lower values of D_R (0.35) the cyclic strength curve is moving downwards in a parallel manner compared to the curve at $D_R = 0.40$ by decreasing the liquefaction resistance by 13% between 6 and 22 uniform loading cycles. On the other hand, using higher values of D_R (0.45) the cyclic strength curve is moving upwards in a parallel manner compared to the curve at $D_R = 0.40$ by increasing the liquefaction resistance by 13% in the range between 6 and 22 uniform loading cycles. Moreover, by recalibrating the contraction parameter h_{po} and using a lower value of D_R, the steepness of the $CRR - N$ curve is slightly reduced by 2% at $N = 6$ whereas a higher value of D_R leads to an even steeper curve (3% increase at $N = 6$). The aforementioned observation is really important as the apparent relative density D_R, as an input parameter, has a crucial effect in the liquefaction resistance for the design of hydraulic fills under earthquake loading over the whole range of interest ($N = 6 - 22$ uniform loading cycles).

The influence of the apparent relative density on the model response can be explained by eq.(C.2-C.4) (Appendix C). It is clear that, the D_R defines initial bounding and dilatancy surfaces through the relative state parameter ξ_R. Therefore, for a given cyclic loading level, the looser the soil is the more rapidly the bounding surface is approaching the critical surface where plastic deformations are evolving under constant mean effective stresses.
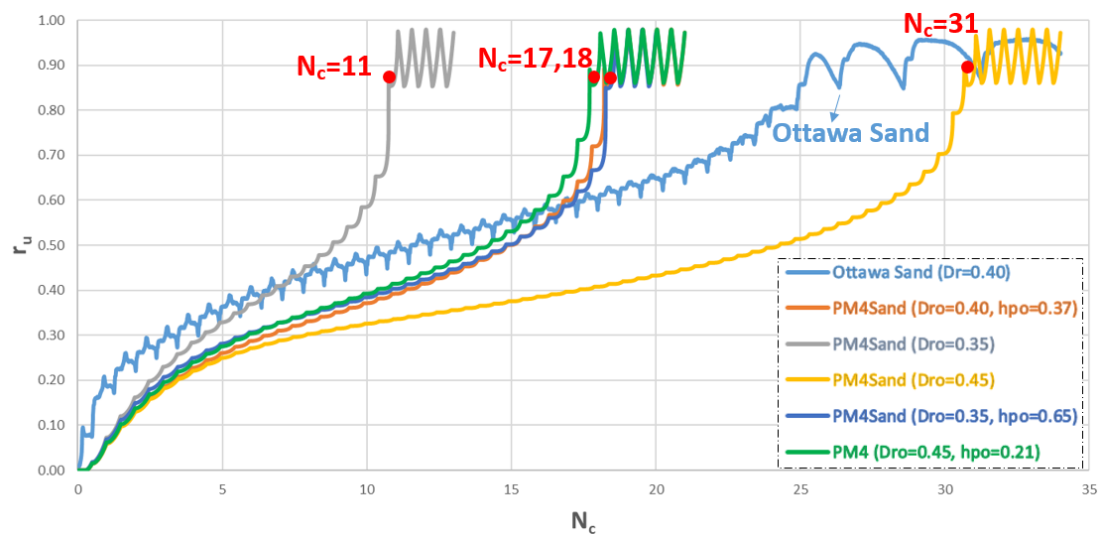
Figure 3.6: Influence of the apparent relative density $\boldsymbol{D_R}$ on the generation of excess pore pressures.

Related to the excess pore pressure generation (r_u), the simulations accumulate similar r_u during the first five loading cycles ($N_c = 5$) for all values of D_R (Figure 3.6). After this stage, the impact of D_R in the soil behaviour until a r_u of around 1.0 is reached is clear. Without recalibration of h_{po}, the simulations show stiffer response for an increasing value of D_R (0.45) as more cycles are required to reach that state ($N_c = 31$) (critical state is reached slower). Conversely, the simulations show softer response for a decreasing value of D_R (0.35), as less number of cycles are required ($N_c = 11$) (critical state is reached faster). It should be noted, that the effect of the recalibration of h_{po} parameter to the generation of excess pore pressures is almost negligible as the response remains the same.

The influence of the apparent relative density D_R on the evolution of excess pore pressures can be explained as follows: using lower values of D_R will define lower bounding surface (M^b). This will result in lower elastic shear modulus G (eq.(C.20)) through the stress-ratio effects (eq.(C.21)). Consequently, the bulk modulus K is going to be lower which eventually restricts the elastic volumetric strain increment (eq.(C.18)) and thus the evolution of excess pore pressures. As a result, the looser the sand is the faster the generation of excess pore pressures is accomplished

Moreover, the contraction rate parameter h_{po} is recalibrated according to the second liquefaction criterion ($r_u = 1.0 \ at \ N_c = 25 \ cycles$) for three different values of D_R at a CSR of 0.086 (Figure 3.7). This was done in order to investigate the possibilities of approaching more accurately the $r_u - N$ curves obtained from the laboratory.
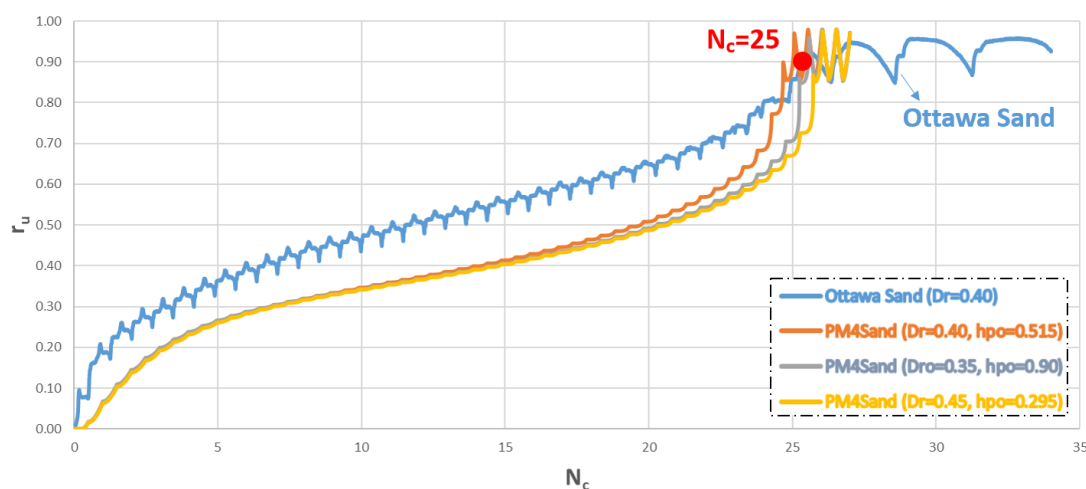
Figure 3.7: Influence of the recalibration of the contraction rate parameter h_{po} regarding the $r_u \approx 1$ criterion at $N_c = 25$ cycles at a CSR of 0.086.

It is observed that the recalibration of the h_{po} parameter led to a precise approximation concerning the $r_u \approx 1$ state at a CSR of 0.086 (Figure 3.7) by varying apparent relative density D_R. One important observation is, that the generation of excess pore pressures until $r_u \approx 1$ from PM4Sand model is almost the same for all three different set of parameters.

3.4.2 Influence of G₀

The influence of the shear modulus coefficient G_o with respect to the $CRR - N$ response and to the evolution of excess pore pressures (r_u) is evaluated by testing four new set of parameters (Table 3.3). The first pair includes the variation of G_o by keeping all the other parameters constant. In the following two sets, the recalibration of the contraction parameter h_{po} is performed according to the first liquefaction criterion ($\gamma = 3\% \ at \ N_c = 15 \ cycles$).

	i	ii	iii	iv	v
D_R	0.40	0.40	0.40	0.40	0.40
G_o	524	100	1000	100	1000
h_{po}	0.37	0.37	0.37	0.425	0.32

Table 3.3: Parametric assessment of G_o in the model response by using different set of parameters.
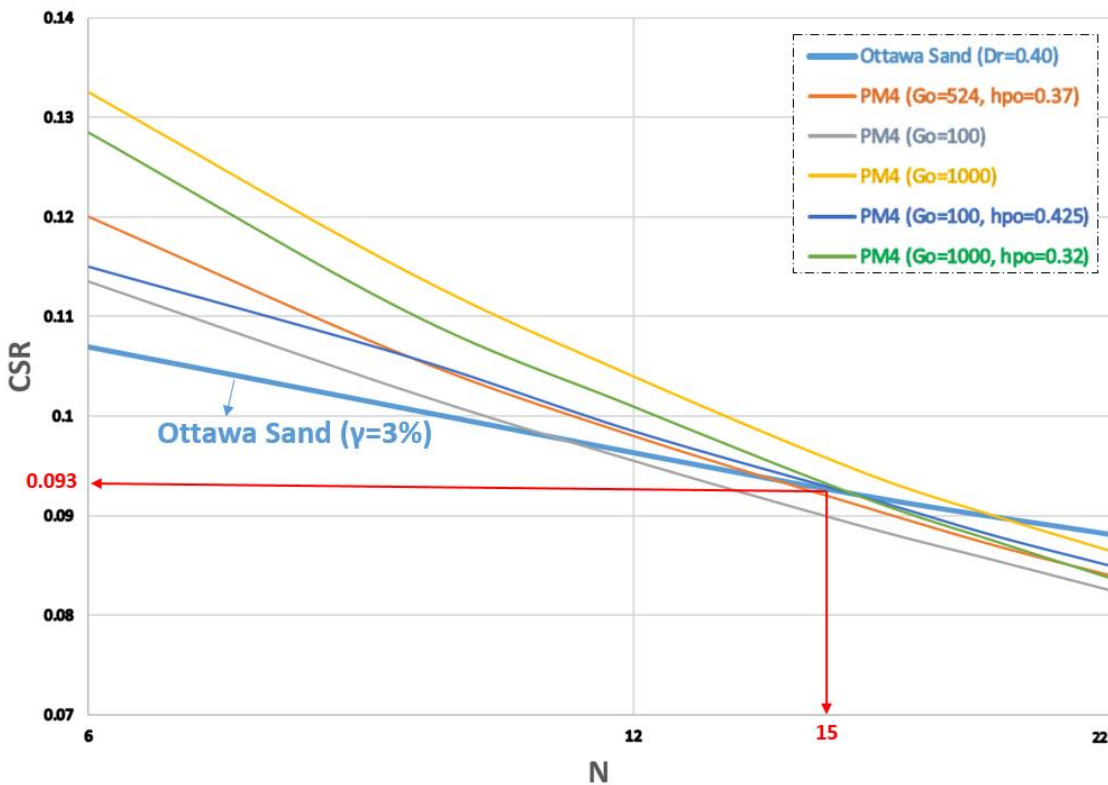
Figure 3.8: Influence of the shear modulus coefficient G_o on the $CRR - N$ curves.

It is observed, that the influence of the shear modulus coefficient G_o in the $CRR - N$ response (Figure 3.8) is of less significance, compared to the corresponding effect of apparent relative density D_R (Figure 3.8). Without recalibration of h_{po}, by using lower values of G_o (100) the cyclic strength curve is moving downwards with respect to the curve at $G_o = 524$ by decreasing the liquefaction resistance by 6% at $N = 6$ and by 2% at $N = 22$ uniform loading cycles. Consequently, the effect of G_o in cyclic strength for large number of loading cycles is becoming trivial. On the other hand, using higher values of G_o (1000) the cyclic strength curve is moving upwards compared to the curve at $G_o = 524$ by increasing the liquefaction resistance by 11% at $N = 6$ and by 7% at $N = 22$ uniform loading cycles. Moreover, by recalibrating the contraction parameter h_{po} and using a lower value of G_o , the steepness of

the CRR-N curve is slightly reduced by 4% at $N = 6$ whereas a higher value of G_o leads to an even steeper curve (7% increase at $N = 6$).
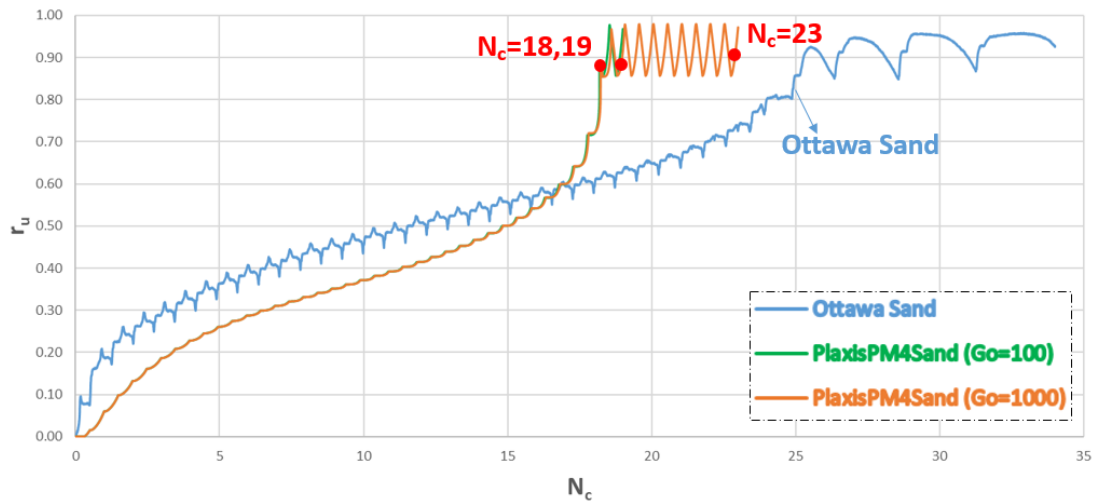
Figure 3.9: Influence of the shear modulus coefficient G_o on the generation of excess pore pressures.
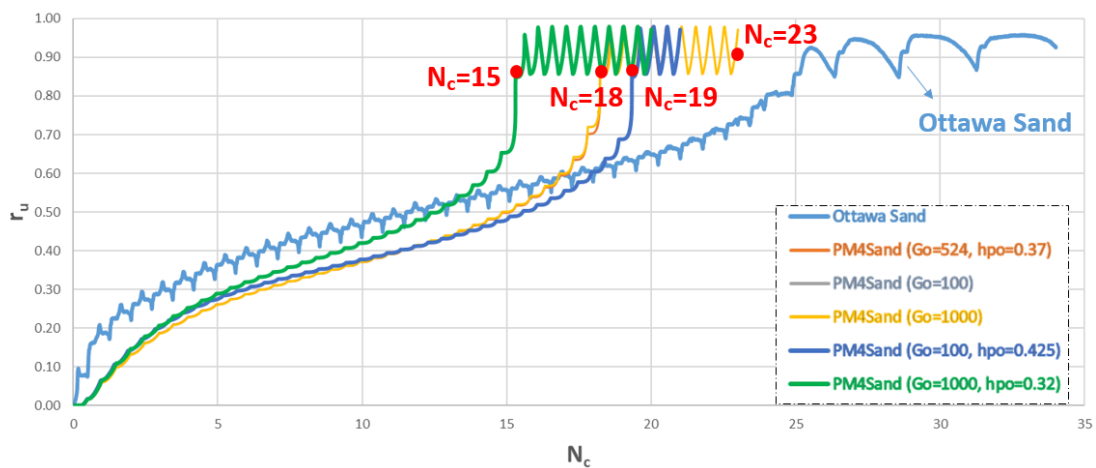
Figure 3.10: Influence of the shear modulus coefficient G_o on the generation of excess pore pressures.

Related to the excess pore pressure generation (r_u), it is shown, that without recalibration of the contraction rate parameter h_{po}, the variation of G_o is not affecting the generation of excess pore pressures at all until an r_u of around 1.0 is reached (Figure 3.9). For that reason, the recalibration of h_{po} according to the second liquefaction criterion ($r_u = 1.0$) is not investigated for the shear modulus coefficient G_o. However, the fact that there is no influence of G_o throughout the whole response before $r_u = 1.0$ seems odd in the following sense: as explained in section 3.5.1 the evolution of excess pore pressures is governed by the restriction of the elastic volumetric strain tensor to evolve which depends on the bulk modulus K (through the elastic shear modulus G). Due to the fact that the shear modulus coefficient G_o is directly proportional to the elastic shear modulus G one would expect considerable effects on the evolution of r_u with the variation in G_o.

On the other hand, the effect of the variation of shear modulus coefficient G_o is significant in the rate of shear strain accumulation after $r_u = 1.0$ ($N_c = 18$) (Figure 3.9). It is clear, that a higher value of G_o leads to significant increase in the accumulation of shear strains per loading cycle after an r_u of around 1.0 is reached compared to a lower G_o in which the shear strain accumulation is more gradual. After an $r_u = 1.0$ ($N_c = 18$) a shear strain of approximately 3% is reached after 1 cycle for $G_o = 100$ ($N_c = 19$) and after 5 cycles for $G_o = 1000$ ($N_c = 23$). This effect can be explained as follows: the factor that regulates whether the accumulation of shear strains after an r_u of around 1.0 is reached is accomplished in a gradual or progressive manner is the fabric tensor (eq.C.15)). This tensor is dependent on the plastic shear strain increment (de^{pl}) (eq.(C.24) through the ratio between plastic volumetric strain increment ($d\varepsilon_v^{pl}$) and dilatancy (D) (eq.(C.15)). From eq.(C.24 to C.26) the(de^{pl}) is directly proportional to the loading index L which is inversely proportional to the plastic modulus K_p (eq.(C.28)). The latter is directly proportional to G_o through the elastic shear modulus G (eq.(C.31)). As a results higher values of G_o lead to a more progressive shear strain accumulation after an r_u of around 1.0 is reached.

Moreover, it is shown, that the recalibration of h_{po} by using higher values of G_o (1000) led to slower generation of excess pore pressures ($N_c = 15$) while the effect of recalibration of h_{po} by using lower values of G_o (100) on the evolution of r_u is almost negligible ($N_c = 19$) (Figure 3.10).

3.5 Influence of the Secondary Model Parameters

3.5.1 Influence of n^b

The bounding surface parameter n^b is used to define the initial bounding surface (eq.(C.3)) and consequently affects the distance between the bounding and critical state surface. Therefore, it defines the rate with which the bounding surface is approaching the critical surface. Moreover, the n^b affects the dilatancy D (eq.C.34 to eq.C.44) which governs the evolution of plastic volumetric strains (eq.C.23)).

The influence of the bounding surface parameter n^b with respect to the $CRR - N$ response and to the evolution of excess pore pressures (r_u) is evaluated by testing six new set of parameters (Table 3.4). The first pair includes the variation of n^b by keeping all the other parameters constant. In the following set, the recalibration of the contraction parameter h_{po} is performed according to the first liquefaction criterion ($\gamma = 3\%$ at $N_c = 15$ $cycles$) while the last three are about the recalibration of the parameter h_{po} parameter according to the second liquefaction criterion ($r_u = 1.0$ at $N_c = 25$ $cycles$) at a CSR of 0.086

	i	ii	iii	iv	v	vi	vii
D_R	0.40	0.40	0.40	0.40	0.40	0.40	0.40
G_o	524	524	524	524	524	524	524
h_{po}	0.37	0.37	0.37	0.26	0.515	0.455	0.33
n^b	0.50	0.25	0.10	0.10	0.50	0.25	0.10

Table 3.4: Parametric assessment of n^b in the model response by using different set of parameters.
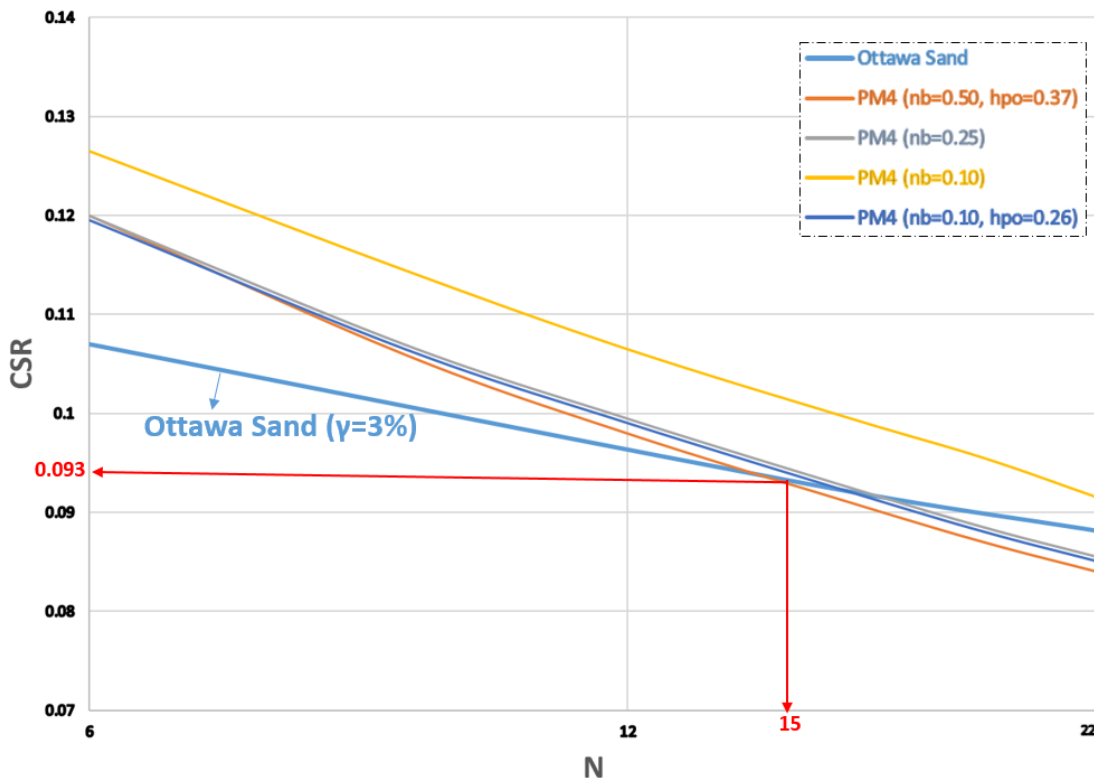
Figure 3.11: Influence of the bounding surface parameter n^b on the $CRR - N$ curves.

It is observed, that bounding surface parameter n^b do not affect the $CRR - N$ response besides when using $n^b = 0.10$ without the recalibration of h_{po} (Figure 3.11). In that case, the cyclic strength curve is moving upwards in a parallel manner compared to the curve at $n^b = 0.50$ by increasing the liquefaction resistance by around 7.5% between 6 and 22 uniform loading cycles. However, in all other cases, the effect of n^b in cyclic strength throughout the whole range of interest is becoming trivial.

Figure 3.12: Influence of the bounding surface parameter n^b on the generation of excess pore pressures.

Related to the excess pore pressure generation (r_u), the simulations accumulate similar r_u during the first twelve loading cycles ($N_c = 12$) besides when using $n^b = 0.10$ without the recalibration of h_{po} (Figure 3.12). After this stage, the simulations show stiffer response for a decreasing value of n^b especially for the lowest (0.10) as more cycles are required to reach an r_u of around 1.0 ($N_c = 29$) (critical state is reached slower). It should be noted, that the recalibration of h_{po} parameter do not have a big impact to the generation of excess pore pressures as a slight increase in loading cycles is observed (($N_c = 20$).

Moreover, the contraction rate parameter h_{po} is recalibrated according to the second liquefaction criterion ($r_u = 1.0$ at $N_c = 25$ cycles) for two different values of n^b at a CSR of 0.086 (Figure 3.13). This was done in order to investigate the possibilities of approaching more accurately the $r_u - N$ curves obtained from the laboratory.
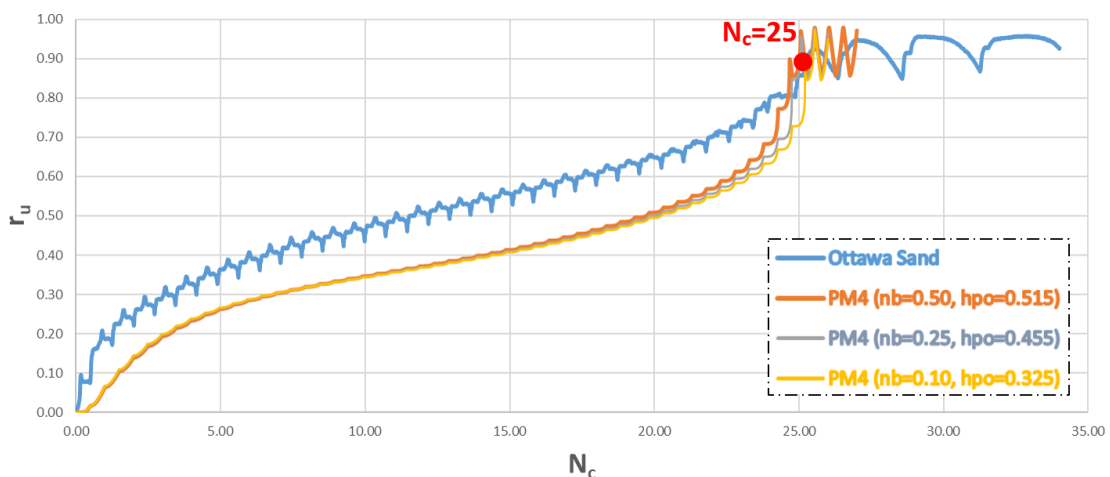
Figure 3.13: Influence of the recalibration of the contraction rate parameter h_{po} regarding the $r_u \approx 1$ criterion at $N_c = 25$ cycles at a CSR of 0.086.

It is observed, that the recalibration of the h_{po} parameter led to a precise approximation concerning the $r_u \approx 1$ state at a CSR of 0.086 (Figure 3.10) by varying the bounding surface parameter n^b. One important observation is, that the generation of excess pore pressures until $r_u \approx 1$ from PM4Sand model is almost the same for all three different set of parameters.

3.5.2 Influence of R

In PM4Sand model, the critical state line (CSL) is defined with respect to two parameters: the critical state parameter R and Q as proposed by (Bolton, 1986). These parameters are affecting the curvature and position of the CSL (Figure C.1). In this study the influence of the R parameter is going to be examined as after parametric assessment the cyclic response of the model is not considerably affected by the parameter Q.

The influence of the critical state parameter R with respect to the $CRR - N$ response and to the evolution of excess pore pressures (r_u) is evaluated by testing four new set of parameters (Table 3.5). The first pair includes the variation of R by keeping all the other parameters constant. In the following two sets, the recalibration of the contraction parameter h_{po} is performed according to the first liquefaction criterion ($\gamma = 3\% \; at \; N_c = 15 \; cycles$) while the last three are about the recalibration of the parameter h_{po} parameter according to the second liquefaction criterion ($r_u = 1.0 \; at \; N_c = 25 \; cycles$) at a CSR of 0.086.

	i	ii	iii	iv	v	vi	vii	viii
		$\gamma=3\%$ at $N_c = 15$				$r_u = 1.0$		
D_R	0.40	0.40	0.40	0.40	0.40	0.40	0.40	0.40
G_o	524	524	524	524	524	524	524	524
h_{po}	0.37	0.37	0.37	0.155	0.81	0.515	0.235	1.11
n^b	0.50	0.50	0.50	0.50	0.50	0.50	0.50	0.50
R	1.50	1.00	2.00	1.00	2.00	1.50	1.00	2.00

Table 3.5: Parametric assessment of R in the model response by using different set of parameters
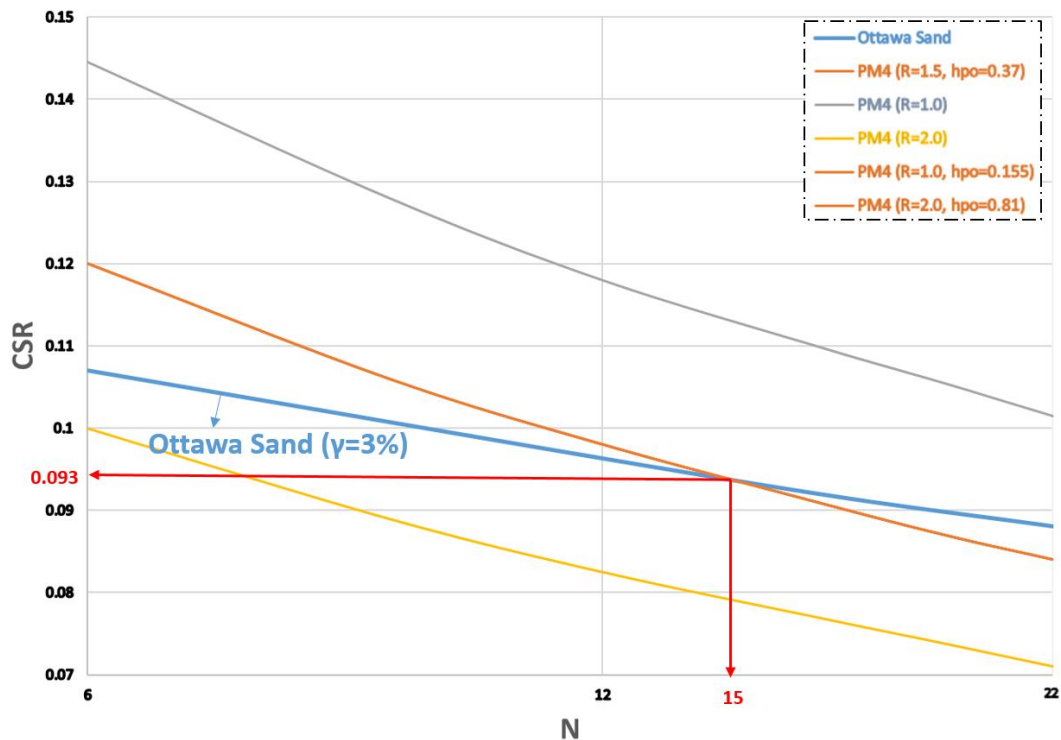
Figure 3.14: Influence of the bounding surface parameter R on the $CRR - N$ curves.

It is observed that the critical state parameter R has a direct influence in the $CRR - N$ response (Figure 3.14). Without recalibration of h_{po}, by using lower values of R (1.0) the cyclic strength curve is moving upwards in a parallel manner compared to the curve at $R = 1.5$ by increasing the liquefaction by 20% between 6 and 22 uniform loading cycles. On the other hand, using higher values of R (2.0) the cyclic strength curve is moving downwards in a parallel manner compared to the curve at $R = 1.5$ by decreasing the liquefaction resistance by 16% in the range between 6 and 22 uniform loading cycles. Moreover, by recalibrating the contraction parameter h_{po} for different values of R the steepness of the $CRR - N$ curves are not modified at all.

The influence of the critical state parameter R on the model response can be explained by eq.(C.2-C.4) and Figure C.1 (Appendix C). By increasing the parameter R the critical state line is moving downwards. This will lead to a decrease in $D_{R,CS}$ which gives a lower relative state parameter ξ_R enabling the model to approach the CSL faster. This effect is comparable to the apparent relative density as both parameters are related to the relative state parameter.
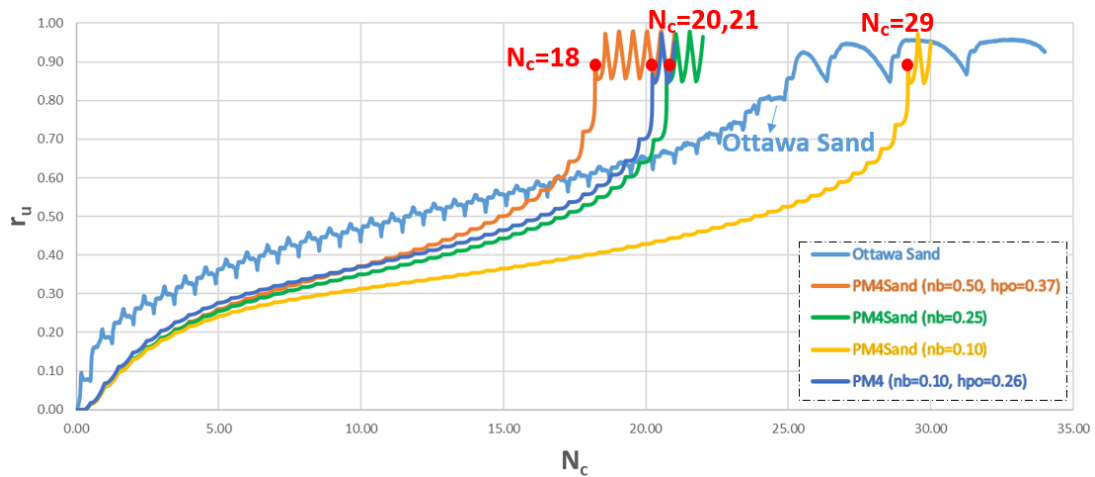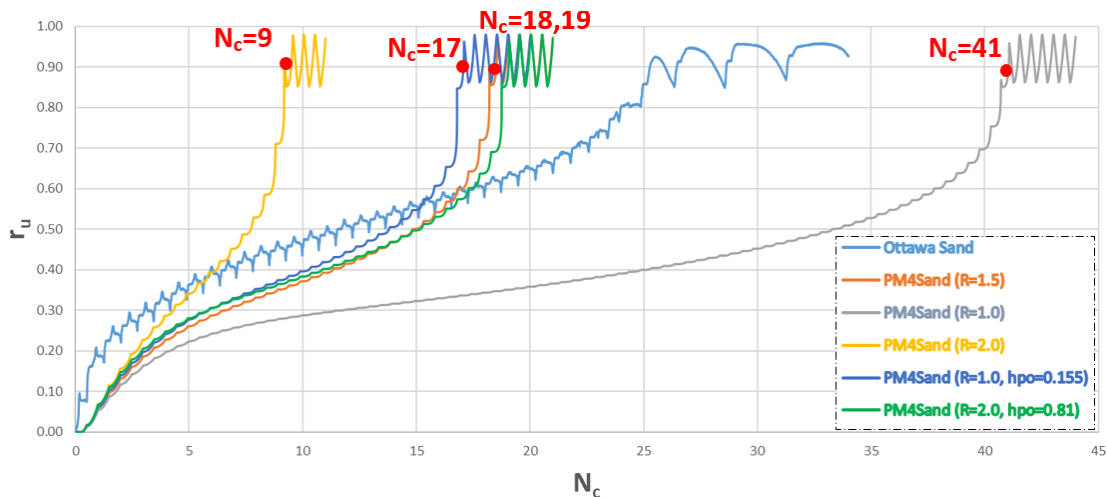
Figure 3.15: Influence of the critical state parameter R on the generation of excess pore pressures.

Related to the excess pore pressure generation (r_u) and without recalibration of h_{po}, the simulations show stiffer response for a decreasing value of R (1.0) (Figure 3.15) as more cycles are required to reach that state ($N_c = 41$) (critical state is reached slower). Conversely, the simulations show softer response for an increasing value of R (2.0), as less number of cycles are required ($N_c = 9$) (critical state is reached faster). It should be noted, that the effect of the recalibration of h_{po} parameter to the generation of excess pore pressures is almost negligible as the response remains the same.
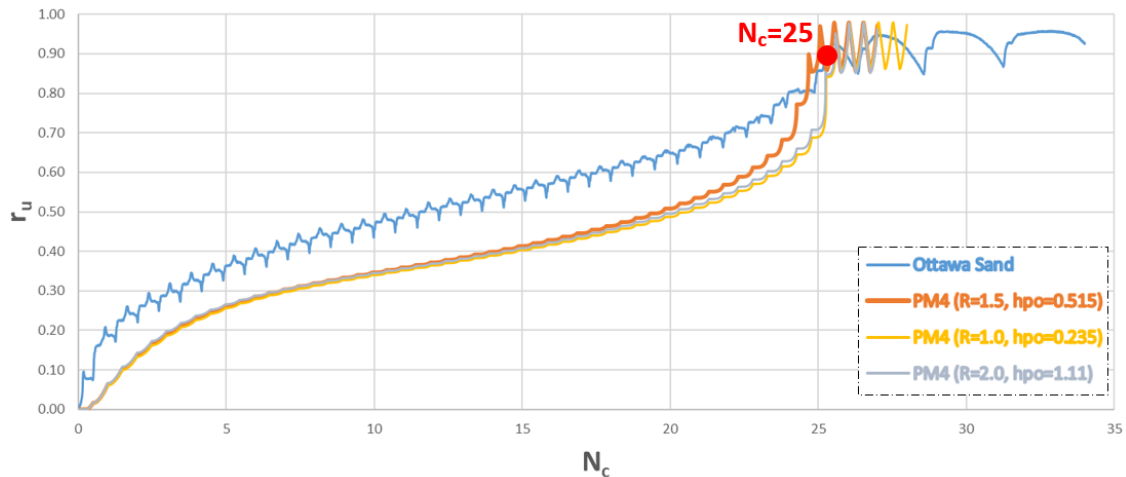
Figure 3.16: Influence of the recalibration of the contraction rate parameter h_{po} regarding the $r_u \approx 1$ criterion at $N_c = 25$ cycles at a CSR of 0.086.

It is observed, that the recalibration of the h_{po} parameter led to a precise approximation concerning the $r_u \approx 1$ state at a CSR of 0.086 (Figure 3.16) by varying the critical state parameter R. One important observation is, that the generation of excess pore pressures until $r_u \approx 1$ from PM4Sand model is almost the same for all three different set of parameters.

3.6 Evaluation of the Final Set of Parameters

Before evaluating the final set of parameters it is important to define which $CRR - N$ curves obtained from Ottawa F-65 Sand are of importance for the design of a typical hydraulic fill. In real practise the fills are placed over a $10 - 15m$ height. This means that the effective confining stress levels can reach $150kPa$ at maximum. Consequently, the first two graphs in Figure 3.2 are of primary focus for this study.

After concluding that the PM4Sand model produced far steeper cyclic strength curves than the experimental responses for $\sigma'_{vc} = 50kPa$, a new calibration process is employed. A lower dilatancy is needed to better approximate the $CRR - N$ curves for the lower confining stress of $50kPa$. This process included reduced values for the bounding surface parameter n^b (0.25 & 0.10 compared to 0.50 at default) and the recalibration of the contraction parameter h_{po} according to the first liquefaction criterion ($\gamma = 3\%$ at $N_c = 15\ cycles$). From Figure 3.17, it is clear, that lower values of n^b reduced significantly the steepness of the curves and gave a much better approximation.
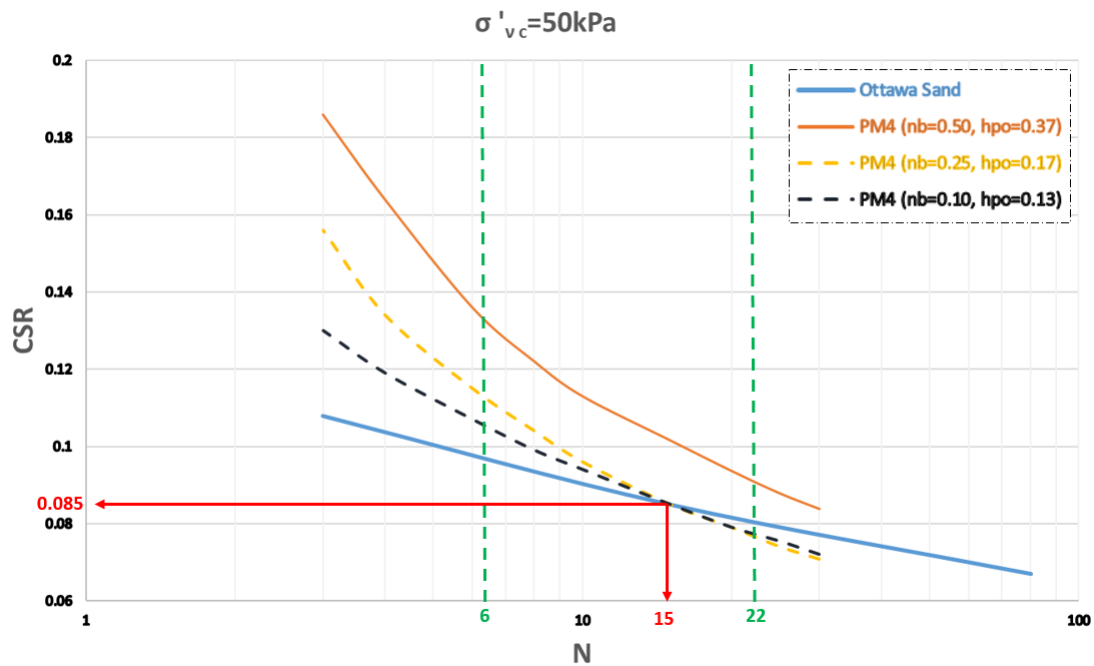
Figure 3.17: Recalibration of the h_{po} parameter by using lower values for the bounding surface parameter n^b to better approximate the curves for $\sigma'_{vc} = 50kPa$.
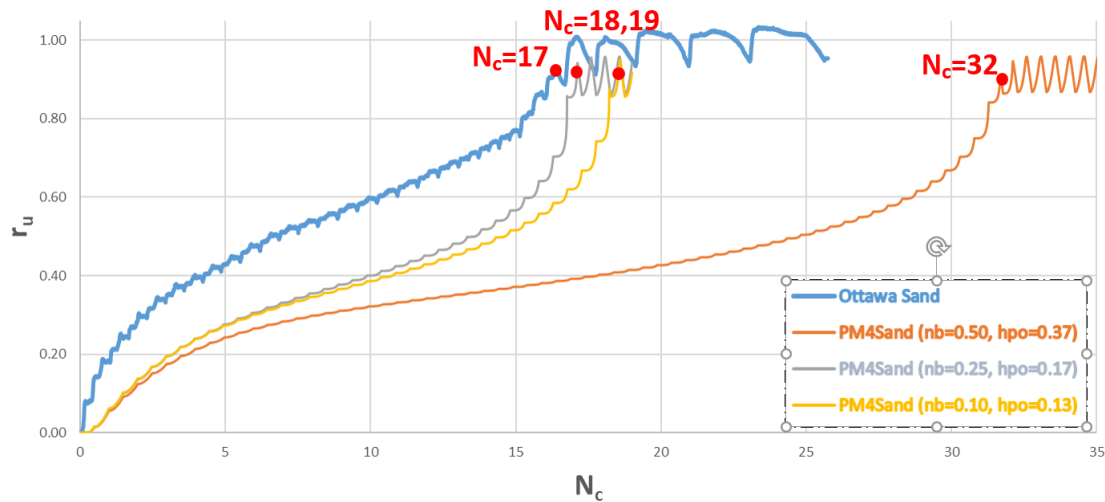
Figure 3.18: Influence of the apparent relative density D_R on the generation of excess pore pressures.

Related to the excess pore pressure generation (r_u), the recalibration of h_{po} improved the $r_u - N$ response (Figure 3.18) at a CSR of 0.080. Using lower values for the bounding surface parameter n^b led to a softer soil behavior by reducing the number of cycles required to reach an r_u of around 1.0 from $N = 31$ to $N = 17$ for $n^b = 0.25$ and to $N = 18$ for $n^b = 0.10$.

Regarding the parameter selection there are two different guidelines from which one can select the final set for the design under earthquake induced liquefaction: the $CRR - N$ response and the $r_u - N$ response. The first one gives a clear insight about the overall response of the model and is defined according to criteria that refer to reaching specific percentage of shear strains at a given number of loading cycles. The second one is based on the excess pore pressure evolution in which after a certain value is reached, liquefaction is defined. In this study the most representative guideline is reaching a pore pressure ratio of approximately unity ($r_u \approx 1$) as it the most common criterion used in real practise for the determination of liquefaction triggering in hydraulic fill structures. In this study, the parameter selection is going to be defined for both cases as after the parametric assessment a clear insight about the model performance is acquired.

Regarding the samples consolidated at $\sigma'_{vc} = 50kPa$, the same set of parameters are selected for both the $CRR - N$ response and the evolution of excess pore pressure as there was a decent match for both cases (Table 3.6). About the specimens consolidated at $\sigma'_{vc} = 100kPa$, the $CRR - N$ response was well approximated by using the initial set of parameters. However, a lower value for G_o is selected to decrease the overestimation at $N = 6$ uniform cycles. With respect to the $r_u \approx 1$ criterion it was concluded, that the model can approximate the $r_u - N$ responses with the recalibration of h_{po} parameter and varying any of the primary and secondary model parameters. For practical reasons, the concept of reducing the bounding surface parameter n^b by recalibrating h_{po} for $r_u \approx 1$ is selected as it has minor influence in the $CRR - N$ response.

	σ'_{vc}=50kPa			σ'_{vc}=100kPa	
	CRR-N	r_u=1		**CRR-N**	r_u=1
D_R	0.40	0.40	D_R	0.40	0.40
G_o	524	524	G_o	100	524
h_{po}	0.13	0.13	h_{po}	0.37	0.325
n^b	0.10	0.10	n^b	0.50	0.10
R	1.5	1.5	R	1.5	1.5

<u>Table 3.6:</u> Parametric assessment of R in the model response by using different set of parameters

3.7 Conclusions

The comparison of the experimental from the Ottawa F-65 Sand to the simulated responses from PM4Sand model gave significant insight about the capabilities and limitation of the PM4Sand model:

- The PM4Sand model well approximates the general features of cyclic loading behaviour
- The PM4Sand model produces CRR slopes which are consistent with typical cyclic strength curves from literature
- The PM4Sand model predicts steeper cyclic strength curves than in the experimental responses
- This steepness is decreased with an increasing confinement level which is means that there is a dependence of the CRR on the overburden stress level. This is consistent with (Boulanger & Ziotopoulou, 2017) according to the K_σ behaviour of the model
- In general, the model overpredicts the CRR for small number of loading cycles and underpredicts the CRR for large number of loading cycles
- The apparent relative density D_R, as a primary input parameter, has the most crucial effect in the cyclic strength and also significant influence in the generation of excess pore pressures
- The shear modulus coefficient G_o is having minor influence in the cyclic strength and is not affecting the generation of excess pore pressures at all until an r_u of around 1.0 is reached
- The overestimation of CRR at the lower confinement level ($\sigma'_{vc} = 50kPa$) can be reduced by using a lower value for the bounding surface parameter n^b and then recalibrating the contraction rate parameter h_{po} against the cyclic strength curve
- The generation of excess pore pressures in the experiments the experiments showed a relatively large buildup during first two cycles while the model carry difficulties on coping with that effect

Chapter 4: Verification of the PM4Sand Model for Static Loading

4.1 Introduction

As previously described in Chapter 3, the PM4Sand model is designed in order to capture liquefaction phenomena which occur during dynamic loading arising from an earthquake event. Moreover, in literature it is indicated, that the soil structure can also fail due to monotonic undrained loading. This type of failure is triggered when the static shear stress of a soil body required to sustain equilibrium exceeds the shear strength of the soil in its liquefied state (Chapter 2.1.2). This is most commonly known as static liquefaction or flow liquefaction and can lead to disastrous effects for the structure. The aforementioned background triggered the question on whether the PM4Sand model can replicate static liquefaction phenomena, despite the fact, that it is preliminary designed to model liquefaction arising from earthquake loading.

For the evaluation process, undrained Direct Simple Shear (DSS) tests performed on Ottawa F-65 Sand are analysed. Then, the PM4Sand model is calibrated according to the monotonic shear strength curves obtained from these tests and the responses for different conditions confinement levels are assessed. Moreover, the influence of the parameters in the response of the model is examined by performing a parametric assessment analysis.

4.2 Data Interpretation

The validation of the PM4Sand model for the simulation of static liquefaction is investigated by analysing undrained Direct Simple Shear (DSS) tests performed on Ottawa F-65 Sand (https://datacenterhub.org/resources/ottawa_f_65). The model is examined at element level to evaluate whether it can reproduce similar responses with respect to what has been observed in laboratory tests for monotonic undrained loading. The evaluation of the model's performance for the aforementioned type of sand has already been investigated by (Bastidas, 2016) using single-element numerical simulations in FLAC 2D. In her study, the input model parameters were used as obtained from the cyclic calibration while in this study a separate calibration for static loading is implemented. The validation of the PM4Sand model is accomplished using element tests in Plaxis software. The model is calibrated according to the monotonic shear strength curves obtained from lab tests and the responses for different confinement levels are assessed. Moreover, the influence of the parameters in the response of the model is examined by performing a parametric assessment analysis.

The tests were performed for loose samples normally consolidated under vertical effective stresses of $100kPa$ and $400kPa$ with an average relative density of about 31%. The samples were sheared under a constant height condition which is equivalent to an undrained shearing condition in the DSS (Dyvik, 1987).

The stress-strain responses, stress paths and evolution of excess pore water pressures are depicted in Figures 4.1-4.3. It can be observed, that the samples are reaching a Quasi-Steady State (QSS) condition at a shear strain of around 3% and 7% for an overburden stress of $100kPa$ and $400kPa$ respectively (Figure 4.1). For higher shear strains, the samples show dilative behaviour as an increase in effective stresses and a decrease in excess pore water pressures is observed for both confining stresses of $100kPa$ and $400kPa$ (Figure 4.2-4.3). The higher confined samples ($400kPa$) are showing less dilative response compared to the lower confined ($100kPa$) which is according to what has been observed in real practise.
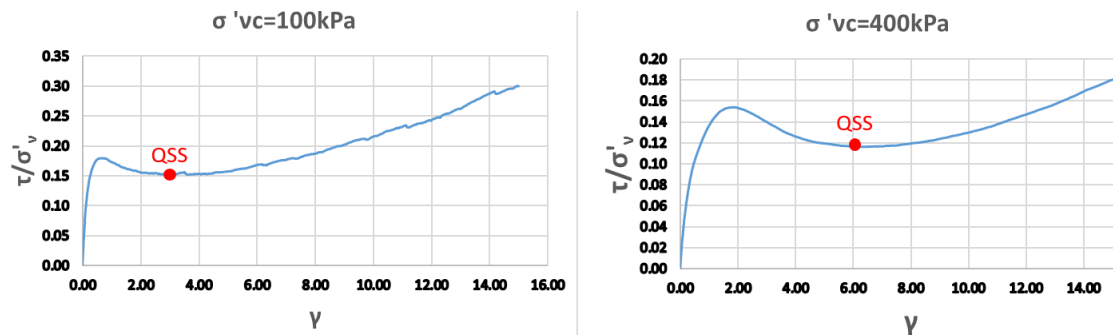
Figure 4.1 a,b: Stress-strain responses obtained from monotonic DSS tests performed on Ottawa Sand for confining stresses of 100kPa and 400kPa (Bastidas, 2016)
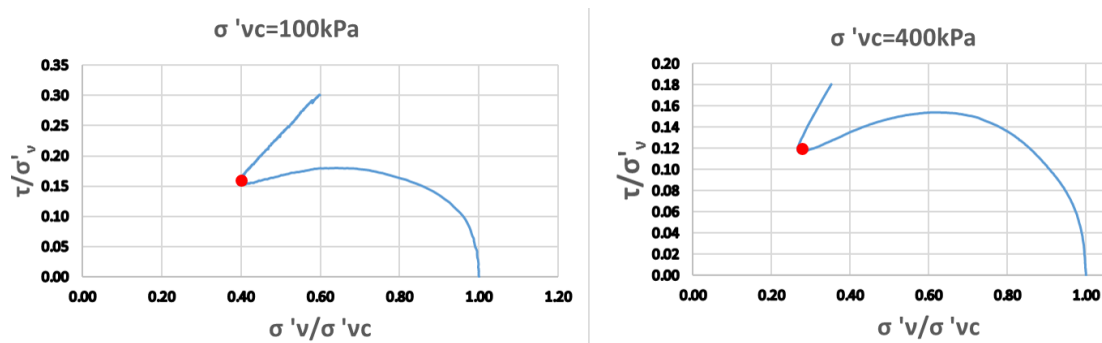
Figure 4.2 a,b: Stress paths obtained from monotonic DSS tests performed on Ottawa Sand for confining stresses of 100kPa and 400kPa (Bastidas, 2016)
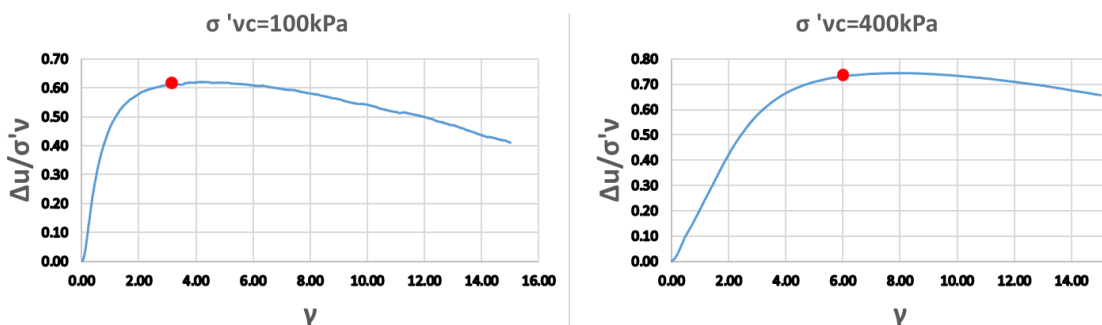
Figure 4.3 a,b: Evolution of excess pore water pressures obtained from monotonic DSS tests performed on Ottawa Sand for confining stresses of 100kPa and 400kPa (Bastidas, 2016)

4.3 Input Model Parameters

The primary model parameters D_R, G_o and h_{po} are calibrated with respect to the aforementioned laboratory test results while the secondary model parameters are used with its default values. The relative density D_R accounts for the dilatancy and the stress-strain responses of the model as it defines the tendency of the soil for contraction or dilation through the relative state parameter (Chapter 2.8.4). The shear modulus coefficient G_o controls the elastic shear modulus G at small strains (eq.(2.18)) while the contraction rate parameter h_{po} governs the evolution of plastic volumetric strains.

In the current thesis project, the apparent relative density D_R is determined as the relative density measured in the lab while the shear modulus coefficient G_o is estimated from correlation. The contraction rate parameter h_{po} is calibrated to match the peak monotonic shear strength at a confining stress of $100kPa$. Then the ability of the model to reproduce the other monotonic responses at different confining stress levels ($50kPa$, $400kPa$) is evaluated.

Apparent Relative Density D_R

This parameter is determined as the value of relative density measured in the laboratory. Thus, for the specimens confined under vertical effective stresses of $\sigma'_{vc} = 100kPa$ and $\sigma'_{vc} = 400kPa$ the relative density is defined as $D_R = 0.31$. The 'apparent' value of D_R means that the aforementioned quantities are an initial estimation for the calibration and the user can adjust them later on in order to better approximate the responses of interest.

Shear Modulus Coefficient G_o

This parameter can be related over a range of relative densities according to the following equation which is a combination between eq.(2.64) and eq.(2.67) as:

$$G_o = 167\sqrt{46D_R^2 + 2.5} \qquad (4.1)$$

Contraction rate parameter h_{po}

This parameter is adjusted to approximate the peak monotonic shear strength at a confining stress of $100kPa$.

Plaxis Soil Element Tests

The performance of the model for the liquefaction triggering under static loading is verified by reproducing undrained Direct Simple Shear (DSS) tests in the Plaxis SoilTest facility at element level. The coefficient of earth pressure at rest is defined as: $K_o = 1 - \sin(\varphi'_{cv}) = 1 - \sin 33^o = 0.46$.

The apparent relative density D_R for the confining stress levels of $\sigma'_{vc} = 100kPa$ and $\sigma'_{vc} = 400kPa$ is defined as $D_R = 0.31$. The shear modulus coefficient G_o is calculated according to eq.(4.1) as $G_o = 439$. The contraction rate parameter h_{po} is adjusted ($h_{po} = 0.15$) to

approximate the peak monotonic shear strength from Plaxis element tests at the confining stress of $\sigma'_{vc} = 100kPa$ (Figure 3.5). Then the ability of the model to reproduce the other monotonic responses at different overburden stresses ($\sigma'_{vc} = 50kPa, \sigma'_{vc} = 400kPa$) is evaluated.
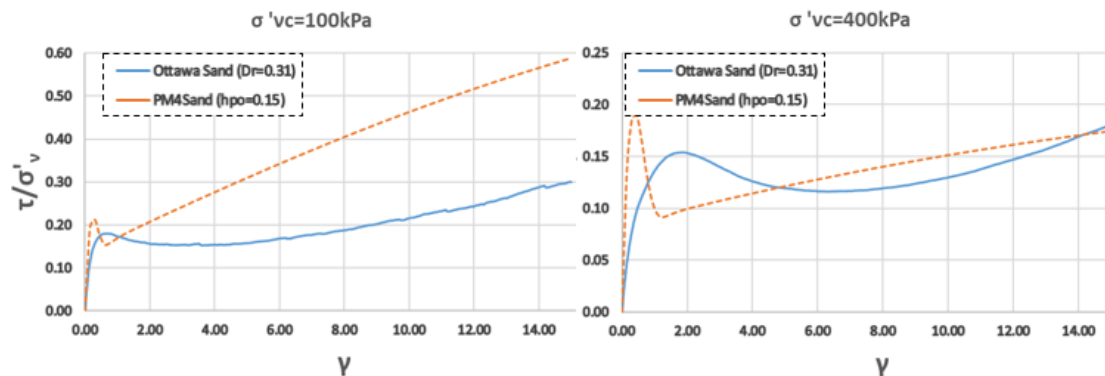
Figure 4.4 a,b: Simulated and experimental stress-strain responses at overburden stresses of 100kPa and 400kPa for D_R=0.31.
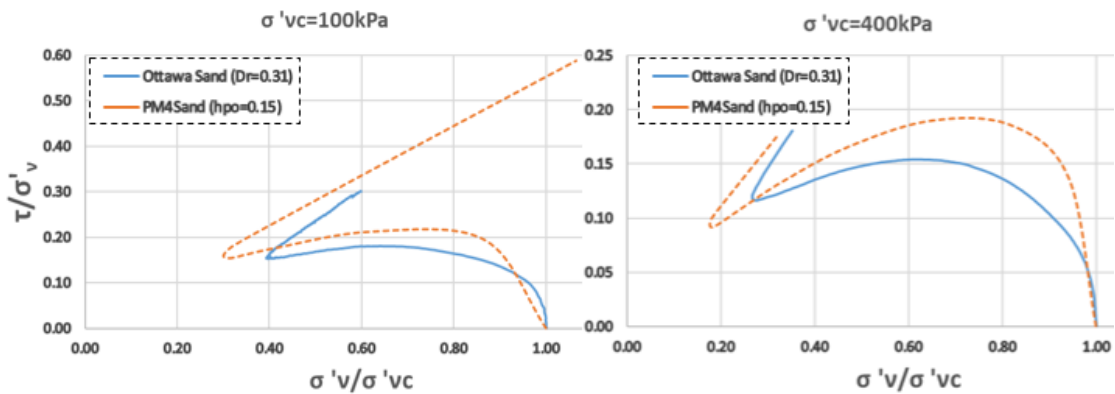
Figure 4. 5a,b: Simulated and experimental stress paths at overburden stresses of 100kPa and 400kPa for D_R=0.31.
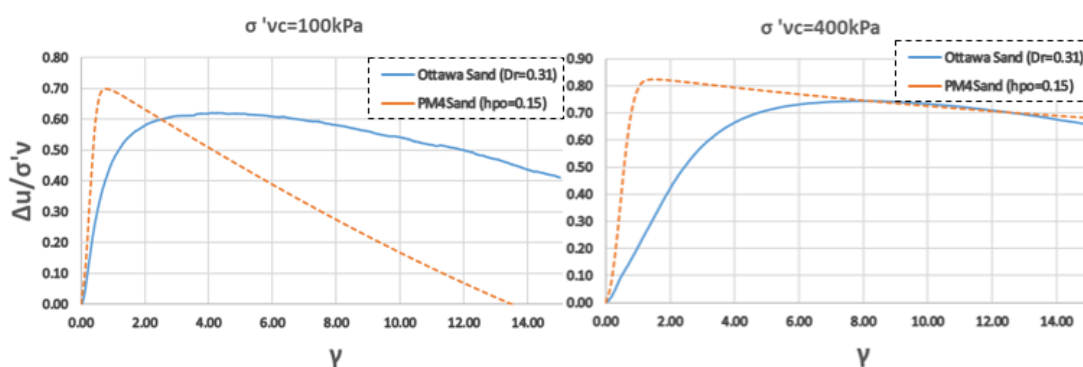
Figure 4.6 a,b: Simulated and experimental evolution of excess pore water pressures at overburden stresses of 100kPa and 400kPa for D_R=0.31.

It is observed, that the stress-strain responses produced by the PM4Sand are showing higher dilative response after the peak shear strength is reached while the laboratory responses are much smoother (Figure 4.4-4.6). This effect is decreased with an increasing overburden

stress. In the following section, a parametric assessment is performed to evaluate the influence of the parameters in the model response and whether the PM4Sand model can approximate better the experimental responses.

4.5 Influence of the Primary Model Parameters

4.5.1 Influence of D_R

The influence of the apparent relative density D_R in the model response is examined by testing six new set of parameters (Table 4.1). The first pair includes the variation of D_R by keeping all the other parameters constant at $\sigma'_{vc} = 100kPa$. In the following four sets, the recalibration of the contraction parameter h_{po} is performed by using lower values for relative density.

<p align="center">Varying D_R Recalibration of h_{po} & Varying D_R</p>

	i	ii	iii	iv	v	vi	vi
D_R	0.31	0.28	0.31	0.28	0.25	0.23	0.20
G_o	439	439	439	439	439	439	439
h_{po}	0.15	0.15	0.15	0.35	0.46	0.50	0.60

Table 4.1: Parametric assessment of D_R in the model response by using different set of parameters.

It is observed, that the initial softening behaviour is slightly decreased and the following dilative tendency is increased with an increasing relative density D_R at $\sigma'_{vc} = 100kPa$ (Figure 4.7). Consequently, the effect of relative density in the peak monotonic strength is minor while its influence is clear primarily in the post-peak response.

Regarding the recalibration of the h_{po} parameter, it is observed, that by decreasing D_R, the post-peak response is becoming considerably softer by approximating better the experimental repsonses (Figure 4.8). The simulations are showing 'limited liquefaction' behaviour for $D_R = 0.25$ and $D_R = 0.28$ and 'liquefaction' behaviour for $D_R = 0.20$ and $D_R = 0.23$ (Chapter 2.2.3).
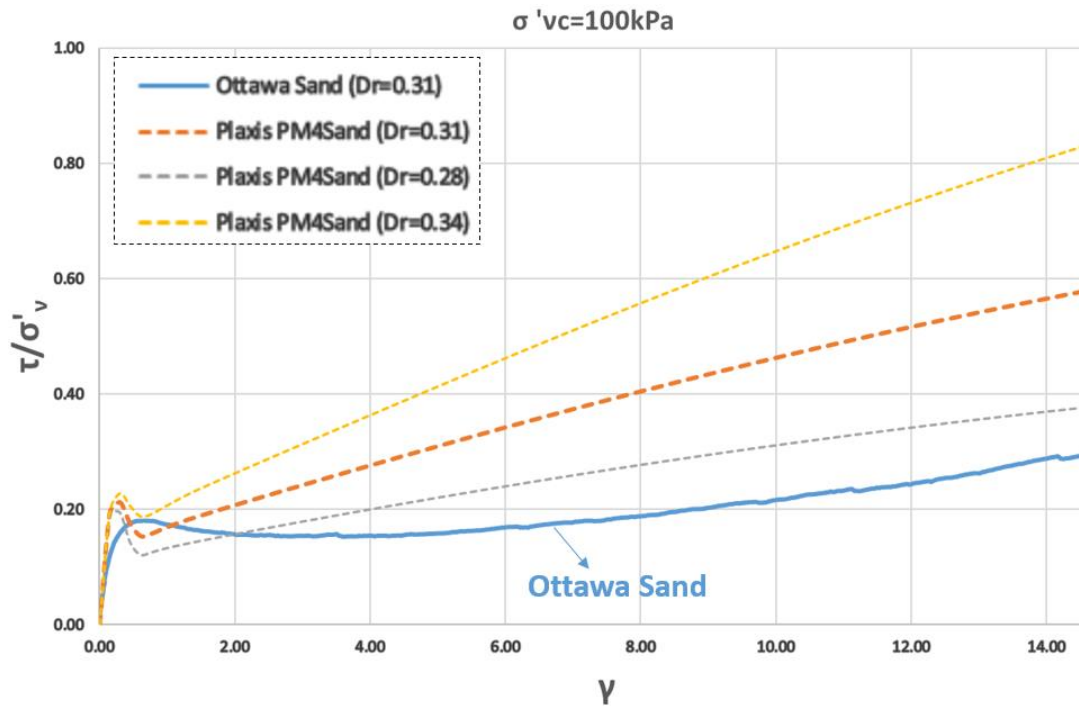
Figure 4.7: Influence of the apparent relative density D_R in the model response at $\sigma'_{vc} = 100 kPa$.
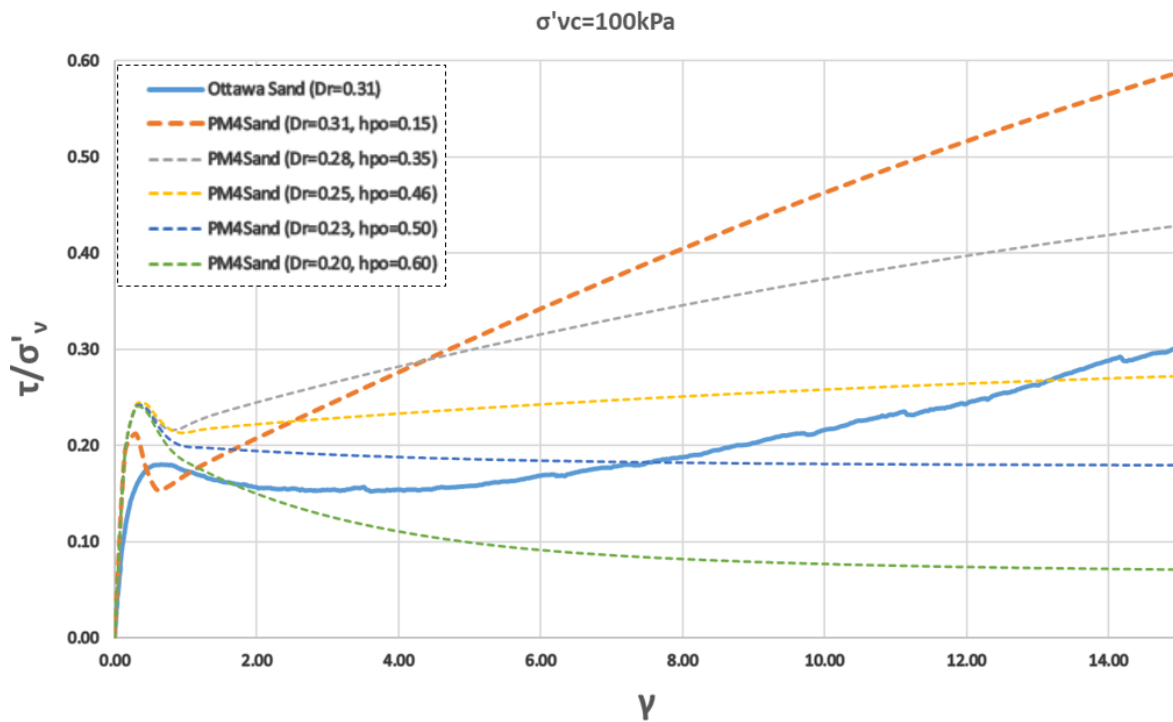
Figure 4.8: Influence of the apparent relative density D_R by recalibrating h_{po} in the model response at $\sigma'_{vc} = 100 kPa$.

4.5.2 Influence of G_o

The influence of the shear modulus coefficient G_o in the model response is examined by testing two new set of parameters (Table 4.2). This pair includes the variation of G_o by keeping all the other parameters constant.

Varying G_o

	i	ii	iii
D_R	0.31	0.31	0.31
G_o	439	250	100
h_{po}	0.15	0.15	0.15

Table 4.2: Parametric assessment of G_o in the model response by using different set of parameters

It is observed, that the G_o parameter is having a direct influence on the response at small strains. In particular, the residual strength is reached more gradually (at higher strain levels) for a decreased value of shear modulus coefficient ($G_o = 100$)(Figure 4.9).
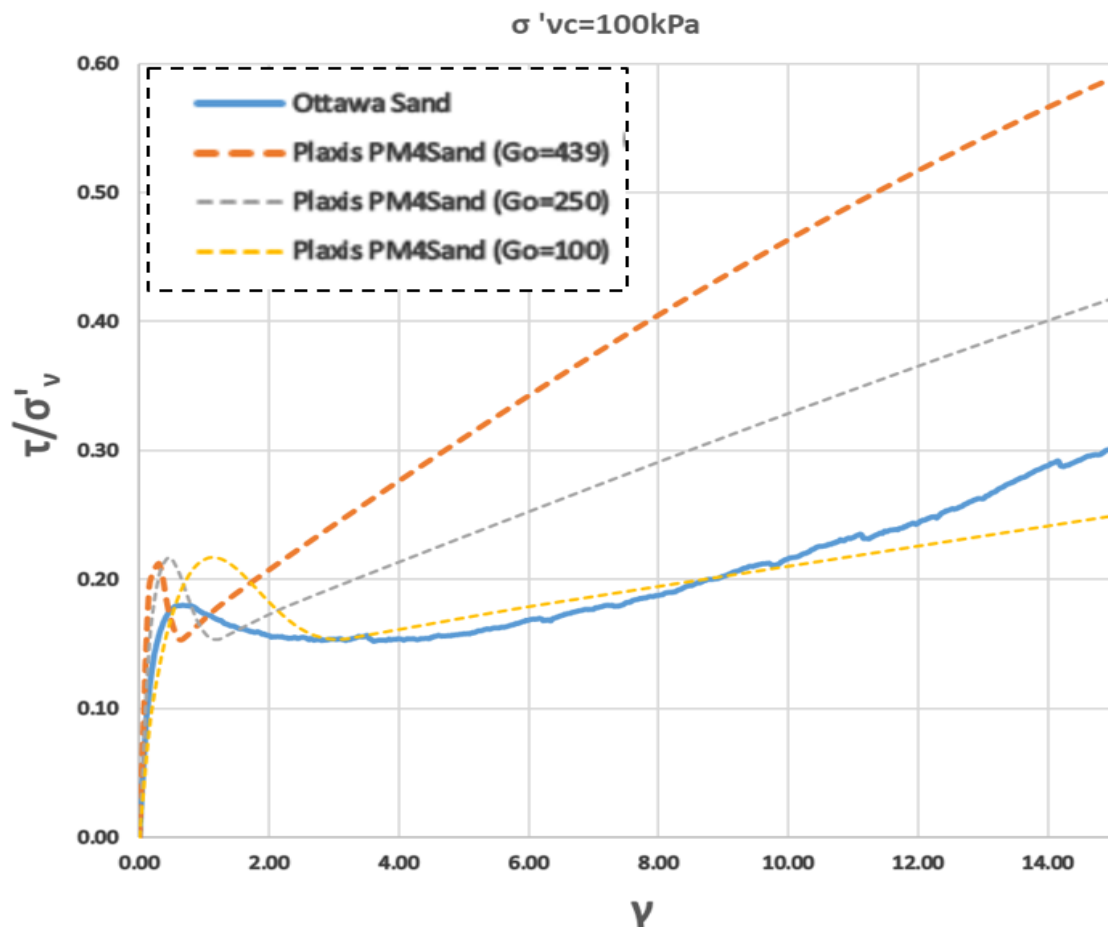
Figure 4.9: Influence of the shear modulus coefficient G_o in the model response at $\sigma'_{vc} = 100kPa$.

4.6 Influence of the Secondary Model Parameters

4.6.1 Influence of n^b

The influence of the bounding surface parameter n^b in the model response is examined by testing two new set of parameters (Table 4.3). This pair includes the variation of n^b by keeping all the other parameters constant.

	i	ii	iii
D_R	0.31	0.31	0.31
G_o	439	439	439
h_{po}	0.15	0.15	0.15
n^b	0.50	0.25	0.10

Table 4.3: Parametric assessment of $\boldsymbol{n^b}$ in the model response by using different set of parameters

It is observed, that the initial softening behaviour is becoming trivial for all values of bounding surface parameter (Figure 4.10). The dilative tendency that is followed after the peak shear strength is reached, is decreased with a decreasing value of n^b. This can be attributed to the fact, that for lower values of n^b (and by considering that the default value of dilatancy surface parameter n^d is 0.10) the bounding surface (M^b) lies closer to the dilatancy surface (M^d) (Figure 2.22). Consequently, once the stress state crosses M^d, the M^b is then being approached faster. Therefore, using lower values of n^b leads to a softer post-peak response which is closer to the experimental results.
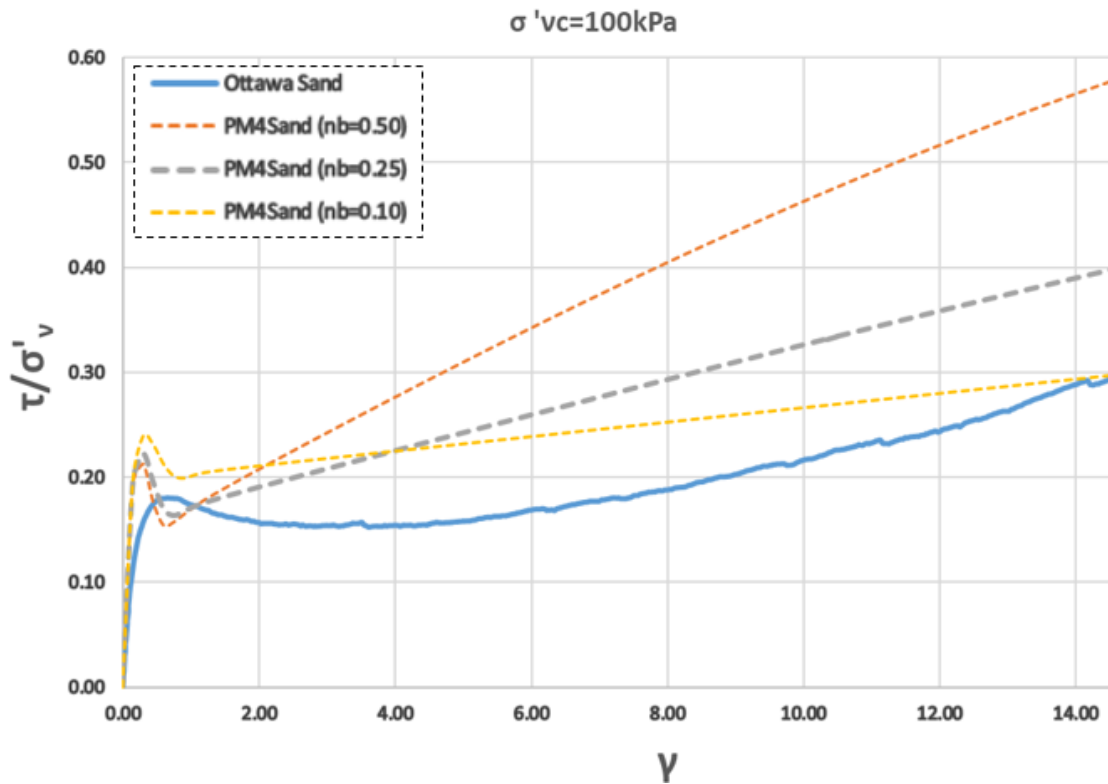
Figure 4.10: Influence of the bounding surface parameter n^b in the model response at $\sigma'_{vc} = 100kPa$.

4.6.2 Influence of R

The influence of the critical state parameter R in the model response is examined by testing six new set of parameters (Table 4.4). The first pair includes the variation of R by keeping all the other parameters constant for all different confining stress levels. In the following four sets, the recalibration of the contraction parameter h_{po} is performed by using lower values for R at $\sigma'_{vc} = 100kPa$.

Varying R   Recalibration of h_{po} & Varying R

	i	ii	iii	iv	v	vi
D_R	0.31	0.31	0.31	0.31	0.31	0.31
G_o	439	439	439	439	439	439
h_{po}	0.15	0.15	0.15	0.38	0.55	0.70
R	1.50	1.00	2.00	1.75	2.00	2.25

Table 4.4: Parametric assessment of R in the model response by using different set of parameters

It is observed, that the initial softening behaviour along with the following dilative tendency is reduced with an increasing R (Figure 4.11). This can be attributed to the fact, for higher

values of R the critical state line is moving downwards (Figure C.1). This will lead to a decrease in $D_{R,CS}$ which gives a lower relative state parameter ξ_R (eq. C.2) enabling the model to approach the CSL faster. From Figure 4.11, it is clear, that the effect of the critical state parameter R is significant both in the peak monotonic strength and in the post-peak response.

Regarding the recalibration of the h_{po} parameter, it is observed, that by increasing R, the post-peak response is becoming considerably softer by approximating better the experimental responses (Figure 4.12). The simulations are showing 'limited liquefaction' behaviour for $R = 1.75$ and 'liquefaction' behaviour for $R = 2.0$ and $R = 2.25$ (Chapter 2.2.3).
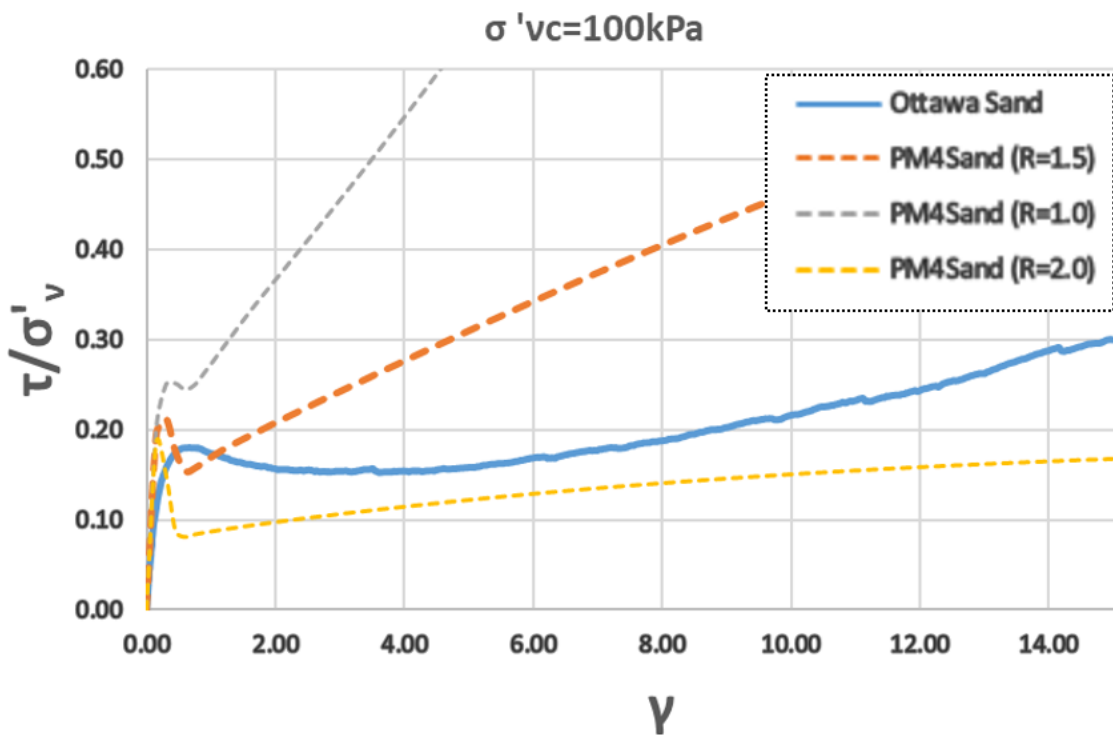
Figure 4.11: Influence of the critical state parameter $\boldsymbol{R}$ in the model response at $\sigma'_{vc} = 100kPa$.
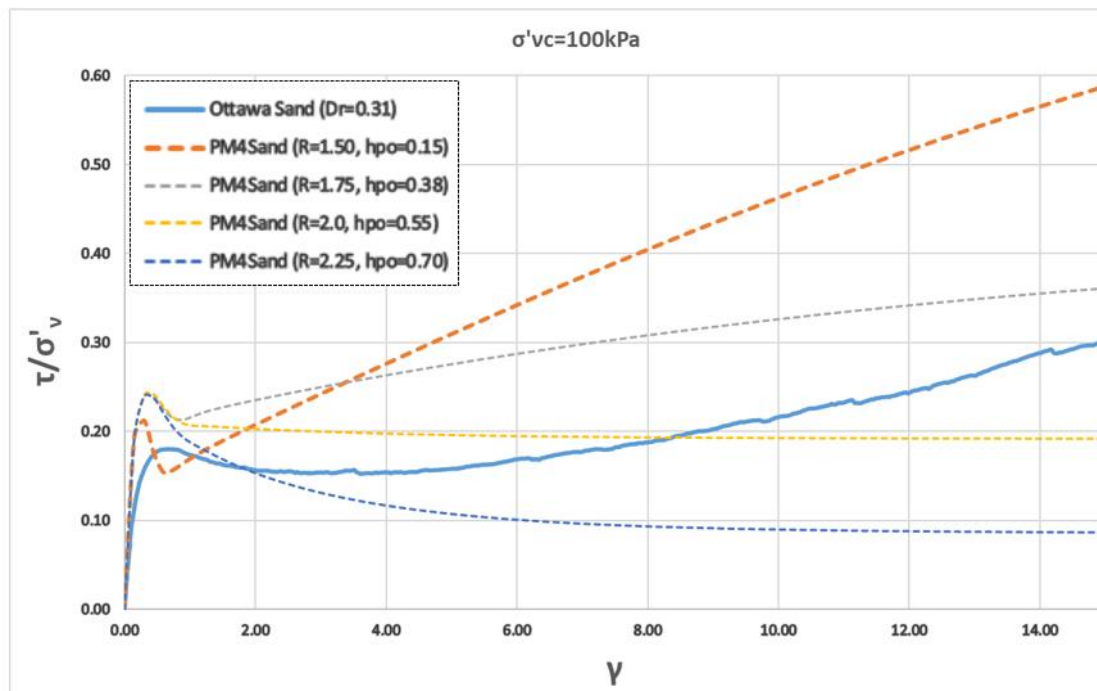
Figure 4.12: Influence of the critical state parameter R by recalibrating h_{po} in the model response at $\sigma'_{vc} = 100kPa$.

4.6.2 Influence of Q

The influence of the critical state parameter Q in the model response is examined by testing six new set of parameters (Table 4.4). The first pair includes the variation of Q by keeping all the other parameters constant for all different confining stress levels. In the following four sets, the recalibration of the contraction parameter h_{po} is performed by using lower values for Q at $\sigma'_{vc} = 100kPa$.

	i	ii	iii	iv	v	vi
D_R	0.31	0.31	0.31	0.31	0.31	0.31
G_o	439	439	439	439	439	439
h_{po}	0.15	0.15	0.15	0.33	0.42	0.55
Q	10.00	9.00	11.00	9.50	9.00	8.50

Table 4.5: Parametric assessment of Q in the model response by using different set of parameters

It is observed, that the initial softening behaviour along with the following dilative tendency is reduced with an decreasing Q (Figure 4.13). This can be attributed to the fact, for lower values of Q the critical state line is moving downwards (Figure C.1). This will lead to a decrease in $D_{R,CS}$ which gives a lower relative state parameter ξ_R (eq. C.2) enabling the model to

approach the CSL faster. From Figure 4.13, it is clear, that the effect of the critical state parameter Q is significant both in the peak monotonic strength and in the post-peak response. Moreover, it is important to note, that the effect of Q in the model response is realized with a lower rate compared to the corresponding effect of the parameter R (Figure 4.11).

Regarding the recalibration of the h_{po} parameter, it is observed, that by decreasing Q, the post-peak response is becoming considerably softer by approximating better the experimental responses (Figure 4.14). The simulations are showing 'limited liquefaction' behaviour for $Q = 9.5$ and $Q = 9.0$ 'liquefaction' behaviour for $Q = 8.5$ (Chapter 2.2.3).
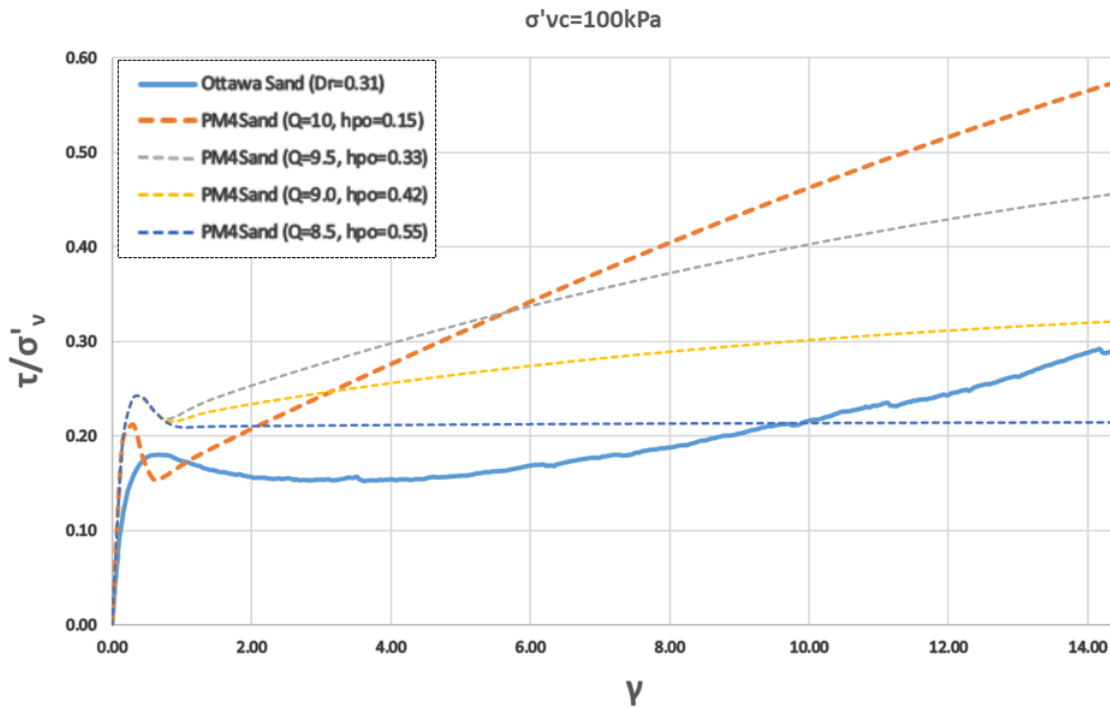
Figure 4.13: Influence of the critical state parameter Q in the model response at $\sigma'_{vc} = 100kPa$.
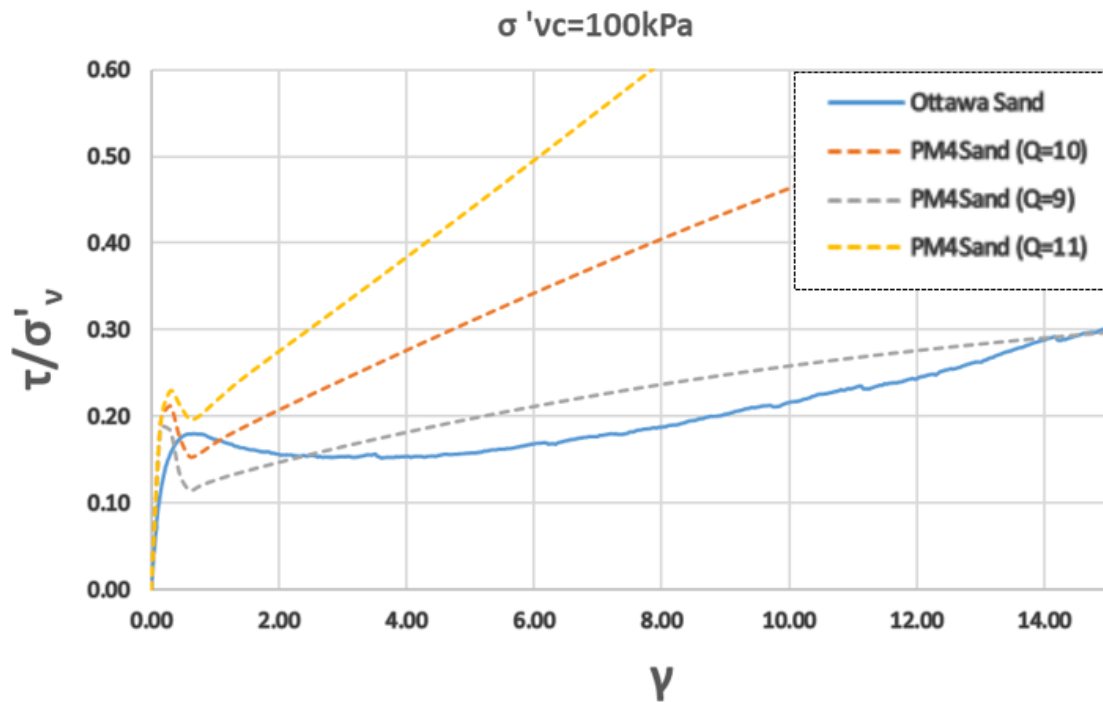
Figure 4.14: Influence of the critical state parameter Q by recalibrating h_{po} in the model response at $\sigma'_{vc} = 100kPa$.

4.6.3 Influence of ф'$_{cv}$

The influence of the critical state friction angle φ'_{cv} in the model response is examined by testing two new set of parameters (Table 4.6). This pair includes the variation of φ'_{cv} by keeping all the other parameters constant.

Varying ф'$_{cv}$

	i	ii	iii
D_R	0.31	0.31	0.31
G_o	439	439	439
h_{po}	0.15	0.15	0.15
ф'$_{cv}$	33	30	36

Table 4.6: Parametric assessment of φ'_{cv} in the model response by using different set of parameters

It is observed, that the initial softening behaviour along with the following dilative tendency is slightly reduced with a decreasing value of φ'_{cv}. (Figure 4.15). Consequently, the effect of the critical state friction angle is of less significancet for both the peak monotonic strength and the post-peak response.
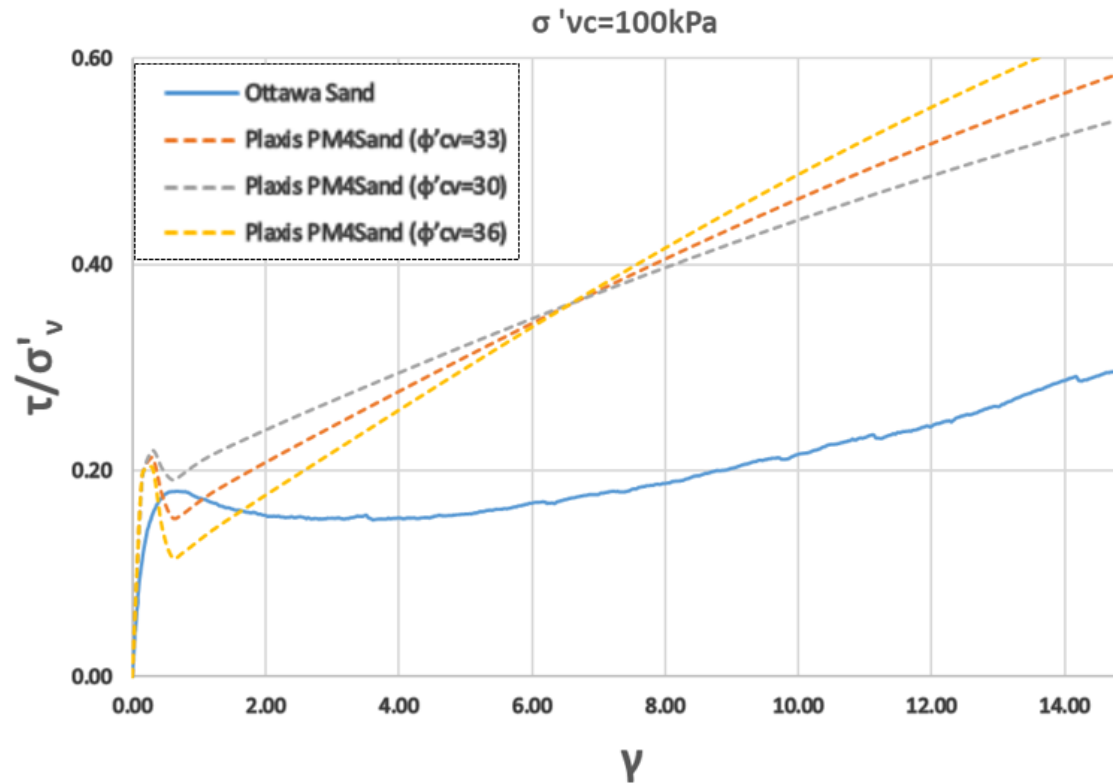
Figure 4.15: Influence of the critical state parameter $\boldsymbol{\varphi'_{cv}}$ in the model response at $\sigma'_{vc} = 100kPa$.

4.7 Conclusions

- Plaxis PM4Sand model approximates well the general features of static loading
- Regarding the initial parametric selection, the model shows limited liquefaction behaviour in which the dilative (or post-peak) response after the quasi-steady state is reached is higher than in the experimental responses
- This high dilative tendency is decreased with an increasing confinement level which means that higher overburden stresses suppress the dilative response
- The following dilative (or post peak) response after the peak shear strength is reached can be smoothened and thus approximate better the experimental responses by:

  - using lower values for the apparent relative density D_R and recalibrating the contraction rate parameter h_{po}
  - using lower values for the bounding surface parameter n^b
  - using higher values for the critical state parameter R and recalibrating the contraction rate parameter h_{po}
  - using lower values for the critical state parameter Q and recalibrating the contraction rate parameter h_{po}

Chapter 5: Simulation of Earthquake Induced Liquefaction in Hydraulic Fills

5.1 Introduction

In this chapter the performance of the Plaxis PM4Sand model for the prediction of earthquake induced liquefaction in hydraulic fills is evaluated. Several different seismic motions characterized by various fundamental frequencies and peak ground accelerations are analysed. Then, the influence of these earthquake motions in the liquefaction triggering of hydraulic fills placed over different relative densities are evaluated. The acceleration-time signals are obtained from a large database regarding strong-motion seismographs (www.kyoshin.bosai.go.jp) and need to be initially evaluated before applied to the model.

The hydraulic fill structure is modelled in Plaxis as a 1-D soil column. The stratigraphy of the soil column is interpreted based on correlations from the literature. This will provide the appropriate information for the estimation of the required input parameters and also for the calibration of the PM4Sand model parameters that are going to be used for the liquefiable layers. The susceptibility of the hydraulic fill to liquefaction which is placed over a different range of relative densities is initially assessed with the NCEER method. The fill layers that are prone to liquefy are modelled with PM4Sand model whereas the layers that are not susceptible to liquefaction are modelled with Hardening Soil Small (HSS) model.

The acceleration-time signals are applied as a dynamic displacement on bedrock level which generates seismic waves that propagate towards the surface through the soil layers. After applying the Fourier Transform in each signal, the frequency domain is obtained from which dominant frequencies are identified. These frequencies are required to determine the size of the mesh-elements and the dynamic properties of the soil column.

The dynamic analysis is performed with and without consolidation and the lateral boundaries used are tied degrees of freedom. This type of boundary is ideal for 1-D wave propagation which allows to reduce the geometry of the problem. The results in terms of the development of excess pore pressures are examined throughout the whole earthquake motion and the differences between those two modes are investigated. The onset of liquefaction in the hydraulic fill is captured when the excess pore pressure ratio has reached a value of around 1.0 ($r_u \approx 1$).

5.2 Input Ground Motion

The acceleration-time motions are obtained from the database (www.kyoshin.bosai.go.jp). In particular, sevel different earthquake signals are analysed with a magnitude of $M_w = 8$. The maximum horizontal accelerations were measured at bedrock level and the values are ranging between $a_{max} = 0.14g$ and $a_{max} = 0.22g$. Moreover, the dominant frequencies acquired after applying the Fourier Transform in each of the acceleration-time signals are varying between $f_{fund} = 0.37Hz$ and $f_{fund} = 5.47Hz$. The earthquake motions can be

distinguished into two classes with respect to this fundamental frequency content. The first class is comprised by motions characterized by low fundamental frequencies ($f_{fund} = 0.37Hz$, $f_{fund} = 0.40Hz$, $f_{fund} = 0.59Hz$ and $f_{fund} = 0.70Hz$) while the second containts signals of higher dominant frequencies ($f_{fund} = 3.31Hz$, $f_{fund} = 3.60Hz$ and $f_{fund} = 5.47Hz$). Before applying the signal to Plaxis an evaluation process is required which will determine whether the signal is going to be modified or applied as initially measured. This process consists of the following steps:

- The acceleration motions can be cut to capture only the strong ground motion. In this analysis, the duration of the acceleration motions is ranging between $140sec$ and $200sec$. The signals are going to be cut at $100sec$ as after this point the ground shaking is negligible (Appendix A.1 – Figure A.1-A.7)
- If the acceleration in the end of the ground motion is zero the velocity should be also zero. A non-zero value of the velocity could be due to noise or disturbance of the wave propagation. In this case, filtering and baseline correction should be applied to the acceleration-time signal. As this was the case, a bandpass Butterworth filter is applied in which the frequency range was set between $0.1Hz$ and $11Hz$. The Butterworth filter is a type of signal processing filter designed to have a frequency response as flat as possible in the passband.
- The acceleration-time history to be applied in the model represents the signal at bedrock level. In case the ground motion is obtained at surface, a deconvolution process should be applied to capture the signal variation from bedrock to surface due to the different dynamic soil properties of the layers. In this case, the deconvolution is not applied because the acceleration ground motion corresponds to the signal at bedrock.
- It is known that the filtering or the correction process may modify the initial input signal, especially in terms of Peak Ground Acceleration (PGA). Thus, the new signal needs to be scaled to the original PGA.
- After finishing the filtering and correction process, the input signal is applied in Plaxis at bedrock level as a dynamic displacement. This generates seismic waves propagating towards surface through the model. Moreover, Fourier Transform is applied to the acceleration signal in order to obtain the frequency amplitude spectrum from which the fundamental frequencies can be defined (Appendix A.1 – Figure A.8-A.14). These frequencies are required to define the Rayleigh damping coefficients in Chapter 5.4.4

5.3 Soil Column Interpretation

The hydraulic fill structure is simulated as a 1-D soil column (Figure 5.1). The fill material consists of sand which is placed $1m$ over water using the discharge pipeline method with $D_R = 60\%$ and $10m$ underwater using the rainbowing method with different relative densities varying between $D_R = 30\%$ and $D_R = 60\%$. For deeper layers the relative density is

apparently increased ($D_R = 70\%$ from 11m to 26m and $D_R = 80\%$ from 26m to 41m) and the bedrock level is assumed to be at 41m depth.

The strength parameters of the soil column are calculated as a function of the relative density from eq.(5.1-5.3). The latter is set equal to the relative density of the considered layer (Figure 5.3) since there are no available laboratory or in-situ data.
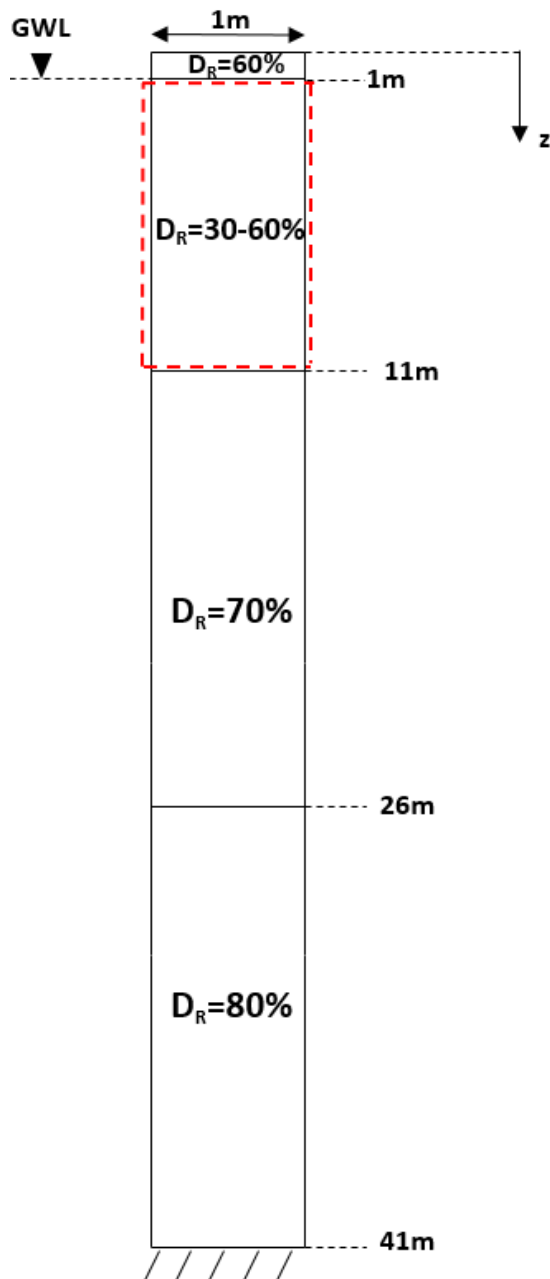
Figure 5.1: Simulated hydraulic fill of 11m as a 1-D soil column.

The friction angle and the unit weight are calculated according to (Brinkgreve, R.B.J.,2010) as:

$$\varphi' = 28 + 12.5\frac{D_R}{100} \qquad [^0] \qquad (5.1)$$

$$\gamma_{unsat} = 15 + 4\frac{D_R}{100} \qquad [kN/m^3] \qquad (5.2)$$

$$\gamma_{sat} = 19 + 1.6\frac{D_R}{100} \qquad [kN/m^3] \qquad (5.3)$$

D_R (%)	Top (m)	Bottom (m)	Description	ϕ' (°)	γ_{unsat} (KN/m^3)	γ_{sat} (KN/m^3)
60	0	1	Medium dense	36	17,4	20,0
30	1	11	Loose	32	16,2	19,5
40	1	11	Loose	33	16,6	19,6
50	1	11	Medium dense	34	17	19,8
60	1	11	Medium dense	36	17,4	20,0
70	11	26	Dense	37	17,8	20,1
80	26	41	Dense	38	18,2	20,3

Table 5.1: Interpretation of the soil column.

Liquefaction Susceptibility

The liquefaction susceptibility of the hydraulic fill and of the whole soil column is initially evaluated with the NCEER method. The Cyclic Stress Ratio (CSR) of each layer is calculated according to the semi-empirical method (Seed & Idriss, 1971) from eq.(2.7). The Cyclic Resistance Ratio (CRR) is determined from eq.(2.24) where factors concerning the earthquake magnitude, the confinement level and sloping ground effects are considered.

As level ground conditions was the case, the K_a factor is taken as unity. The $CRR_{7.5}$ is calculated from eq.(2.11) where the $(N_1)_{60}$ value is assessed from eq.(2.14) for each value of relative density D_R. Then the factory of safety FS is determined from eq.(2.23) which provides a clear insight for the layers that are prone to liquefy ($FS < 1$).

The results of the liquefaction susceptibility analysis for the hydraulic fill earthquake are given in Appendix A.2 (Table A.16-A.19) regarding the seven earthquake motions. The results of the whole soil column for a typical fill of $D_R = 30\%$ relative density are indicated in Appendix A.2 (Table A.15). Note that, in the aforementioned Tables, the results for four acceleration motions are indicated as some of the signals have the same peak ground acceleration. It is clear that, according to NCEER method, the liquefaction potential of the hydraulic fill placed with relative densities between $D_R = 30\%$ and $D_R = 60\%$ for all different seismic motions is high ($FS < 1$).

5.4 Plaxis 2D Modelling

5.4.1 Soil Layers with Hardening Soil Small (HSS) Model

The Hardening Soil Small (HSS) model is used to model all layers in static analysis as well as for soil layers in dynamic analysis that are not susceptible to liquefaction ($FS > 1$). The layers with high liquefaction potential ($FS < 1$) are modelled with the PM4Sand model. The following correlations are used to define the input parameters of the HSS model. These parameters are mainly dependent on the relative density of the soil and given by (Brinkgreve, R.B.J.,2010) as:

$$E_{50}^{ref} \approx 60 D_R \qquad (5.4)$$

$$E_{oed}^{ref} = E_{50}^{ref} \approx 60 D_R \quad (5.5)$$

$$E_{ur}^{ref} \approx 2 E_{oed}^{ref} \quad (5.6)$$

$$G_o^{ref} = 60 + 68 \frac{D_R}{100} \quad (5.7)$$

$$\gamma_{0.7} = \left(2 - \frac{D_R}{100}\right) 10^{-4} \quad (5.8)$$

$$m = 0.7 - \frac{D_R}{320} \qquad (5.9)$$

$$K_{o,nc} = 1 - \sin \varphi' \quad (5.10)$$

$$R_f = 1 - \frac{D_R}{800} \qquad (5.11)$$

where E_{50}^{ref} is the secant stiffness from triaxial test at reference pressure, E_{oed}^{ref} is the tangent stiffness from oedometer test at reference pressure, E_{ur}^{ref} is the unloading/reloading stiffness, G_o^{ref} is the reference shear stiffness at small strains, $\gamma_{0.7}$ is the shear strain in which the shear modulus G has reduced to 72.2%, m is the rate of stress-level dependency in stiffness behaviour, $K_{o,nc}$ is the horizontal to vertical ratio in primary 1D compression and R_f is the failure ratio.

The list of the Hardening Soil Small (HSS) parameters for all soil layers that are going to be used for the analysis are indicated in Table 5.2.

Soil column	Depth (m)	$E_{50,ref}$ (kPa)	$E_{oed,ref}$ (Kpa)	$E_{ur,ref}$ (kPa)	$G_{o,ref}$ (kPa)	$\gamma_{0.7}$ (-)	m (-)	$K_{o,nc}$ (-)	R_f (-)
$D_R=60\%$	0-1	36000	36000	72000	100800	0,00014	0,51	0,42	0,93
$D_R=30\%$	1-11	18000	18000	36000	80400	0,00017	0,61	0,46	0,96
$D_R=40\%$	1-11	24000	24000	48000	87200	0,00016	0,58	0,46	0,95
$D_R=50\%$	1-11	30000	30000	60000	94000	0,00015	0,54	0,44	0,94
$D_R=60\%$	1-11	36000	36000	72000	100800	0,00014	0,51	0,42	0,93
$D_R=70\%$	11-26	42000	42000	84000	107600	0,00013	0,48	0,42	0,91
$D_R=80\%$	26-41	48000	48000	96000	114400	0,00012	0,45	0,38	0,90

Table 5.2: Hardening Soil Small (HSS) parameters for each soil layer.

5.4.2 Soil Layers with PM4Sand Model

The PM4Sand model is used in dynamic analysis to model the soil layers that are susceptible to liquefaction ($FS < 1$). The relevant layers consist of the hydraulic fill ($D_R = 30 - 60\%$) which is extended from $1m$ to $11m$ depth (Figure 5.1).

Apparent Relative Density D_R

The apparent relative density (D_R) of the hydraulic fill is taken as the relative of the whole layer: $D_R = 0.30$, $D_R = 0.40$, $D_R = 0.50$ and $D_R = 0.60$ for each case.

Shear Modulus Coefficient G_o

The shear modulus coefficient (G_o) is calculated from eq.(3.1) as a function of relative density (D_R).

Contraction Rate Parameter h_{po}

The contraction rate parameter (h_{po}) is calibrated to match specific Cyclic Resistance Ratio (CRR) in Plaxis element test corresponding to a $\gamma = 3\%$ failure criterion at $N_c = 15$ loading cycles in direct simple shear loading. The calibration is done for the middle of the fill layer which is at $6m$ depth. It is important to note, that the target CRR (Table 5.3) considered for the calibration of h_{po} takes into account the earthquake magnitude (MSF) and overburden stress effects (K_σ) as shown in eq.(2.44).

Soil column	Depth(m)	$CRR_{7.5}$	MSF	K_σ	CRR
$D_R=30\%$	6	0,066	0,88	1,04	0,060
$D_R=40\%$	6	0,091	0,88	1,05	0,083
$D_R=50\%$	6	0,127	0,88	1,05	0,117
DR=60%	6	0,176	0,88	1,06	0,164

Table 5.3: Target CRR from which to calibrate the contraction rate parameter h_{po}.

In the following table the primary set of the model parameters used in PM4Sand are indicated with the secondary parameters kept as default (Boulanger & Ziotopoulou, 2015).

Soil column	Depth(m)	D_R	G_o	h_{po}
D_R=30%	1-11	0,30	430	0,15
D_R=40%	1-11	0,40	524	0,25
D_R=50%	1-11	0,50	624	0,33
D_R=60%	1-11	0,60	729	0,41

Table 5.4: Primary set of model parameters used in PM4Sand.

5.4.3 Mesh Generation and Time Step

In dynamic finite element models, the determination of the size of the mesh-elements along with the time step of the calculation is of high importance to ensure proper seismic wave propagation through the model. This means that the element size would preferably not be too large. However, a too small element size would lead to large computational time so the user has to select an optimum average element size for each layer.

The maximum element size per layer is defined according to (Kuhlmeyer & Lysmer, 1973) as:

$$\Delta l_{average} \leq \frac{\lambda}{8} = \frac{v_{s,layer}}{8 f_{max}} \quad (5.12)$$

where λ is the wavelength, $v_{s,layer}$ is the shear wave velocity of the considered layer and f_{max} is the maximum frequency component of the input signal. The maximum frequency component is obtained after applying the Fourier Transform on the acceleration signal (Figure 5.2) as $f_{max} = 11Hz$.

The dynamic time step in Plaxis is set equal to the time step of the acceleration input signal. In this case, the time step is $\Delta t = 0.005s$. Moreover, the waves have to be prevented from traveling within more than one element per time step. This can be evaluated by the following expression where the critical time step is defined as:

$$\Delta t \leq \frac{\Delta l_{average}}{v_{s,layer}} \quad (5.13)$$

The shear wave velocity for each layer is calculated as:

$$v_{s,layer} = \sqrt{\frac{G}{\rho}} \quad (5.14)$$

where G is the elastic shear modulus and ρ is the density of the soil layer.

The elastic shear modulus G for the layers modelled with HSS small model is calculated as:

$$G = G_{o,HS} = G_{o,ref} \left(\frac{\sigma'_3 \sin(\varphi')}{p_{ref} \sin(\varphi')} \right)^m \quad (5.14)$$

where p_{ref} is the reference confining pressure taken as 100kPa and σ'_3 is the minor principal stress in a triaxial test.

The elastic shear modulus G for the fill layer modelled with PM4Sand model is calculated in two different ways: $i)$ according to eq.(2.18) where G_o is taken from eq.(3.1) (PM4Sand model formulation) and $ii)$ according to eq.(5.14) (HSS Small model formulation). Then, the maximum element size and maximum time step for each layer is computed from eq.(5.12) and eq.(5.13) and the results are indicated in Table 5.5. It is important to note that the value of $v_{s,layer}$ in the aforementioned equations is set equal to the average value of shear wave velocity for the considered soil layer. The analytical calculations for the whole soil column are indicated in Appendix A.2.

Soil column	$v_{s,average}$ (m/s)	f_{max} (Hz)	Δl_{max} (m)	Δt_{max} (s)	Soil column	$v_{s,average}$ (m/s)	f_{max} (Hz)	Δl_{max} (m)	Δt_{max} (s)
D_R=60%	109	11	1,23	0,011	D_R=60%	137	11	1.61	0.011
D_R=30%	129	11	1,47	0,011	D_R=30%	183	11	2.08	0.011
D_R=40%	141	11	1,60	0,011	D_R=40%	190	11	2.16	0.011
D_R=50%	153	11	1,74	0,011	D_R=50%	197	11	2.24	0.011
D_R=60%	164	11	1,86	0,011	D_R=60%	203	11	2.31	0.011
D_R=70%	229	11	2,61	0,011	D_R=70%	283	11	3.21	0.011
D_R=80%	265	11	3,01	0,011	D_R=80%	328	11	3.73	0.011

Table 5.5 i), ii): Average shear wave velocity, maximum frequency, maximum element size, maximum time step for each layer by taking into account the elastic shear modulus G calculated according to i) PM4Sand model and ii) HSS Small model.

5.4.4 Rayleigh Damping

In Plaxis, two major damping components are introduced, representing the dissipation of energy from an earthquake due to the wave propagation through the model. The first one is the hysteric damping which accounts for damping at large strains. However, the soil behaviour may be irreversible even at low strain levels. For that purpose, the Rayleigh damping is introduced which can capture damping at small strains.

The damping matrix C is composed of the mass matrix M and the stiffness matrix K and given according to the Rayleigh damping formulation as:

$$\vec{C} = a_R \vec{M} + \beta_R \vec{K} \quad (5.15)$$

where a_R and β_R are the Rayleigh damping coefficients.

The Rayleigh damping coefficients can be calculated after the two target frequencies have been defined. According to (Hudson, 1994) the first target frequency is set equal to the fundamental frequency of the considered soil profile as:

$$f_1 = \frac{v_{s,average}}{4H} \quad (5.16)$$

where H is the thickness and $v_{s,average}$ is the average shear wave velocity of the considered soil layer.

The second target frequency is set as the closest odd number regarding the ratio of the fundamental frequency of the acceleration signal at bedrock to the first target frequency as:

$$f_2 \approx \frac{f_{fund}}{f_1} \quad (5.17)$$

where f_{fund} is the frequency with the maximum Fourier amplitude (Figure 5.2).

The Rayleigh damping coefficients a_R and β_R are then calculated as:

$$\alpha_R = \frac{2\xi\omega_1\omega_2}{\omega_1+\omega_2} \quad (5.18)$$

$$\beta_R = \frac{2\xi}{\omega_1+\omega_2} \quad (5.19)$$

where:

$$\omega_i = 2\pi f_i \quad (5.20)$$

where ξ is the target damping ratio and ω_i is the mode angular circular frequency.

In literature, the suggested values for damping ratio are varying between 0.5% and 2%. In this case, a value of 1% is used.

Soil column	$v_{s,average}$ (m/s)	H (m)	f_1 (Hz)	f_2 (Hz)	ω_1 (rad/s)	ω_2 (rad/s)	ξ (%)	α_R	β_R
D_R=60%	109	1	27,3	1	171,2	6,3	1	0,121215	0,00011
D_R=30%	129	10	3,2	1	20,3	6,3	1	0,095921	0,000753
D_R=40%	141	10	3,5	1	22,1	6,3	1	0,097893	0,000703
D_R=50%	153	10	3,8	1	24,0	6,3	1	0,099619	0,00066
D_R=60%	164	10	4,1	1	25,8	6,3	1	0,101024	0,000624
D_R=70%	229	15	3,8	1	24,0	6,3	1	0,099574	0,000661
D_R=80%	265	15	4,4	1	27,8	6,3	1	0,102464	0,000588

Table 5.6: Rayleigh damping coefficients by considering the elastic shear modulus G according to the PM4Sand model formulation.

Soil column	$v_{s,average}$ (m/s)	H (m)	f_1 (Hz)	f_2 (Hz)	ω_1 (rad/s)	ω_2 (rad/s)	ξ (%)	α_R	β_R
D_R=60%	137	1	34.3	1	215.2	6.3	1	0.122099	0.00009
D_R=30%	183	10	4.6	1	28.7	6.3	1	0.103123	0.000571
D_R=40%	190	10	4.8	1	29.8	6.3	1	0.103809	0.000554
D_R=50%	197	10	4.9	1	30.9	6.3	1	0.104455	0.000537
D_R=60%	203	10	5.1	1	31.9	6.3	1	0.104978	0.000524
D_R=70%	283	15	4.7	1	29.6	6.3	1	0.103682	0.000557
D_R=80%	328	15	5.5	1	34.3	6.3	1	0.106231	0.000492

Table 5.7: Rayleigh damping coefficients by considering the elastic shear modulus G according to the HSS Small model formulation.

The target frequencies f_1 and f_2 along with the corresponding Rayleigh damping coefficients α_R and β_R define frequencies that are going to be absorbed by the soil layers. This means that frequencies higher than f_1 are going to be over-damped. In that way, the frequency range between f_1 and f_2 is set automatically with lower damping values by Plaxis. This allows frequencies belonging to that range to be taken into account in the analysis. Using e.g higher values of f_1 results in a lower range of over-damped frequencies. This allows for more frequencies to be taken into account in the analysis and thus having a bigger influence in the results.

5.5 Dynamic Analysis

The dynamic analysis in Plaxis can be excecuted in two different ways: with consolidation or without consolidation. The latter is implemented in the latest version of Plaxis 2D 2018 and provides less mesh dependence and better spread of pore-water pressures according to the manual. In this study, both types of dynamic analysis are tested out and the differences in the results in terms of excess pore pressures evolution are investigated. Regarding the lateral boundaries, if free-field boundaries are to be used then the material at the boundaries needs to be replaced by drained layers. This is required to prevent complete loss of strength at the boundaries which may result in large deformations. In this case, the selected lateral boundary conditions are tied degrees of freedom as the hydraulic fill structure is simulated as a 1-D soil column. This allows to simulate a reduced geometry of the problem. The nodes at the left and right model boundaries are connected such that the nodes will undergo the same displacement At the bottom boundary a compliant base is applied by adding a surface to absorb downwards propagating waves.

The geometry of the simulated hydraulic fill and of the whole soil column is depicted in Figure 5.2.
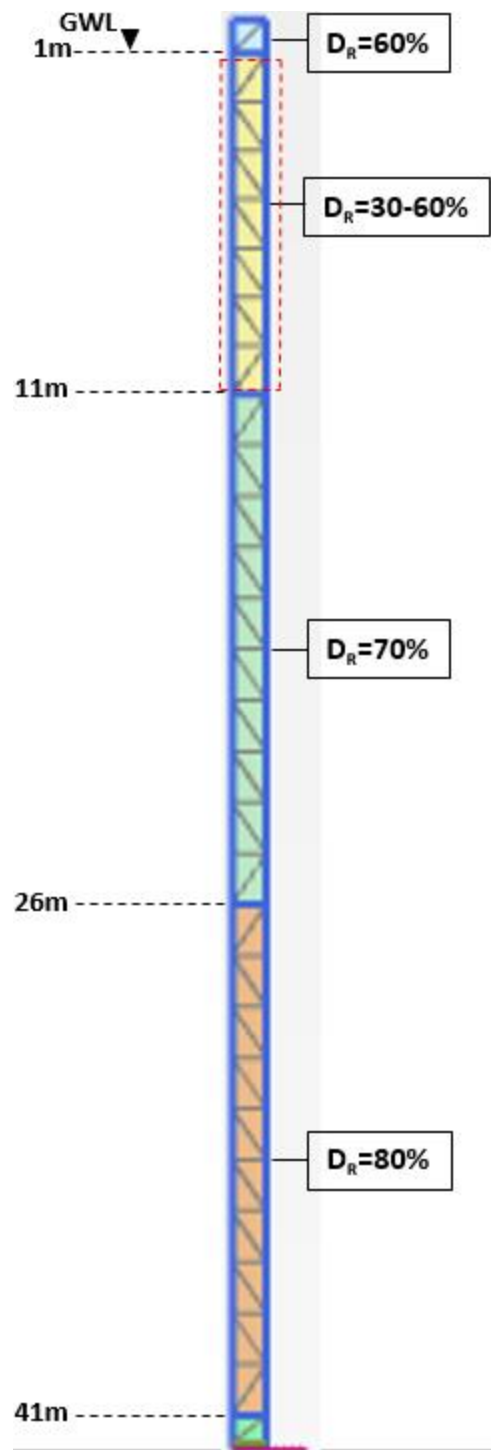
Figure 5.2: Model geometry. Hydraulic fill simulated as a 1-D soil column.

5.6 Results

This section includes the results obtained from Plaxis regarding the generation of excess pore pressures in the hydraulic fill layers with relative densities of $D_R = 30\%$, $D_R = 40\%$, $D_R = 50\%$ and $D_R = 60\%$ for all seven different earthquake motions (Appendix A.1). In real practise, it is suggested to scale the series of acceleration signals into a specific value of peak

ground acceleration. In this thesis project, this is not carried out as the resulting excess pore pressures evolution in the end of the earthquake motion (and thus the earthquake-induced liquefaction) is not influenced by the peak ground acceleration. Firstly, dynamic analyses without consolidation are performed for all the aforementioned fill cases followed by dynamic analyses with consolidation. The differences in the results in terms of excess pore pressures evolution are investigated for both types of analysis. Soil layers that reach an excess pore pressure ratio (r_u) of around 1.0 are identified as liquefied.

5.6.1 Sensitivity analysis

Mesh element size

Initially, the dynamic analyses in Plaxis are performed with a very coarse mesh. A domain comprised of coarse mesh elements is suggested to be employed in order to save computational time. However, this triggered the question on whether finer mesh elements would result in different results. Consequently, the influence of the mesh element size in the generation of excess pore pressures is investigated by refining the domain. Two finer element sizes are tested for the analyses: an element size of $0.90m$ and $0.46m$ compared to the initial analyses where the element size was $1.45m$. It is observed, that when using finer mesh elements the results remain the same in terms of excess pore pressures generation. This can be attributed to the fact, that the default element size of $1.45m$ is within the range of allowable limits regarding the maximum value (Table 5.5) that leads to a proper wave propagation along the soil column.

Time step

The dynamic time step in Plaxis is set equal to the time step of the acceleration input signal. This is set in the dynamic phase where the time step is set as the dynamic time interval $(100s)$ divided by the maximum number of steps stored in the software. In order to save computational time, the user can reduce the maximum number of substeps while increasing the number of substeps, as long as the aforementioned division is even to the dynamic time step $(0.01s)$ (eq. 5.18).

$$Time\ step = \frac{Dynamic\ time\ interval}{Max\ no.steps * Substeps} \quad (5.18)$$

Target frequency

As described in Chapter 5.4.4, the target frequencies are defined through the elastic shear modulus G in two different ways: i) according to the formula for HSS Small model and ii) according to the formula for PM4Sand model. These are giving different values for the target 9frequency f_1. By applying (i) for the calculation of target frequencies leads to slightly higher values of f_1 and consequently to a lower range of over-damped frequencies. This allows for more frequencies to be taken into account in the analysis and one should expect bigger influence in the results. For that reason, both ways are tested and the differences in terms of excess pore pressure evolution are examined. It is observed, that the range between the two

target frequencies has a minor effect in the generation of excess pore pressures for all different hydraulic fills. On the other hand, the influence of the range between the target frequencies is more explicit in the resulting displacements. In particular, a bigger range leads to slightly higher horizontal displacements along the fill column.

Final set of parameters

Mesh element size	Time step	Dynamic time interval	Max no. steps	Substeps	Target frequency f_1	Target frequency f_2 (Hz)
(m)	(s)	(s)	(-)	(-)	(Hz)	(Hz)
1.45	0.01	100	2000	5	3.2	1

Table 5.8: Final set of parameters that are used in the dynamic analysis.

5.6.2 Dynamic Analysis without Consolidation

Excess Pore Pressures Generation

Dr=30%

i) After $24s$ excess pore pressures start to develop in the hydraulic fill layer (Figure 5.3). Between $24s$ and $32s$ an increase in excess pore pressure is identified mainly in the middle hydraulic fill layer that propagates upwards and downwards through the soil column. After a rapid increase in excess pore pressures at $35s$ the liquefaction condition is reached ($r_u \approx 1$) at $38s$. This condition is extended nearly throughout the entire fill layer. The liquefaction condition that has been reached up to that point remains constant and restraint in the parts of the hydraulic fill that have liquefied and it does not propagate further through the soil column until the end of the earthquake signal ($100s$).
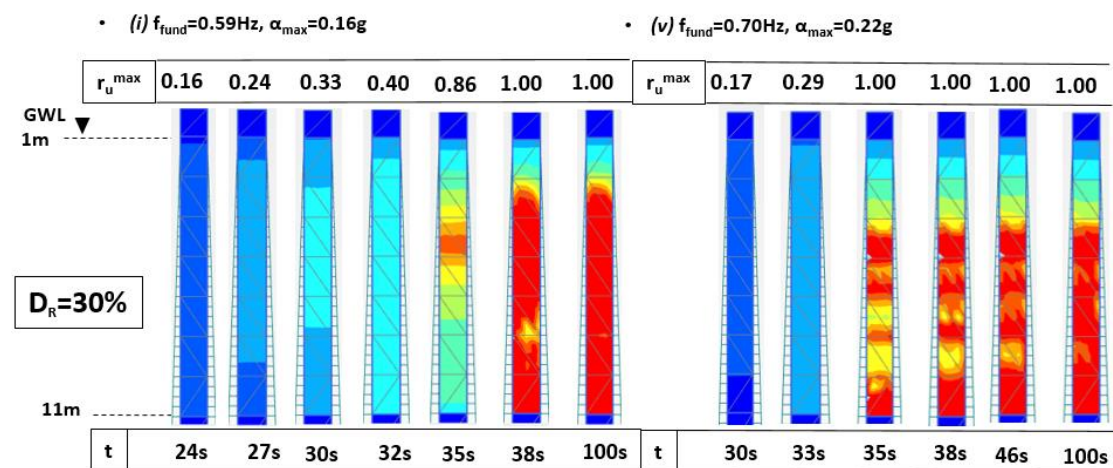
Figure 5.3: Excess pore pressure ratio development in the hydraulic fill of $D_R = 30\%$ for dynamic analysis without consolidation: (i, v)

v) After $30s$ excess pore pressures start to develop in the hydraulic fill layer (Figure 5.3). Between $30s$ and $33s$ a slight increase in excess pore pressure is identified in the hydraulic fill layer and at $35s$ the liquefaction condition is reached ($r_u \approx 1$) in scattered zones along the

fill layer. Between $35s$ and $46s$ the liquefaction state is spread in between these zones by creating a uniform liquefied layer. The liquefaction condition that has been reached up to that point remains constant and restraint in the parts of the hydraulic fill that have liquefied and it does not propagate further through the soil column until the end of the earthquake signal ($100s$).

The results regarding the remaining acceleration signals (ii, iii, iv, vi, vii) and the corresponding evolution of excess pore pressures along the hydraulic fill are indicated in Figure 5.4. It is observed, that the liquefied parts are localized in discrete zones within the hydraulic fill and are not extending along the entire fill column.

Figure 5.4: Excess pore pressure ratio development in the hydraulic fill of $D_R = 30\%$ for dynamic analysis without consolidation (ii, iii, iv, vi, vii)

Dr=40%

i) After $24s$ excess pore pressures start to develop in the hydraulic fill layer (Figure 5.5). Between 24 and $35s$ an increase in excess pore pressure is identified mainly in the middle hydraulic fill layer that propagates upwards and downwards through the soil column. After a rapid increase in excess pore pressure at $38s$ the liquefaction condition is reached ($r_u \approx 1$) which extends from bottom to mid-upper part of the fill and at $43s$ the liquefaction state is propagated gently upwards. The liquefaction condition that has been reached up to that point remains constant and restraint in the parts of the hydraulic fill that have liquefied and it does not propagate further through the soil column until the end of the earthquake signal ($100s$).

ii) After $32s$ excess pore pressures start to develop in the hydraulic fill layer (Figure 5.5). Between $32s$ and $43s$ an increase in excess pore pressure is identified mainly in the middle

hydraulic fill layer that propagates upwards and downwards through the soil column. After a rapid increase in excess pore pressure at $49s$ the liquefaction condition is reached ($r_u \approx 1$) in the mid-upper part of the fill. Between $49s$ and $57s$ the liquefaction state is extended from top to nearly the bottom fill by creating a uniform liquefied layer.

Figure 5.5: Excess pore pressure ratio development in the hydraulic fill of $D_R = 40\%$ for dynamic analysis without consolidation.

iv) After $35s$ excess pore pressures start to develop in the hydraulic fill layer (Figure 5.5). Between $35s$ and $41s$ an increase in excess pore pressure is identified mainly in the mid-upper hydraulic fill layer that propagates upwards and downwards through the soil column. After a rapid increase in excess pore pressure at $43s$ the liquefaction condition is reached ($r_u \approx 1$) in the mid-upper layer. Between $43s$ and $51s$ a significant rise in the excess pore pressures is observed likewise in the mid-lower fill layer and at $54s$ this part has also liquefied ($r_u \approx 1$). Between $54s$ and $57s$ the liquefaction state is propagated between the two aforementioned liquefied layers and eventually almost the entire hydraulic fill has liquefied.

v) After $30s$ excess pore pressures start to develop in the hydraulic fill layer (Figure 5.5). Between $30s$ and $32s$ a slight increase in excess pore pressures is identified that propagates upwards and downwards through the soil column. After a rapid increase in excess pore

pressures at $35s$ the liquefaction condition is reached ($r_u \approx 1$) which extends from bottom to mid-upper part of the fill and at $38s$ the liquefaction state is propagated gently upwards.

The results regarding the remaining acceleration signals (iii, vi, vii) and the corresponding evolution of excess pore pressures along the hydraulic fill are indicated in Figure 5.6. It is observed, that, the liquefied parts are restricted in distinct zones within the hydraulic fill and are not extending along the entire fill column.

- (iii) f_{fund}=3.31Hz, α_{max}=0.20g
- (vi) f_{fund}=5.47Hz, α_{max}=0.22g
- (vii) f_{fund}=3.6Hz, α_{max}=0.14g

$r_u{}^{max}$	0.26	0.36	0.47	1.00	1.00	1.00
$r_u{}^{max}$	0.22	0.29	0.31	0.89	1.00	1.00
$r_u{}^{max}$	0.19	0.26	0.28	1.00	1.00

| t | 22s | 24s | 27s | 35s | 38s | 100s |
| t | 24s | 27s | 33s | 35s | 38s | 100s |
| t | 24s | 27s | 30s | 33s | 100s |

Figure 5.6: Excess pore pressure ratio development in the hydraulic fill of $D_R = 40\%$ for dynamic analysis without consolidation

At this point, it important to highlight, that the excess pore pressures evolution along the hydraulic fill and eventually the liquefaction triggering is dependent on the dominant frequency of the considered signal regardless the peak ground acceleration values. In particular, there is a better diffusion of excess pore pressures in the loosely-packed fills ($D_R = 30\%$ and $D_R = 40\%$) for the signals of low dominant frequencies (Figure 5.3, 5.5). However, for the rest of the signals, there is a localization of liquefied zones in distinct parts along the fill (Figure 5.4, 5.6).

Dr=50%

iii) After $22s$ excess pore pressures start to develop in the hydraulic fill layer (Figure 5.7). Between $22s$ and $30s$ an increase in excess pore pressures is identified mainly in the middle hydraulic fill layer that propagates upwards and downwards through the soil column. Between $32s$ and $38s$ a rapid increase in excess pore pressure is observed in three distinct zones of the fill layer which have eventually liquefied ($r_u \approx 1$). Between $38s$ and $41s$ the liquefaction state is spreaded in between those zones forming almost an entire liquefied layer extending from bottom to mid-upper fill part.

vi) After $22s$ excess pore pressures start to develop in the hydraulic fill layer (Figure 5.7). Between $22s$ and $30s$ an increase in excess pore pressure is identified in the mid-upper hydraulic fill layer that propagates upwards and downwards through the soil column. Between $32s$ and $35s$ a rapid increase in excess pore pressures is observed in three distinct zones of the fill layer which eventually have liquefied ($r_u \approx 1$). Between $35s$ and $38s$ the liquefaction state is spreaded in between those zones forming a uniform liquefied layer

extending from bottom to mid-upper fill part and at $41s$ the liquefaction state is slightly propagated upwards.

vii) After $24s$ excess pore pressures start to develop in the hydraulic fill layer (Figure 5.7). Between $24s$ and $30s$ a slight increase in excess pore pressure is identified in the mid-upper hydraulic fill layer that propagates upwards and downwards through the soil column. After a rapid increase in excess pore pressures at $32s$ the liquefaction condition is reached ($r_u \approx 1$) which extends from bottom to mid-upper part of the fill and at $38s$ the liquefaction state is propagatedgently upwards.
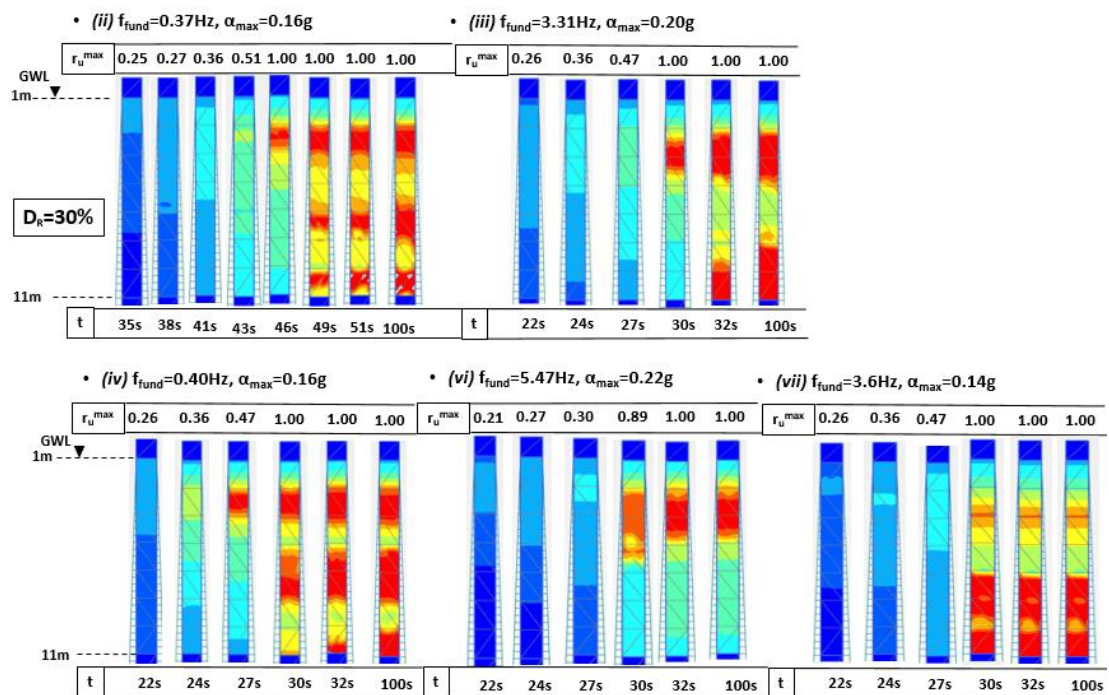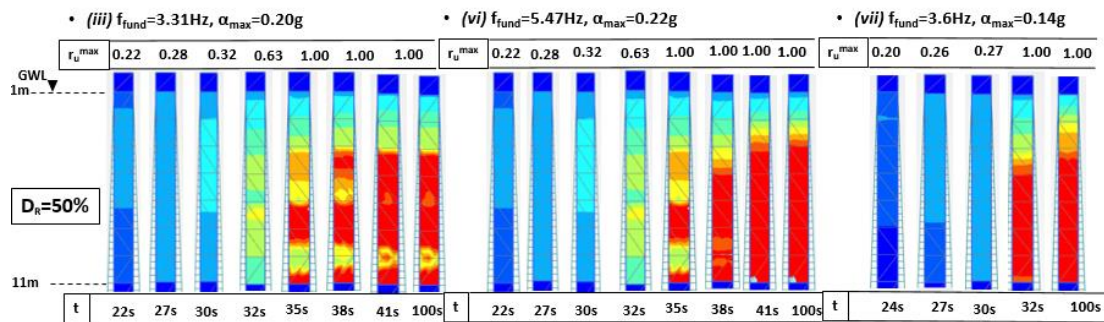

Figure 5.7: Excess pore pressure ratio development in the hydraulic fill of $D_R = 50\%$ for dynamic analysis without consolidation

The results regarding the remaining acceleration signals (i, ii, iv, v) and the corresponding evolution of excess pore pressures along the hydraulic fill are indicated in Figure 5.8. The liquefied parts are localized in a singular restricted zone within the fill layer which is not the case in the fills of lower densities ($D_R = 30\%$, $D_R = 40\%$) in which the liquefied parts are developing in more discrete zones and in a less restricted manner. Therefore, the effect of the relative density as an input parameter has a significant role in the liquefaction triggering.
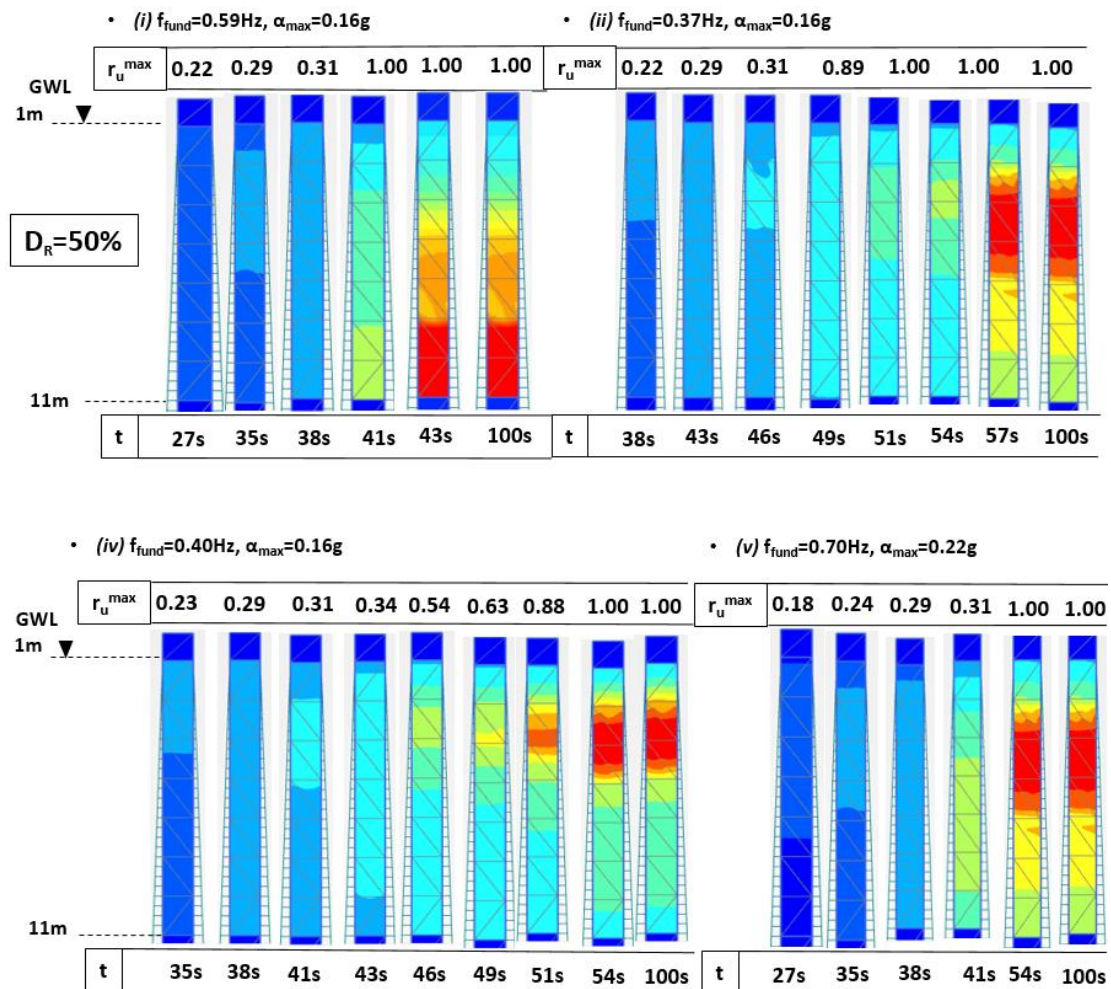
Figure 5.8: Excess pore pressure ratio development in the hydraulic fill of $D_R = 50\%$ for dynamic analysis without consolidation

Dr=60%

iii) After $22s$ excess pore pressures start to develop in the hydraulic fill layer (Figure 5.9). Between $22s$ and $32s$ an increase in excess pore pressure is identified that propagates upwards and downwards through the soil column. Between $32s$ and $38s$ a rapid increase in excess pore pressure is observed in two distinct parts of the fill which have eventually liquefied ($r_u \approx 1$). Between $38s$ and $43s$ the liquefaction state is spreaded in between those parts forming an entire liquefied layer extending from bottom to mid-upper fill.
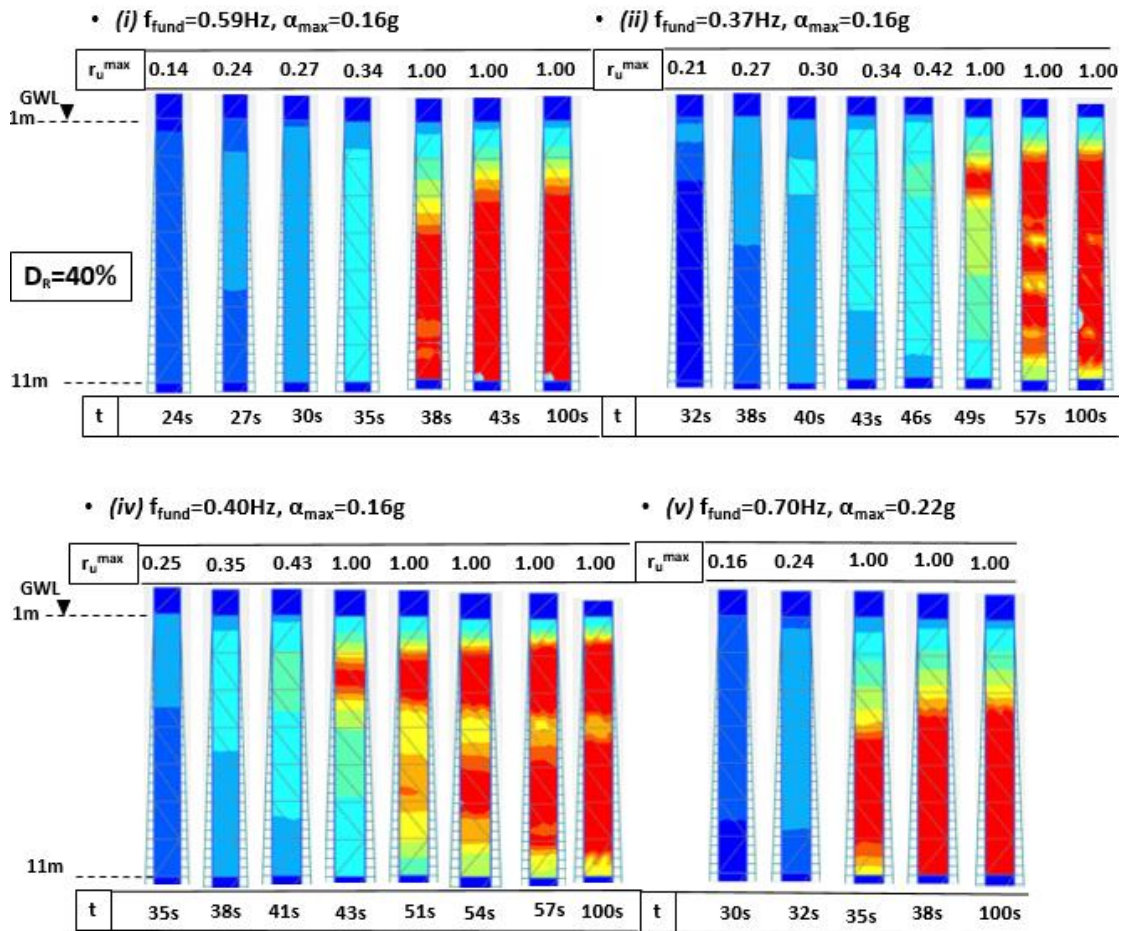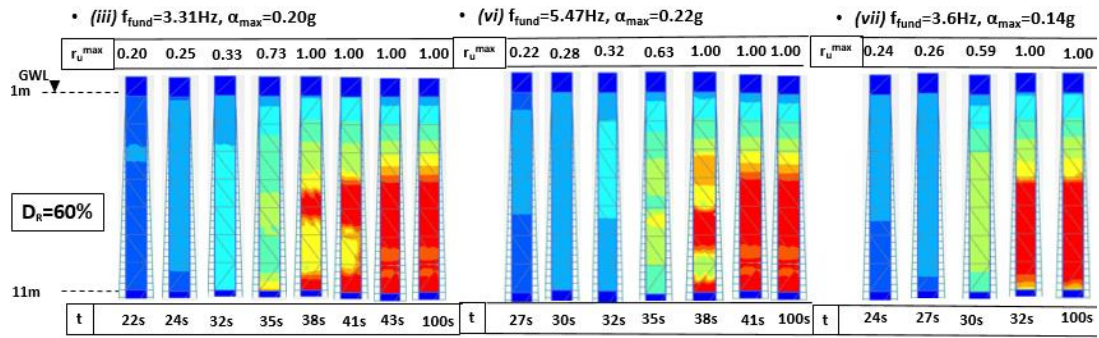
Figure 5.9: Excess pore pressure ratio development in the hydraulic fill of $D_R = 60\%$ for dynamic analysis without consolidation.

vi) After $27s$ excess pore pressures start to develop in the hydraulic fill layer (Figure 5.9). Between $27s$ and $32s$ an increase in excess pore pressures is identified mainly in the middle hydraulic fill layer that propagates upwards and downwards through the soil column. Between $35s$ and $38s$ a rapid increase in excess pore pressure is observed in three distinct zones of the fill layer which have eventually liquefied ($r_u \approx 1$). Between $38s$ and $41s$ the liquefaction state is spreaded in between those zones forming an entire liquefied layer extending from bottom to mid-upper fill part.

vii) After $24s$ excess pore pressures start to develop in the hydraulic fill layer (Figure 5.9). Between $24s$ and $30s$ an increase in excess pore pressures is identified mainly in the middle hydraulic fill layer that propagates upwards and downwards through the soil column. After a rapid increase in excess pore pressures at $32s$ the liquefaction condition is reached ($r_u \approx 1$) which extends from bottom to middle part of the fill.

Regarding the aforementioned results, the liquefaction condition in the end of the earthquake is more restricted compared to the fills of lower relative densities ($D_R = 30\%$, $D_R = 40\%$) in which the liquefied parts are extending almost along the entire fill column (Figure 5.3, 5.5). Consequently, the relative density as an input parameter has a significant role in the liquefaction triggering.

The results regarding the remaining acceleration signals (i, ii, iv, v) and the corresponding evolution of excess pore pressures along the hydraulic fill are indicated in Figure 5.10. It is observed, that the liquefied parts are localized in a singular restricted zone within the fill layer regarding two signals (i, v) while for the rest (ii, iv), the liquefaction is not triggered at all. This can be attributed to the fact, that the relative density is significant in the evolution of excess pore pressures and eventually in the liquefaction triggering.
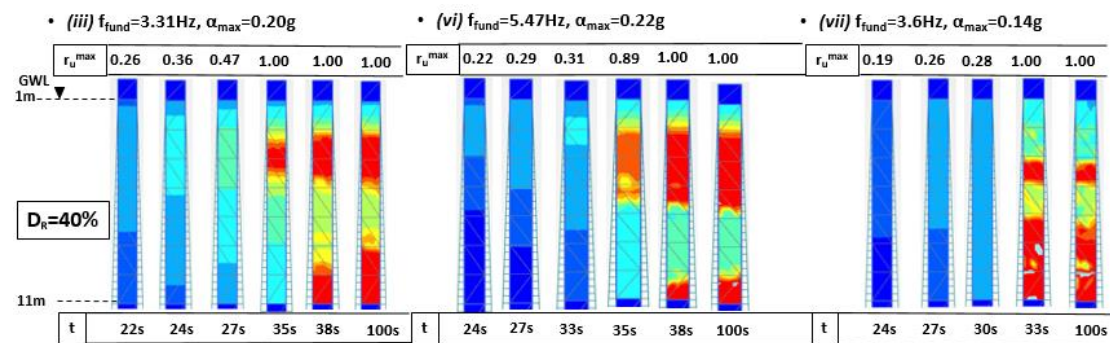
Figure 5.10: Excess pore pressure ratio development in the hydraulic fill of $D_R = 60\%$ for dynamic analysis without consolidation

At this point, it is important to note, that there is a better diffusion of excess pore pressures in the densely-packed fills ($D_R = 50\%$ and $D_R = 60\%$) for the signals of high dominant frequencies (Figure 5.7, 5.9). This phenomenon is contrary to the one observed in the loosely-packed fills ($D_R = 30\%$ and $D_R = 40\%$), in which there is a better excess pore pressure diffusion for the low dominant frequency signals. However, there is a localization of a singular liquefied zone within the fill for the rest of the signals (Figure 5.8, 5.10).

5.6.3 Dynamic Analysis with Consolidation

The new version of Plaxis 2D 2018 is incorporating the mode of dynamic analysis with consolidation. This type of analysis provides less mesh dependence and better spread of pore-water pressures according to the Plaxis manual. Moreover, in the current mode, the coefficients of permeability need to be introuced to the software. Depending on the magnitude of these coefficients, the rate of excess pore pressures dissipation is defined. In particular, for higher values of the coefficient of permeability, the excess pore pressures are dissipating faster as the flow rate for drainage is higher.

Due to the lack of experimental data (e.g grain size distribution curves) from which to determine those coefficients, empirical values are adopted (Table 5.8) which are taking into account a wide range of soils with different permeabilites. The coefficients of permeability for the hydraulic fills placed over relative densities of $D_R = 30\%, D_R = 40\%, D_R = 50\%$ and $D_R = 60\%$ can be considered to vary between the values from low permeable to medium permeable soils. Therefore, the coefficients of permeability are considered to range between the values of $10^{-6}, 10^{-5}, 10^{-4}, 10^{-3}\ m/s$.

In the following section, a sensitivity analysis regarding the influence of the aforementioned coefficients in the generation of excess pore pressures is carried out for all different hydraulic fills and the differences in the results with respect to the dynamic analysis without consolidation are investigated. In the dynamic analyses with consolidation, one representative acceleration motion is depicted for each relative density which is followed by the corresponding dynamic analysis without consolidation for the same signal. This is done, in order to explain the main differences between the two different types of analysis. The results for the other representative acceleration signals are indicated in Appendix A.3.

Typical Coefficient of Permeability k Values for Different Soils

Relative Permeability	Coefficient of Permeability, k (cm/s)	Typical Soils
Very permeable	$>1 \times 10^{-1}$	Coarse gravel
Medium permeable	$1 \times 10^{-1} - 1 \times 10^{-3}$	Sand, fine sand
Low permeable	$1 \times 10^{-3} - 1 \times 10^{-5}$	Silty sand, dirty sand
Very low permeable	$1 \times 10^{-5} - 1 \times 10^{-7}$	Silt, fine sandstone
Impervious	$<1 \times 10^{-7}$	Clay

Table 5.8: Typical coefficients of permeability for different soils

Excess Pore Pressures Generation

Dr=30%

- ***(ii)*** $f_{fund} = 0.37Hz, \alpha max = 0.16g$

k=10⁻⁶m/s

After $35s$ excess pore pressures start to develop in the hydraulic fill layer (Figure 5.11). Between $35s$ and $43s$ an increase in excess pore pressure is identified mainly in the mid-upper hydraulic fill layer that propagates upwards and downwards through the soil column. After a rapid increase in excess pore pressures at $46s$ the liquefaction condition $(r_u \approx 1)$ is reached in the mid-upper fill part. Between $46s$ and $54s$ the liquefaction state is reached in two more discrete zones along the fill column. Moreover, between $54s$ until the end of the earthquake $(100s)$ a slight increase in excess pore pressures is observed in between the liquefied parts. This is can be attributed to the fact, that with $k = 10^{-6} \, m/s$, the developed excess pore pressures tend to dissipate upwards and downwards along the soil column in between the liquefied layers. Hence, the liquefaction condition $(r_u \approx 1)$ is better spread along the fill layer. However, the magnitude of the current permeability coefficient is very low. Therefore, there is not enough time for enough drainage and for a more extensive diffusion of the liquefaction state throughout the fill layer. As a result, some parts of the fill layer did not liquefy at the end of the earthquake $(100s)$. It is important to note, the current dynamic analysis with consolidation, for this extremely low value of permeability coefficient $(10^{-6} \, m/s)$, nearly resembles to the undrained response for the corresponding dynamic analysis without consolidation (Figure 5.12).

k=10⁻⁵m/s

Between $35s$ and $43s$ the generation of excess pore pressures is almost identical compared to the analysis with $k = 10^{-6}m/s$ (Figure 5.11). However, the impact of the permeability coefficient has a crucial role after this point. In particular, the liquefaction state is better spread along the fill column between $46s$ until the end of the earthquake $(100s)$. Cosequently, by applying a permeability coefficient of higher magnitude, the dissipation of excess pore pressures that have developed in the liquefied layers is accomplished in a faster rate. Hence, the liquefaction condition $(r_u \approx 1)$ is more uniformly diffused throughout the fill layer. As a result, at the end of the ground motion the entire fill has liquefied after $r_u \approx 1$ is reached.

- *(ii)* $f_{fund}=0.37Hz$, $\alpha_{max}=0.16g$
- $k=10^{-6}m/s$

$r_u{}^{max}$	0.25	0.27	0.36	0.51	1.00	1.00	1.00	1.00	1.00

GWL
1m

$D_R=30\%$

11m

t	35s	38s	41s	43s	46s	49s	54s	62s	100s

- $k=10^{-5}m/s$

$r_u{}^{max}$	0.29	0.33	0.37	0.49	1.00	1.00	1.00	1.00	1.00

t	35s	38s	41s	43s	46s	49s	54s	62s	100s

- $k=10^{-4}m/s$

$r_u{}^{max}$	0.32	0.40	0.53	0.75	1.00	1.00	1.00	1.00	1.00

GWL
1m

$D_R=30\%$

11m

t	35s	38s	41s	43s	46s	49s	51s	57s	100s

- $k=10^{-3}m/s$

$r_u{}^{max}$	0.22	0.38	0.55	0.82	1.00	1.00	1.00	1.00	1.00

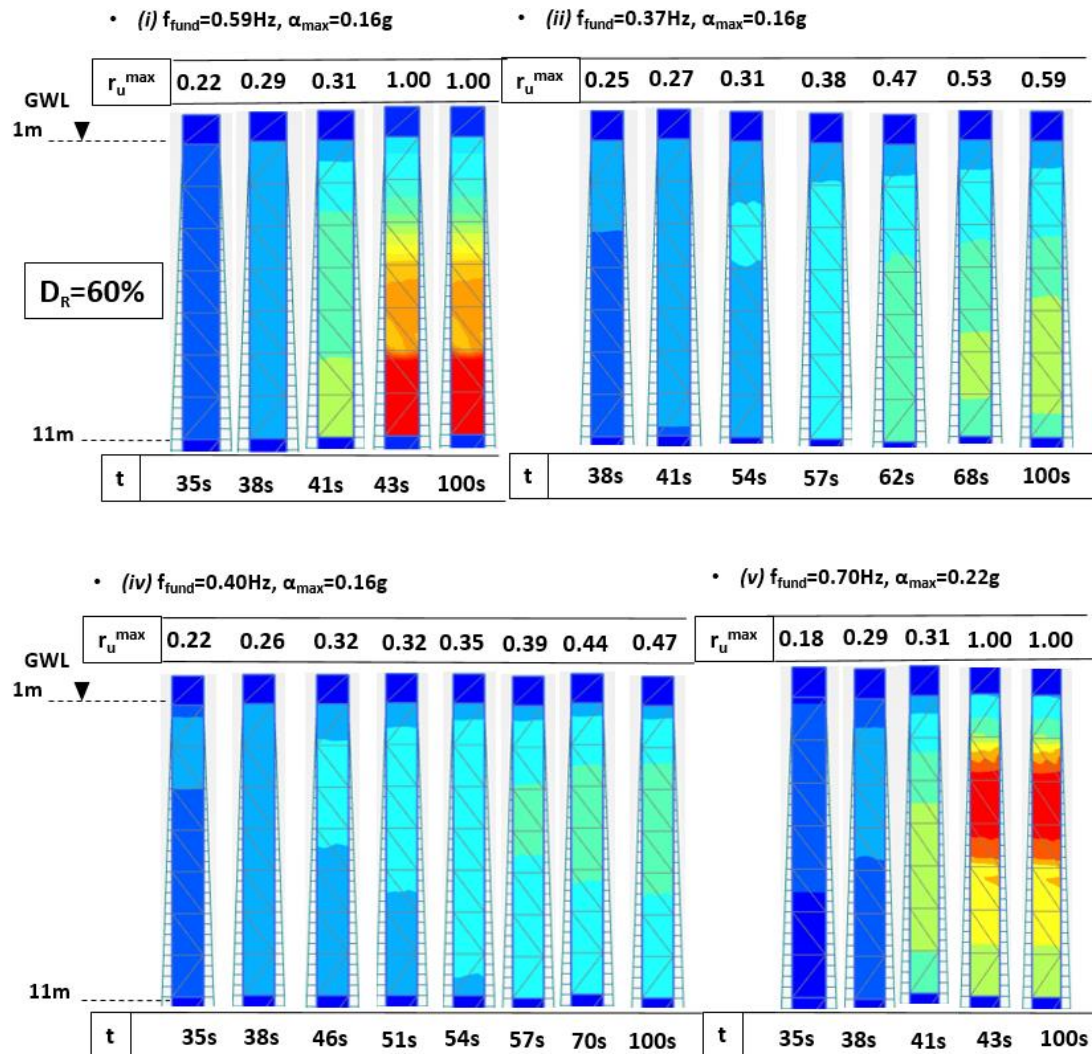| t	35s	38s	41s	43s	46s	49s	51s	57s	100s

Figure 5.11: Excess pore pressure ratio development in the hydraulic fill of $D_R = 30\%$ for dynamic analysis with consolidation.

$k=10^{-4}m/s$ & $k=10^{-3}m/s$

Between $35s$ and $43s$ the rate of excess pore pressures generation is increased compared to the analyses with $k = 10^{-6}m/s$ and $k = 10^{-5}m/s$ (Figure 5.11). This increase originates from the top fill part and propagates downwards through the soil column. At $46s$ the liquefaction condition ($r_u \approx 1$) is reached in the top fill part. Moreover, between $46s$ and $57s$, the liquefaction state is uniformly propagated from top to bottom fill part without forming discrete or scattered zones throughout. Similarly, by applying a permeability coefficient of an even higher magnitude ($k = 10^{-4}m/s$ & $k = 10^{-3}m/s$), the excess pore pressures developed in the liquefied layers are dissipating more rapidly with respect to the ones of lower magnitudes ($k = 10^{-6}m/s$ & $k = 10^{-5}m/s$). Hence, the liquefaction condition ($r_u \approx 1$) is even more uniformly diffused through the fill layer. As a result, at $57s$ the entire fill has liquefied. It is important to note, that the liquefaction phenomenon capturing the entire fill is occuring much earlier compared to the $k = 10^{-5}m/s$ case in which the fill column has liquefied in the end of the earthquake ($100s$).

Figure 5.12: Excess pore pressure ratio development in the hydraulic fill of $D_R = 30\%$ for dynamic analysis without consolidation

Dr=40%

- **(vi)** $f_{fund} = 5.47Hz, \alpha max = 0.22g$

k=10⁻⁶m/s

Between $11s$ and $16s$ an increase in excess pore pressures is identified mainly in the upper hydraulic fill layer that propagates downwards through the soil column (Figure 5.13). After a rapid increase in excess pore pressures at $19s$ the liquefaction condition ($r_u \approx 1$) is reached in both the mid-upper and bottom fill part. Between $19s$ until the end of the earthquake ($100s$) a slight increase in excess pore pressures mainly in the top fill part. Similarly as described before, the current dynamic analysis with consolidation, for an extremely low value of permeability coefficient ($10^{-6}\ m/s$), nearly resembles the undrained response for the corresponding dynamic analysis without consolidation (Figure 5.14).

k=10⁻⁵m/s

Between $11s$ and $16s$ the generation of excess pore pressures is very similar compared to the analysis with $k = 10^{-6}m/s$ (Figure 5.13). However, the impact of the permeability coefficient has a crucial role after this point. In particular, the liquefaction state is better diffused along the fill column between $19s$ and $57s$ in which the entire fill has liquefied. The liquefaction phenomenon is capturing the entire fill layer much earlier ($57s$) compared to the $k = 10^{-6}m/s$ case in which the entire fill has not liquefied even at the end of the earthquake ($100s$).

- $k=10^{-6}$m/s   - $k=10^{-5}$m/s

| r_u^{max} | 0.30 | 0.31 | 0.85 | 1.00 | 1.00 | 1.00 | 1.00 | r_u^{max} | 0.39 | 0.42 | 0.87 | 1.00 | 1.00 | 1.00 | 1.00 | 1.00 | 1.00 |

| t | 11s | 14s | 16s | 19s | 41s | 78s | 100s | t | 11s | 14s | 16s | 19s | 24s | 30s | 35s | 57s | 100s |

- $k=10^{-4}$m/s   - $k=10^{-3}$m/s

| r_u^{max} | 0.52 | 0.55 | 0.89 | 1.00 | 1.00 | 1.00 | 1.00 | r_u^{max} | 0.64 | 0.70 | 1.00 | 1.00 | 1.00 | 1.00 | 1.00 |

| t | 11s | 14s | 16s | 19s | 22s | 24s | 100s | t | 11s | 14s | 16s | 19s | 22s | 24s | 100s |

Figure 5.13: Excess pore pressure ratio development in the hydraulic fill of $D_R = 40\%$ for dynamic analysis with consolidation.

$k=10^{-4}$m/s

Between $11s$ and $16s$ the rate of excess pore pressures generation is increased compared to the analyses with $k = 10^{-6}m/s$ and $k = 10^{-5}m/s$ (Figure 5.13). This increase originates from the top fill part and propagates downwards through the soil column. As described before, by applying a permeability coefficient of an even higher magnitude ($k = 10^{-4}m/s$), the drainage flow rate is higher with respect to the ones of lower magnitudes ($k = 10^{-6}m/s$ & $k = 10^{-5}m/s$). Hence, the liquefaction condition ($r_u \approx 1$) is even more uniformly diffused through the fill layer. As a result, at $24s$ the entire fill has liquefied. It is important to note, that the liquefaction phenomenon is occuring much earlier compared to the $k = 10^{-5}m/s$ case in which the entire fill had liquefied at $57s$.

$k=10^{-3}$m/s

Between $11s$ and $14s$ the rate of excess pore pressures generation is increased compared to the analyses with $k = 10^{-6}m/s$, $k = 10^{-5}m/s$ and $k = 10^{-4}m/s$ (Figure 5.9). This increase originates from the top fill part and propagates downwards through the soil column. At $16s$ the liquefaction condition ($r_u \approx 1$) is reached in the top fill part. Moreover, between $16s$ and $24s$, the liquefaction state is even more uniformly propagated along the entire fill part

without forming discrete or scattered zones throughout and at $24s$ the entire hydraulic fill has liquefied.

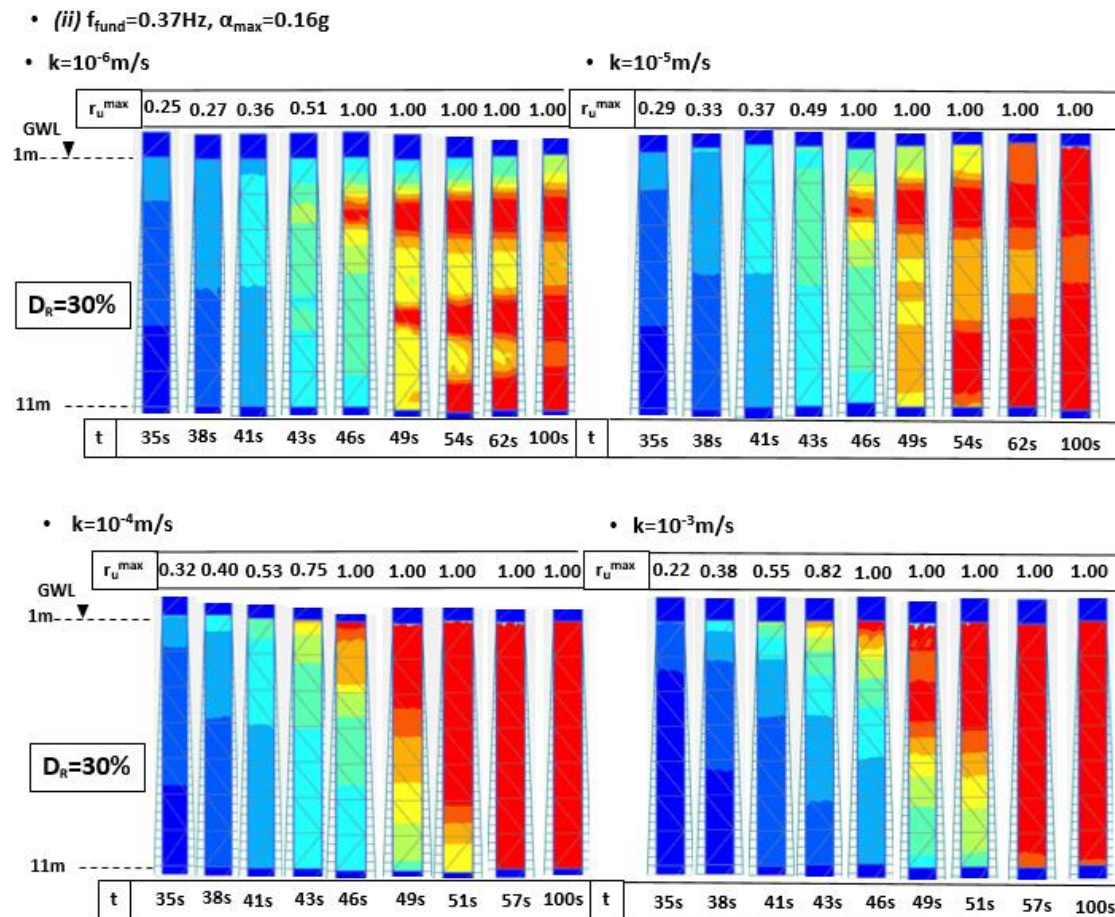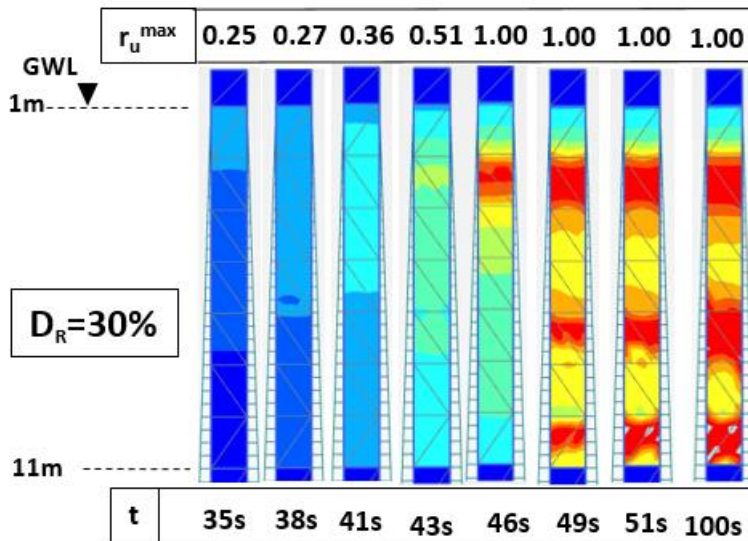
Figure 5.14: Excess pore pressure ratio development in the hydraulic fill of $D_R = 40\%$ for dynamic analysis without consolidation

Dr=50%

- *(ii)* $f_{fund} = 0.37Hz, \alpha max = 0.16g$

k=10⁻⁶m/s

Between $35s$ and $54s$ an increase in excess pore pressures is identified mainly in the mid-upper hydraulic fill layer that propagates upwards and downwards through the soil column (Figure 5.15). It is important to note, that the excess pore pressure generation is carried out in a considerably slower rate than in the loosely-packed fills ($D_R = 30\%, D_R = 40\%$). Thus, the apparent relative density D_R, as an input parameter, has a crucial role in the generation of excess pore pressure and hence in the liquefaction triggering of the fill. After a rapid increase in excess pore pressures at $57s$ the liquefaction condition ($r_u \approx 1$) is reached in the middle fill part. Between $57s$ until the end of the earthquake ($100s$) a slight increase in excess pore pressures is observed around the aforementioned liquefied layers. As described before, the excess pore pressures developed in the liquefied layers tend to dissipate upwards and downwards along the soil column and hence, spread the liquefaction condition ($r_u \approx 1$) throughout the fill column. However, the magnitude of the permeability coefficient is very low ($k = 10^{-6} \, m/s$). Therefore, there is not enough time for drainage and for a more extensive diffusion of the liquefaction state throughout the fill layer. As a result, at the end of the earthquake ($100s$) the liquefaction is restricted in a singular continuous layer. Similarly, the current dynamic analysis with consolidation, for an extremely low value of permeability coefficient ($10^{-6} \, m/s$), nearly resembles the undrained response for the corresponding dynamic analysis without consolidation (Figure 5.16).

k=10⁻⁵m/s

Between $35s$ and $51s$ the generation of excess pore pressures is very similar compared to the analysis with $k = 10^{-6}m/s$ (Figure 5.15). However, the impact of the permeability coefficient has a crucial role after this point. In particular, once the liquefaction state is reached in the middle fill part ($57s$) this condition is better diffused towards the top of the fill column and gently downwards between $57s$ and until $89s$. Consequently a permeability coefficient of higher magnitude leads to a higher drainage flow rate and thus a faster dissipation of excess pore pressures that are developed in the liquefied layers. As a result, the liquefaction condition ($r_u \approx 1$) is more uniformly diffused throughout the fill layer. At $89s$ a continuous liquefied layer has been formed extending from top to mid-lower fill column. An important observation at this point is, that at the end of the ground motion ($100s$) the entire fill has not liquefied which was actually the case in the corresponding loosely-packed fills ($D_R = 30\%, D_R = 40\%$). This is attributed to the fact, that the higher relative density of the fill ($D_R = 50\%$) restricts the generation of excess pore pressures and therefore, the spread of the liquefaction condition to a smaller extent compared to the loosly-packed fills ($D_R = 30\%, D_R = 40\%$).

- *(ii) f_fund=0.37Hz, α_max=0.16g*
- k=10⁻⁶m/s
- k=10⁻⁵m/s

r_u^{max}	0.25	0.27	0.31	0.39	0.47	0.52	1.00	1.00	1.00
t	35s	38s	46s	49s	51s	54s	57s	59s	100s

r_u^{max}	0.30	0.36	0.46	0.51	1.00	1.00	1.00	1.00	1.00
t	35s	41s	49s	51s	57s	59s	78s	89s	100s

- k=10⁻⁴m/s
- k=10⁻³m/s

r_u^{max}	0.33	0.51	0.68	1.00	1.00	1.00	1.00	1.00
t	35s	41s	46s	51s	57s	60s	68s	100s

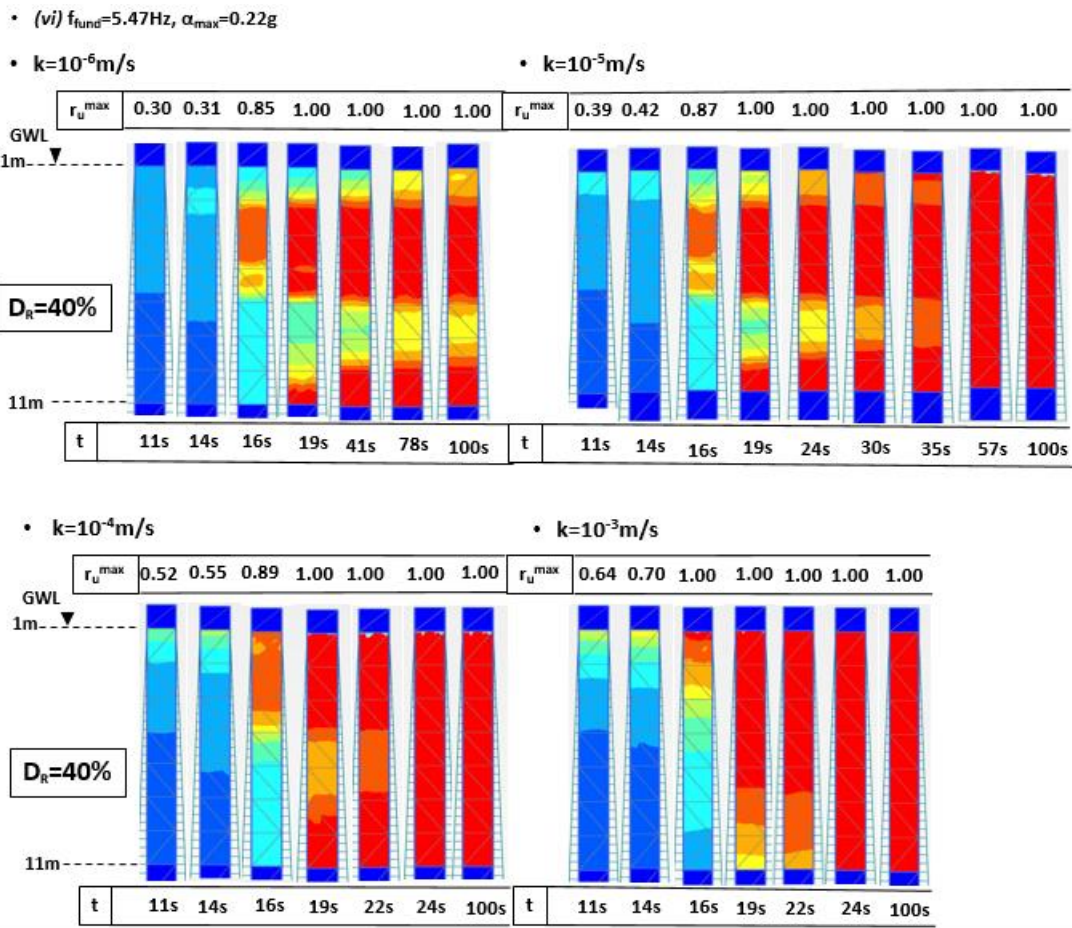| r_u^{max}	0.41	0.57	0.75	0.84	1.00	1.00
t	35s	38s	41s	43s	49s	57s	100s

Figure 5.15: Excess pore pressure ratio development in the hydraulic fill of $D_R = 50\%$ for dynamic analysis with consolidation.

k=10⁻⁴m/s

Between $35s$ and $46s$ the rate of excess pore pressures generation is increased compared to the analyses with $k = 10^{-6}m/s$ and $k = 10^{-5}m/s$ (Figure 5.15). This increase originates from the top fill part and propagates downwards through the soil column. At $51s$ the liquefaction condition $(r_u \approx 1)$ is reached in the top fill part. An important observation here is, that the liquefaction region has moved upwards at the top part of the fill. Moreover, between $51s$ and $68s$, the liquefaction state is propagated uniformly from top until the middle fill part. Similarly, by applying a permeability coefficient of an even higher magnitude $(k = 10^{-4}m/s)$, the excess pore pressures developed in the liquefied layers are dissipating more rapidly along the soil column. Hence, a continuous liquefied layer has been formed at $68s$ extending from top to middle fill column. Furthermore, the final liquefaction state $(68s)$ is occuring much earlier compared to the $k = 10^{-5}m/s$ case in which the same conditions are observed at $89s$.

k=10⁻³m/s

Between $35s$ and $43s$ the rate of excess pore pressures generation is increased compared to the analyses with $k = 10^{-6}m/s$, $k = 10^{-5}m/s$ and $k = 10^{-4}m/s$ (Figure 5.15). This increase originates from the top fill part and propagates downwards through the soil column. At $49s$ the liquefaction condition $(r_u \approx 1)$ is reached in a small region at the top fill part. However, between $49s$ until the end of the earthquake $(100s)$, the liquefaction state is not further diffused along the fill column but remains localized in the top fill part that has liquefied.
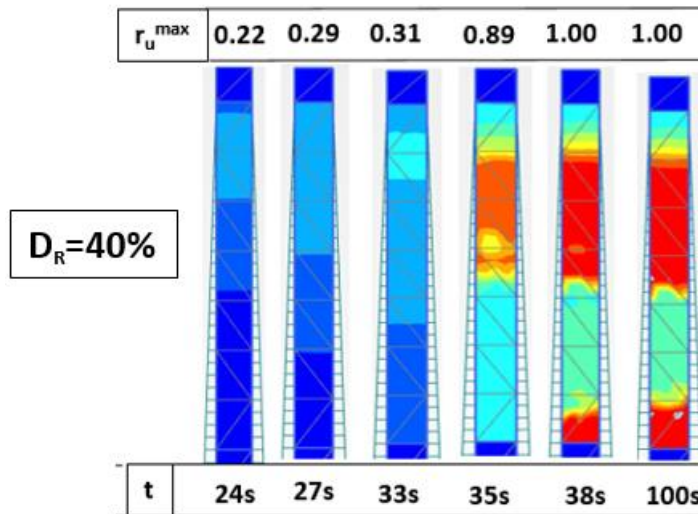

Figure 5.16: Excess pore pressure ratio development in the hydraulic fill of $D_R = 50\%$ for dynamic analysis without consolidation

_**Dr=60%**_

- **(i)** $f_{fund} = 0.59Hz, amax = 0.16g$

k=10⁻⁶m/s

Between $35s$ and $41s$ an increase in excess pore pressures is identified mainly in the lower hydraulic fill layer that propagates upwards through the soil column (Figure 5.17). In a similar manner with the case of $D_R = 50\%$, the excess pore pressure generation is carried out in a considerable slower rate than in the loosely-packed fills ($D_R = 30\%, D_R = 40\%$). After a rapid increase in excess pore pressures at $43s$ the liquefaction condition ($r_u \approx 1$) is reached in the bottom fill part. Between $43s$ until the end of the earthquake ($100s$) the liquefaction condition remains localized in the bottom fill part and does not propagate further along the soil column. Moreover, the magnitude of the permeability coefficient is very low ($k = 10^{-6} \, m/s$). Therefore, there is not enough time for drainage and for a more extensive diffusion of the liquefaction state throughout the fill layer. As a result, at $43s$ the liquefaction condition is restricted to a singular continuous layer at the bottom of the fill and remains unchanged until the end of the earthquake ($100s$). Similarly, the current dynamic analysis with consolidation, for an extremely low value of permeability coefficient ($10^{-6} \, m/s$), nearly resembles the undrained response for the corresponding dynamic analysis without consolidation (Figure 5.18).
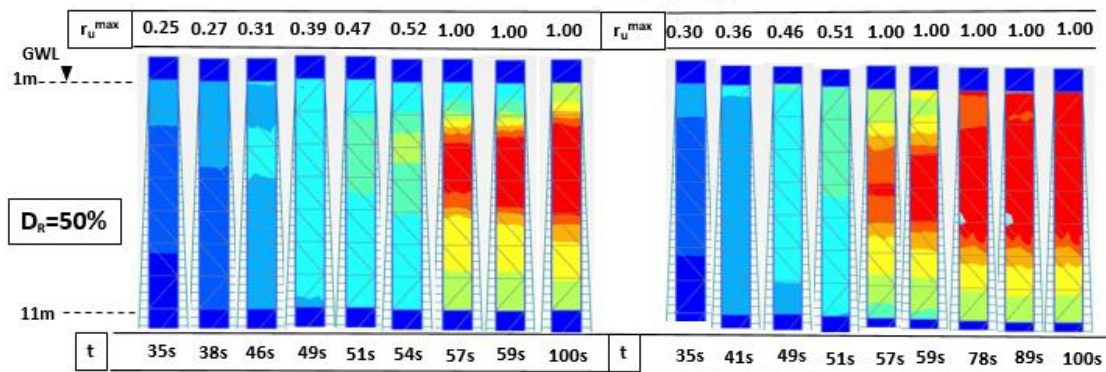
k=10⁻⁵m/s

Between $35s$ and $38s$ the generation of excess pore pressures is slightly increased compared to the analysis with $k = 10^{-6}m/s$ (Figure 5.17). However, the impact of the permeability coefficient has an important role after this point. In particular, once the liquefaction state is reached in the bottom fill part ($43s$) this condition is better diffused upwards until the middle of the fill column between $43s$ and until $46s$. Hence, a continuous liquefied layer has been formed at $46s$ extending from bottom to middle fill column. It is important to note, that between $46s$ until the end of the earthquake ($100s$) the liquefaction condition remains localized in the aforementioned liquefied fill part and does not propagate further along the soil column. Consequently, a higher fill density ($D_R = 60\%$) restricts the spread of the liquefaction condition to an even lesser extent.

- *(i)* f_{fund}=0.59Hz, α_{max}=0.16g

- k=10⁻⁶m/s   • k=10⁻⁵m/s

$r_u{}^{max}$	0.22	0.30	0.51	1.00	1.00	1.00	$r_u{}^{max}$	0.32	0.49	0.53	1.00	1.00	1.00	1.00

GWL 1m

D_R=60%

11m

t	30s	38s	41s	43s	46s	100s	t	30s	38s	41s	43s	46s	73s	100s

- k=10⁻⁴m/s   • k=10⁻³m/s

$r_u{}^{max}$	0.61	0.81	0.85	1.00	1.00	1.00	1.00	$r_u{}^{max}$	0.78	1.00	1.00	1.00	1.00	1.00	1.00

GWL 1m

D_R=60%

11m

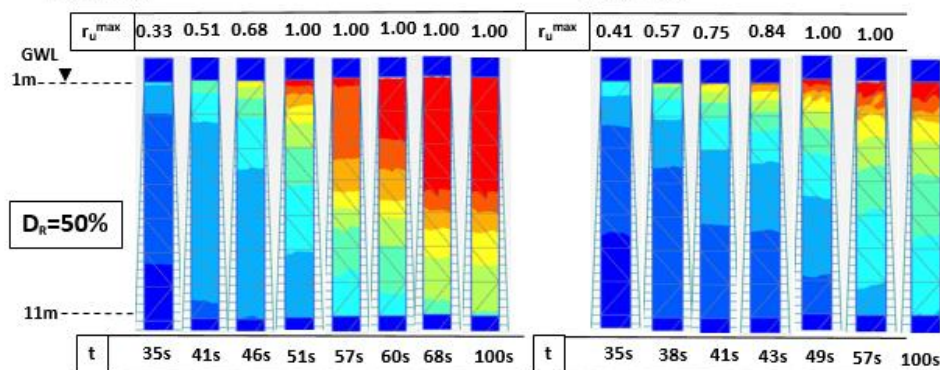| t | 30s | 38s | 41s | 43s | 46s | 49s | 100s | t | 30s | 38s | 41s | 43s | 46s | 49s | 100s |
|---|---|---|---|---|---|---|---|---|---|---|---|---|---|---|
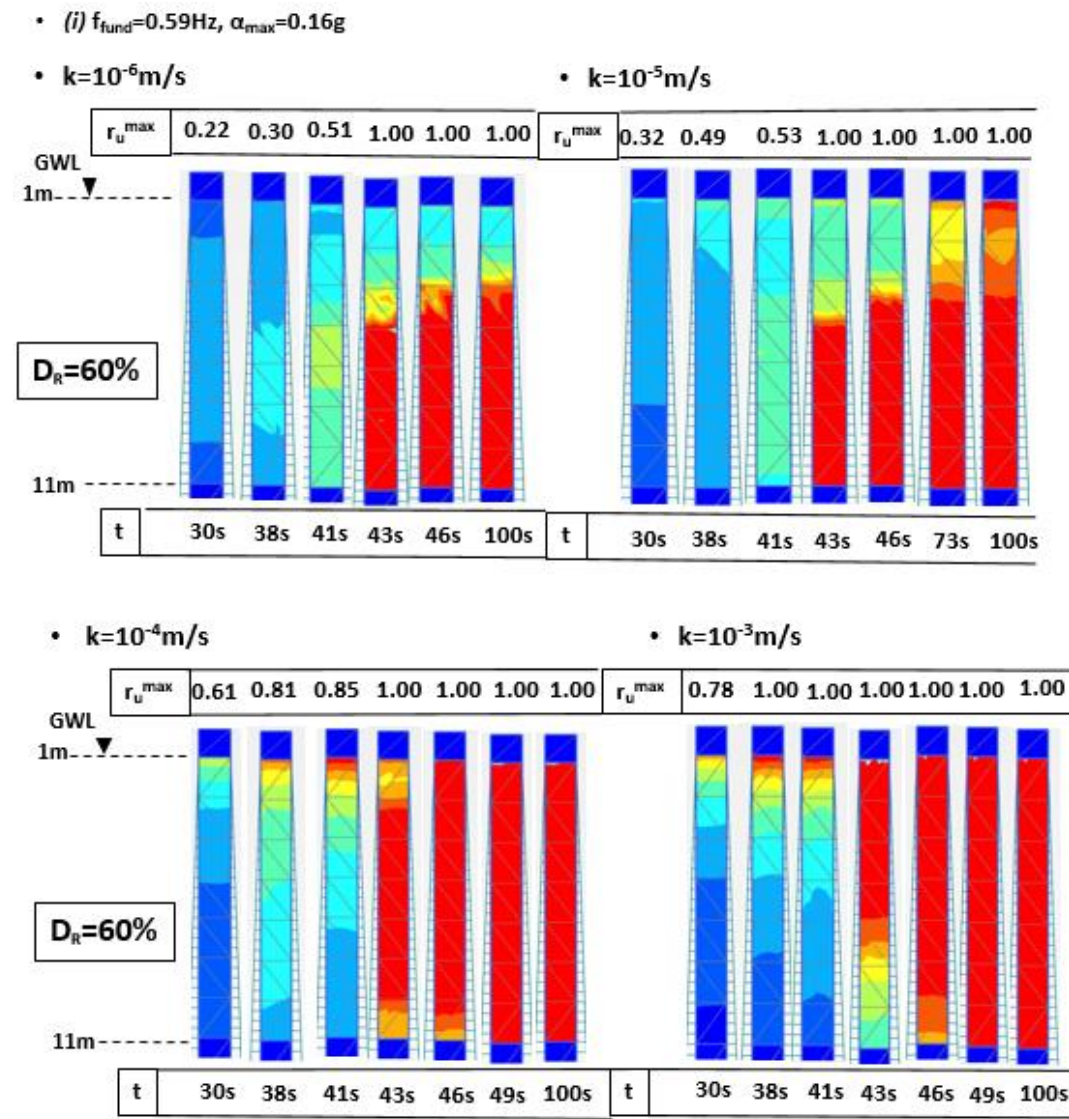
Figure 5.17: Excess pore pressure ratio development in the hydraulic fill of $D_R = 60\%$ for dynamic analysis with consolidation.

k=10⁻⁴m/s

Between $35s$ and $41s$ the rate of excess pore pressures generation is increased compared to the analyses with $k = 10^{-6}m/s$ and $k = 10^{-5}m/s$ (Figure 5.17). This increase originates from the top fill part and propagates downwards through the soil column. At $43s$ the liquefaction condition $(r_u \approx 1)$ is reached in the top fill part. Similarly with the $D_R = 50\%$ case, the liquefaction region has moved upwards at the top fill part. Moreover, between $43s$ and $46s$, the liquefaction state is propagated uniformly from top until the mid-upper fill part. It is important to note, between $46s$ until the end of the earthquake ($100s$) the liquefaction condition remains localized in the aforementioned liquefied fill part which is attributed the the high relative density of the fill.

_k=10⁻³m/s_

Between $35s$ and $38s$ the rate of excess pore pressures generation is increased compared to the analyses with $k = 10^{-6}m/s$, $k = 10^{-5}m/s$ and $k = 10^{-4}m/s$ (Figure 5.17). This increase originates from the top fill part and propagates downwards through the soil column. At $38s$ the liquefaction condition $(r_u \approx 1)$ is reached in a small region at the top fill part. However, between $38s$ until the end of the earthquake $(100s)$, the liquefaction state is not further diffused along the fill column but remains localized in the top fill part that has liquefied.
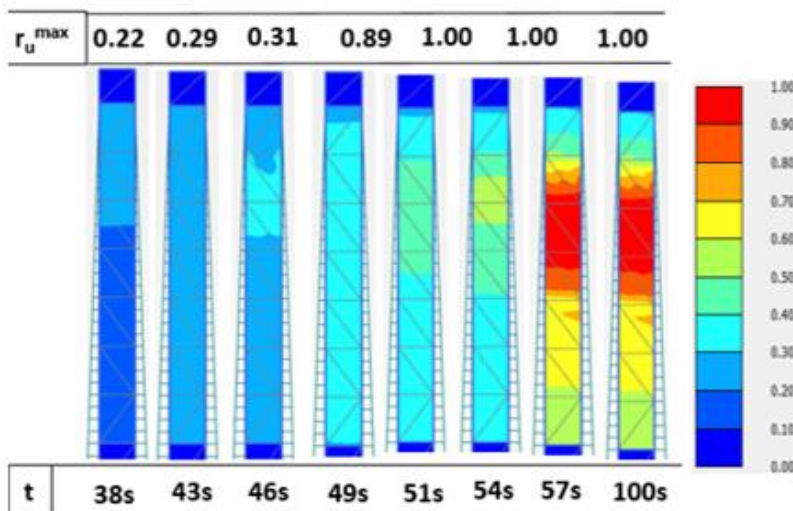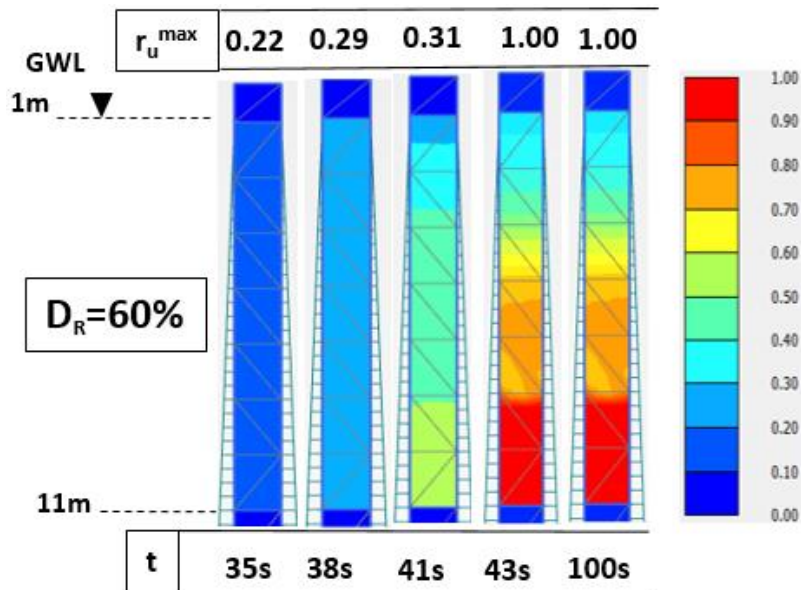

Figure 5.18: Excess pore pressure ratio development in the hydraulic fill of $D_R = 60\%$ for dynamic analysis without consolidation

5.7 Conclusions

- PM4Sand model is indeed applicable for the prediction of earthquake induced liquefaction in hydraulic fills
- The empirical nature of the NCEER method is its largest drawback, as it accounts for varying loading condition and different soil types. Consequently, this method can be conservative for the design, as for the current thesis project, it predicted liquefaction for almost all the hydraulic fills ($D_R = 30\%$ to $D_R = 60\%$) analyzed for all different earthquake motions
- On the other hand, PM4Sand model provides the opportunity to conduct a site-specific analysis for each case by giving results that are much more realistic to what has been observed in real practise
- The effect of the in-situ state of the fill has a critical role on the liquefaction susceptibility in PM4Sand model which is more representative to what has been observed in reality. In particular, the relative density D_R, as an input parameter, is the most predominant factor concerning the liquefaction triggering of hydraulic fills
- According to PM4Sand model, the loosely-packed fills ($D_R = 30\%$ and $D_R = 40\%$) are indeed more susceptible to liquefaction compared to the densely-packed fills ($D_R = 50\%$ and $D_R = 60\%$) which showed less or even no liquefaction potential due to the earthquake events
- Regarding the dynamic analyses with consolidation, the results related to the earthquake-induced liquefaction of the fills is more representative to realistic conditions as there is a better distribution of excess pore pressures along the soil column
- Regarding the dynamic analyses without consolidation, there is a better diffusion of excess pore pressures in the loosely-packed fills ($D_R = 30\%$ and $D_R = 40\%$) for the signals of low dominant frequencies regardless the peak ground acceleration values of the input signal. In the densely-packed fills ($D_R = 50\%$ and $D_R = 60\%$) the same phenomenon takes pace more for the signals of high dominant frequencies. In the rest of the signals there is localization of liquefied zones in distinct parts within the fill layer

Bibliography

Ambraseys, N. (1988). Engineering Seismology. *Int. J. Earth-Geology-University of Thessaloniki and Institute of quake Eng. Struct.Dyn.*, 101-105.

Bastidas, A. M. (2016). *Ottawa F-65 Sand Characterization.* University of California at Davis: Department of Civil and Environmental Engineering.

Been, K., & Jefferies, M. (1985). A state parameter for sands. *Geotechnique 35, (2)*, 99-112.

Bolton, M. (1986). The strength and dilatancy of sands. *Geotechnique 36, (1)*, 65-78.

Boulanger, R. W. (2003a). Relating Kα to relative state parameter index. *J. Geotechnical and Environmental Eng., ASCE 129(8)*, 770-73.

Boulanger, R. W., & Ziotopoulou, K. (2015). *PM4Sand (Version3): A Sand Plasticity Model for Earthquake Engineering Applications.* Center for Geotechnical Modeling Department of Civil and Environmental Engineering, University of California Davis, California.

Brinkgreve, R., Engin, E., & Engin, H. (2010). *Validation of empirical formulas to derive model parameters for sands.* Technical Report, TU Delft, Plaxis.

Casagrande, A. (1936). Characteristics of Cohesionless Soils Affecting the Stability of Slopes and Earth Fills. *Journal of the Boston Society of Civil Engineers*, 257-276.

Chang, F., & Krinitzsky, E. (1977). Duration, spectral content and predominant period of strong motion earthquake records from western United States. *US Army Corps of Engineers Waterways Experiment Station*.

Dafalias, Y., & Manzari, M. (2004). Simple plasticity sand model accounting for fabric change effects. *Journal of Engineering Mechanics, ASCE, 130(6)*, 622-634.

Dyvik, R. T. (1987). Comparison of truly undrained and constant volume direct simple shear test. *Geotechnique 37(1)*, 3-10.

Gonzalo , C. (4234). likvefaction. *118(3)*, 2342-2323.

Hanks, T., & McGuire, R. (1981). The character of high frequency strong ground motion. *Bull. Seism. Soc. Am. 120, (6)(25)*, 2071-2095.

Hicks, M., & Boughrarou, R. (1998). Finite element analysis of the Nerlerk underwater berm failures. *Geotechnique 35, (2)*, 169-185.

Hicks, M., & Onisiphorou, C. (2005). Stochastic evaluation of static liquefaction in a predominantly dilative sand fill. *Geotechnique 55, (2)*, 123-133.

Idriss, I. (1999). An Update to the Seed-Idriss Simplified Procedure for Evaluating Liquefaction Potential. *Proceedings of TRB Workshop on New Approaches to Liquefaction, Federal Highway Administration.* Washington DC, 10 January 1999.

Idriss, I., & Boulanger, R. (2008). *Soil Liquefaction During Earthquakes.* USA: Lynx Communication Group Inc.

Isihara, K. (1984). Post-earthquake failure of tailings, journal=Soil and Foundation.

Isihara, K. (1985). Stability of natural deposits during earthquakes. *11th Int. Conf. on Soil Mechanics and Foundation Engineering.*

Isihara, K. (1996). Soil behaviour in Eartqhquake Geotechnics. *The Oxford Engineering Science Series, (46)*.

Konrad, J.-M. (1988). Interpretation of flat plate dilatometer tests in sands in terms of the state parameter. *Geotechnique 38, (2)*, 263-77.

Kramer, S. (1996). *Geotechnical Earthquake Engineering.* Prentice Hall-Inc, New Jersey, USA.

Kuhlmeyer, R., & Lysmer, J. (1973). Finite element method accuracy for wave propagation problems. *Technical Report, Journal of the soil mechanics and foundation division, 99*, 421-427.

Li, X., & Wang, Y. (1998). Linear representation of steady-state line for sand. *Journal of Geotechnical and Geoenvironmental Engineering, 124(12)*, 1215-7.

Nemat, & Tobita. (1982). Influence of fabric on liquefaction and densification potential of cohesionless sand. 43-62.

Pyke , R., Chan, C., & Seed, H. (1974). Settlement and Liquefaction of Sands under Multi-directional Shaking. *Earthquake Engineering Research Center*, *No. EERC 74-2.* University of California at Berkley.

Robertson, P. (2009). Evaluation of Flow Liquefaction and Liquefied Strength. *Journal of Geotechnical and Geoenvironmental Engineering*, 842-853.

Robertson, P., & Wride, C. (1998). Evaluating cyclic liquefaction potential using the cone penetration test. *Canadian Geotechnical Journal 35, (3)*, 442-459.

Saada, A. (1988). Hollow cylinder torsional devices: their advantages and limitations. *In Symposium on advanced triaxial testing of soil and rock. Edited by R.T. Donaghe, R.C. Chaney, and Marshall L. Silver. American Society for Testing and Materials,Special Technical Publication 977*, (pp. 766-795).

Schofield, A., & Wroth, C. (1968). Critical State Soil Mechanics. *New York, McGraw-Hill*.

Seed, H. (1976). Evaluation of Soil Liquefaction Effects on Level Ground During Earthquakes. *American Society of Civil Engineers, presentet at ASCE National Convention, Philadelphia*, 1-104.

Seed, H. (1983). Earthquake resistant design of earthquake dams, in. *Proceedings, Symposium on Seismic Design of Embankments and Caverns*, (pp. 41-64). Pennsylvania, ASCE, NY.

Seed, H., & De Alba, P. (1986). Use of CPT and SPT Test for evaluating the liquefaction resistance of soils. *Use of in situ Tests in Geotechnical Engineering*, 281-302.

Seed, H., & Idriss. (1982). Ground motions and soil liquefaction during earthquakes: Berkley. *Earthquake Engineering Research Institute Monograph*.

Seed, H., & Idriss, I. (1968). AN ANALYSIS OF GROUND MOTION DURING THE 1957 SAN FRANCISCO EARTHQUAKE. *Bulletin of the Seismological Society of America 58, (6)*.

Seed, H., & Idriss, I. (1971). Simplified procedure for evaluating the liquefaction potential. *Journal of Soil Mechanics and Foundation Division 97, (9)*, 1249-1273.

Seed, H., & Lee, K. (1996). Liquefaction of saturated sand during cyclic loading. *Journal of Soil Mechanics and Foundation Engineering*, 105-134.

Uthayakumar, M., & Vaid, Y. (1998). Static liquefaction of sands under multiaxial loading. *Canadian Geotechnical Journal 35*, 273-283.

Vaid, Y., & Finn, W. (1979). Static shear and liquefaction potential. *J. Geotechnical Div. ASCE 105, (GT10)*, 1233-246.

Vaid, Y., & Sivathayalan, S. (1996). Static and cyclic liquefaction potential of Fraser Delta Sand in simple shear and triaxial tests. *Canadian Geotechnical J., (33)*, 281-89.

Van't Hoff, J., & Nooy van der Kolff, A. (2012). *Hydraulic Fill Manual: For Dredging and Reclamation Works.* CRC Press, Taylor and Francis Group, The Netherlands.

Youd, T., & Idriss, I. (2001). "Liquefaction resistance of soils: summary report from the 1996 NCEER and 1998 NCEER/NSF workshops on evaluation of liquefaction resistance of soils. *Journal of Geotechnical and Geoenvironmental Engineering, 127(4)*, 297-313.

APPENDIX A

A.1 Earthquake motions
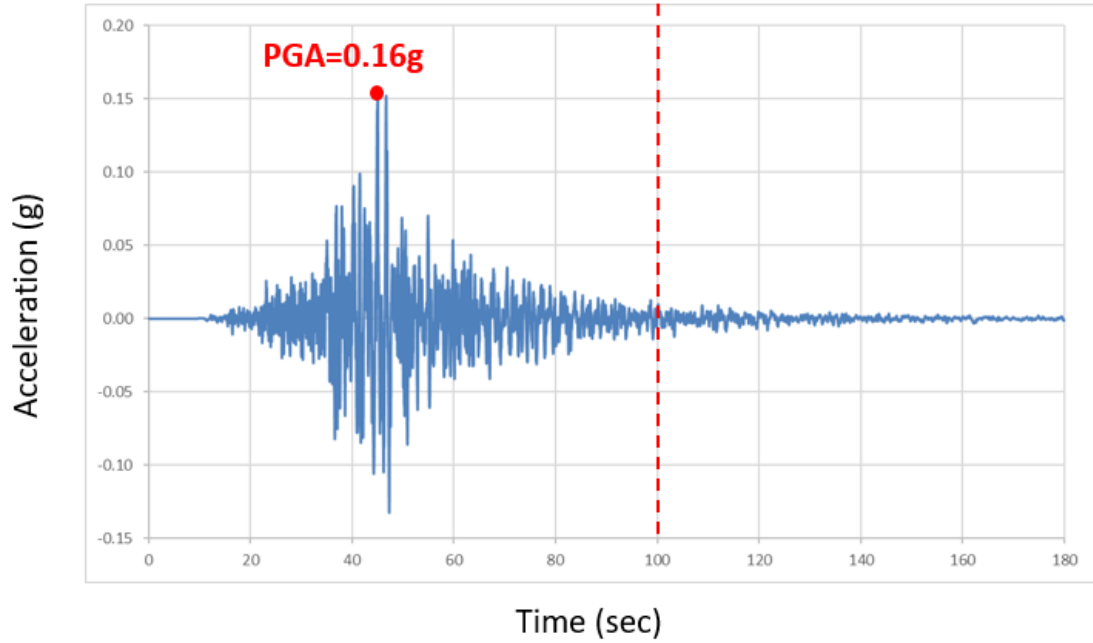
Figure A.1: Filtered and corrected acceleration-time record with Seismosignal software, measured in the north-south direction and scaled at 0.16g, *(i)*
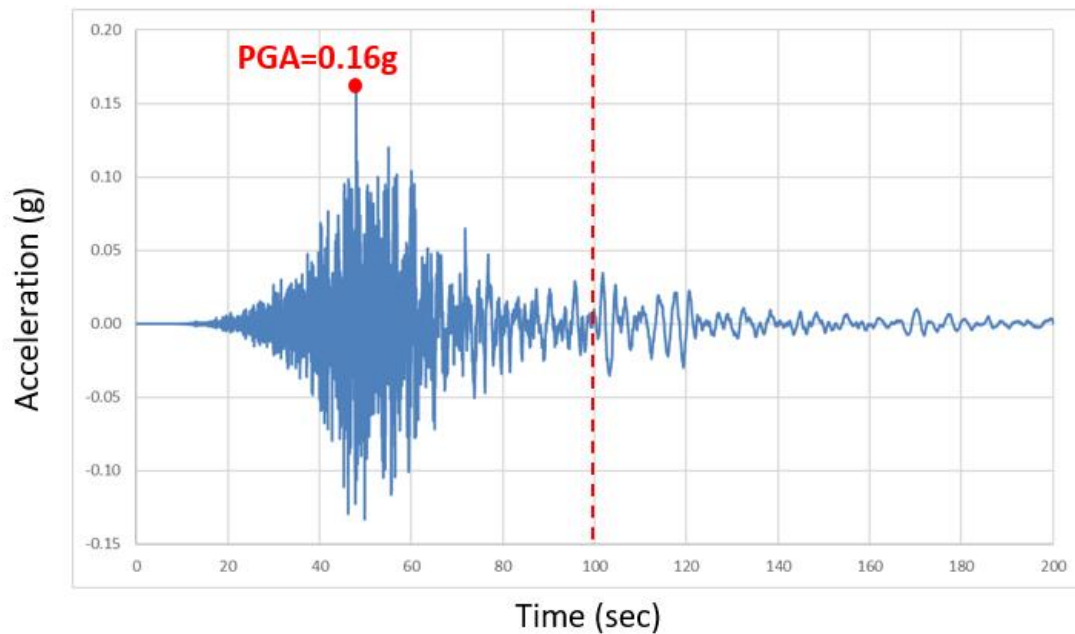
Figure A.2: Filtered and corrected acceleration-time record with Seismosignal software, measured in the east-west direction and scaled at 0.16g, *(ii)*
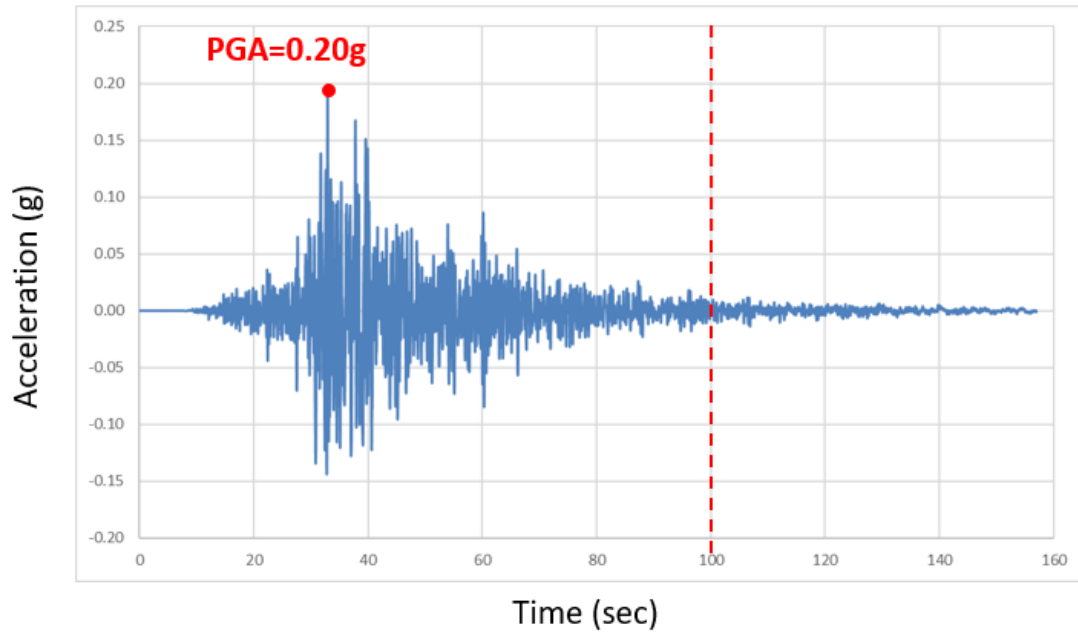
Figure A.3: Filtered and corrected acceleration-time record with Seismosignal software, measured in the north-south direction and scaled at 0.16g, *(iii)*
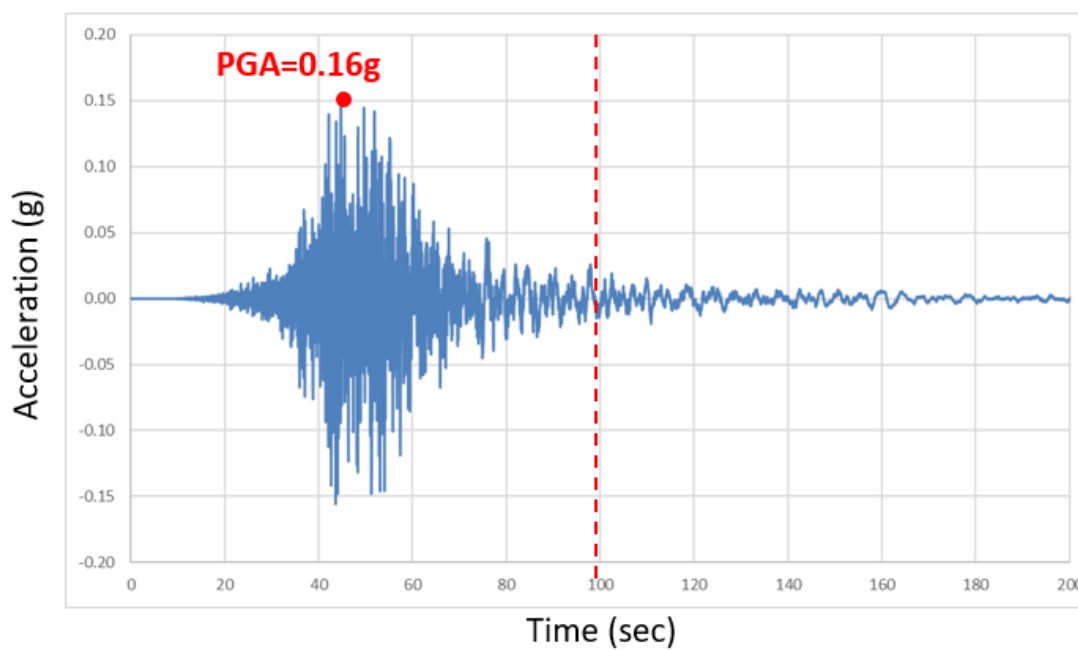
Figure A.4: Filtered and corrected acceleration-time record with Seismosignal software, measured in the north-south direction and scaled at 0.16g, *(iv)*
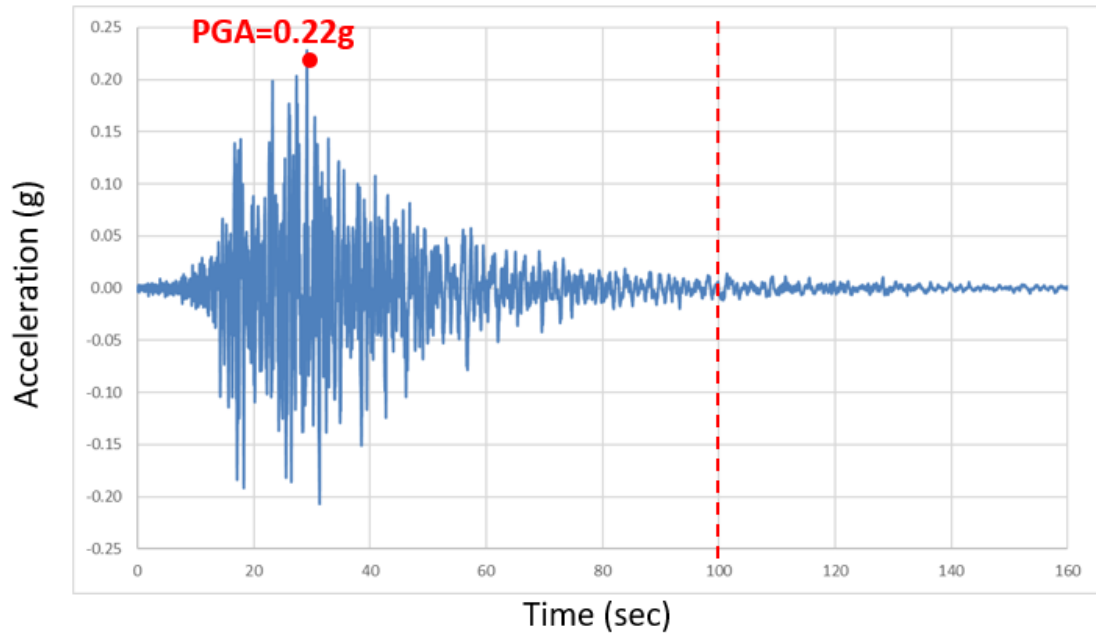
Figure A.5: Filtered and corrected acceleration-time record with Seismosignal software., measured in the north-south direction and scaled at 0.16g, *(v)*
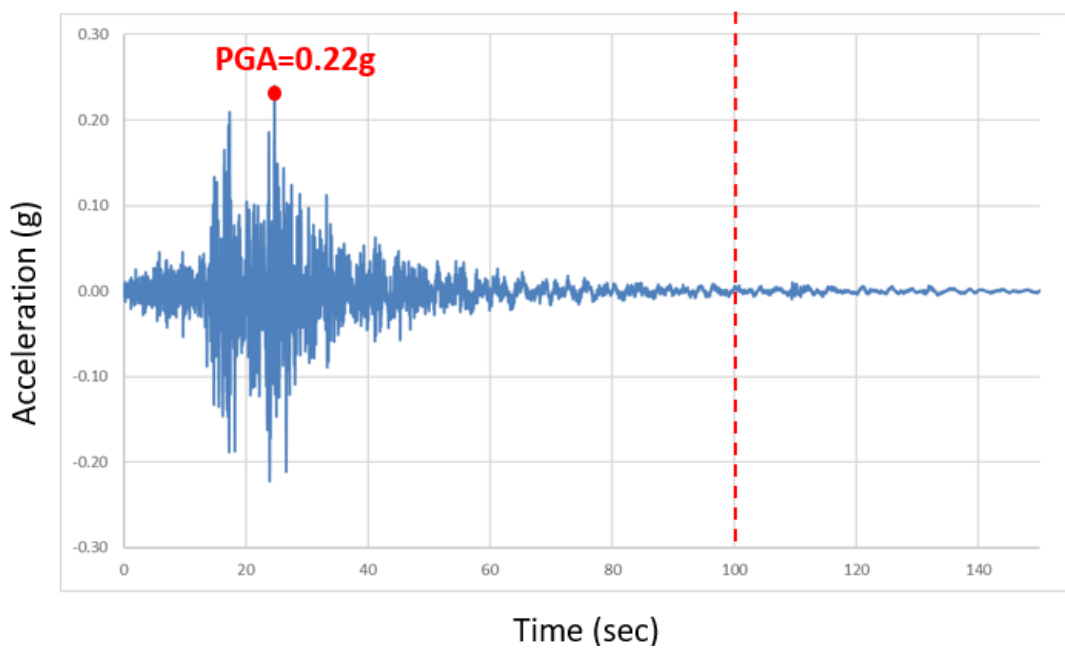
Figure A.6: Filtered and corrected acceleration-time record with Seismosignal software, measured in the east-west direction and scaled at 0.16g, *(vi)*
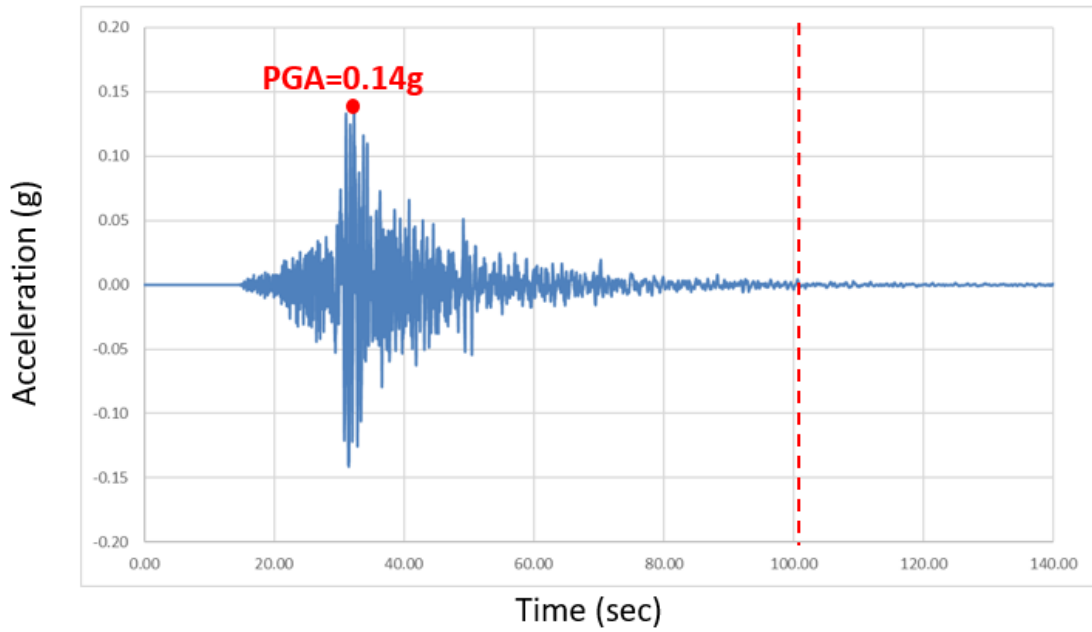
Figure A.7: Filtered and corrected acceleration-time record with Seismosignal software, measured in the east-west direction and scaled at 0.16g, *(vii)*
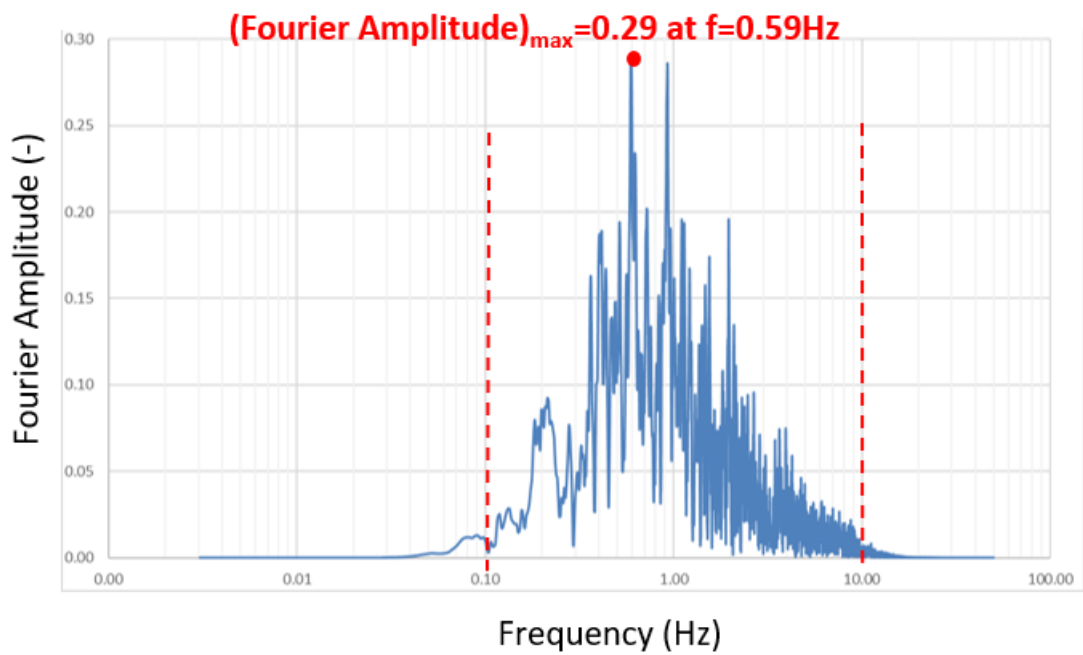
Figure A.8: Frequency amplitude spectrum of the input acceleration ground motion ($PGA = 0.16g$) with Seismosignal software, *(i)*
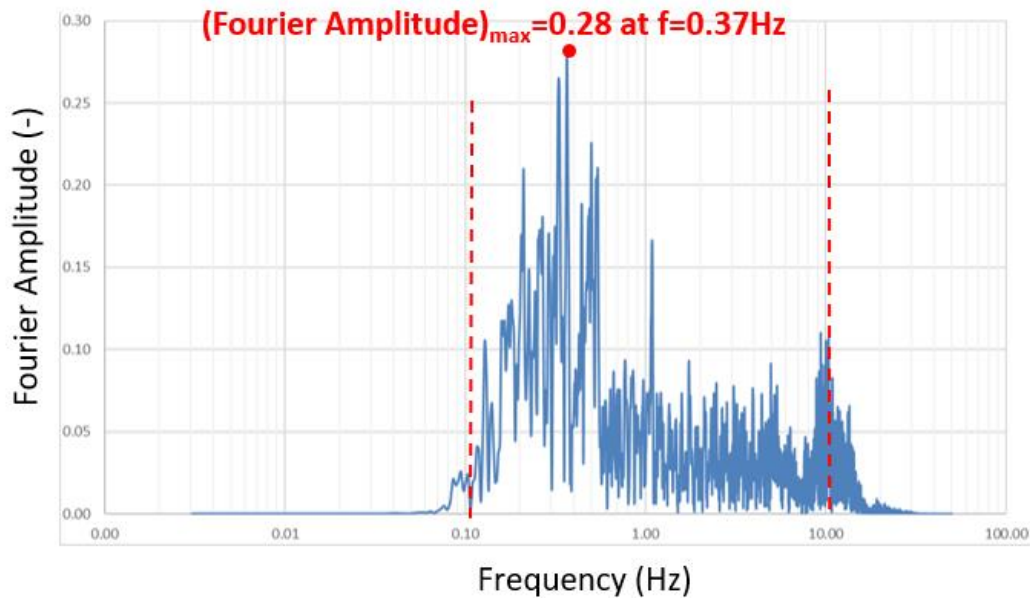
Figure A.9: Frequency amplitude spectrum of the input acceleration ground motion ($PGA = 0.16g$) with Seismosignal software, *(ii)*
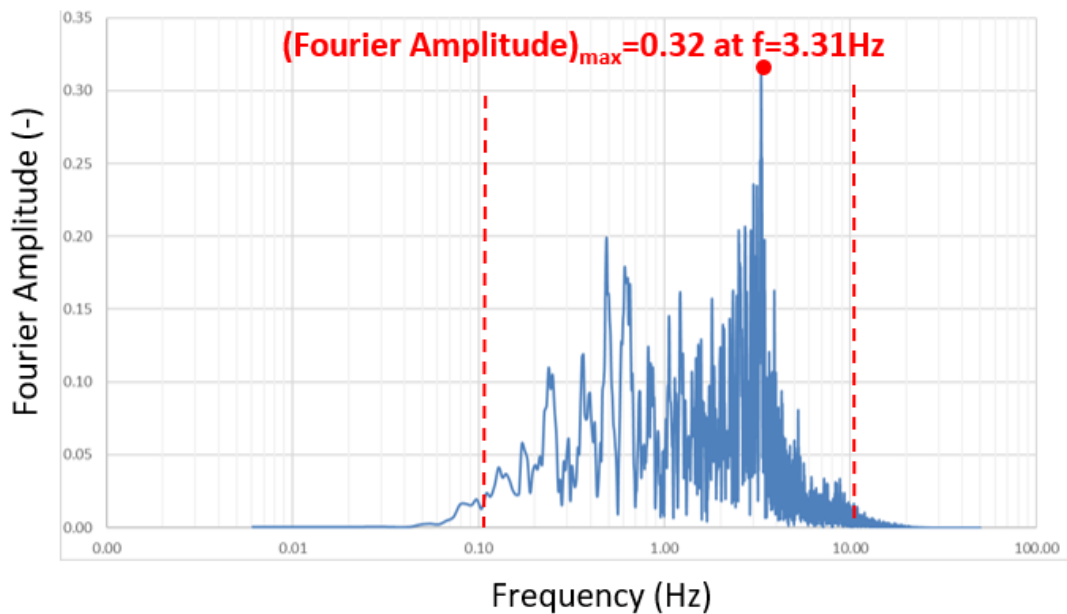
Figure A.10: Frequency amplitude spectrum of the input acceleration ground motion ($PGA = 0.20g$) with Seismosignal software, *(iii)*
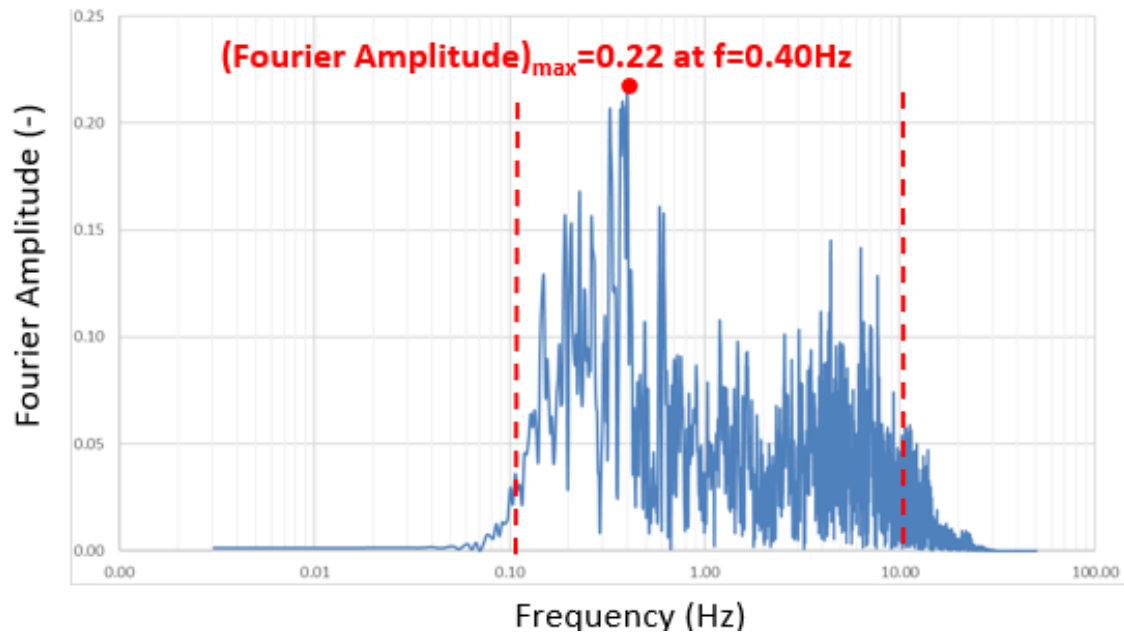
Figure A.11: Frequency amplitude spectrum of the input acceleration ground motion ($PGA = 0.16g$) with Seismosignal software, *(iv)*
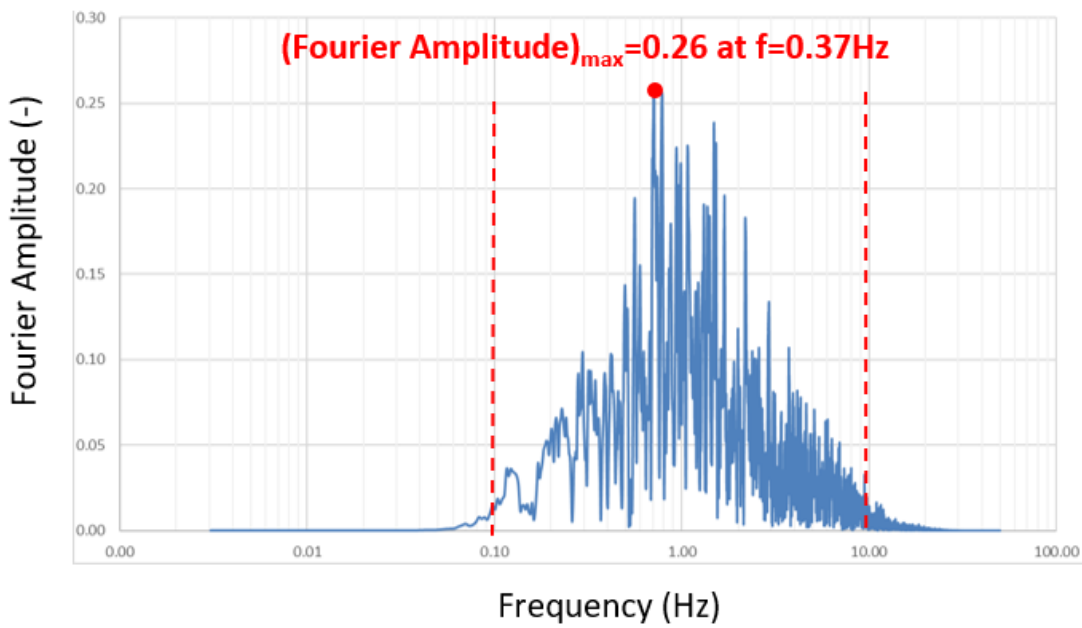
Figure A.12: Frequency amplitude spectrum of the input acceleration ground motion ($PGA = 0.22g$) with Seismosignal software, *(v)*

(Fourier Amplitude)$_{max}$=0.21 at f=5.47Hz
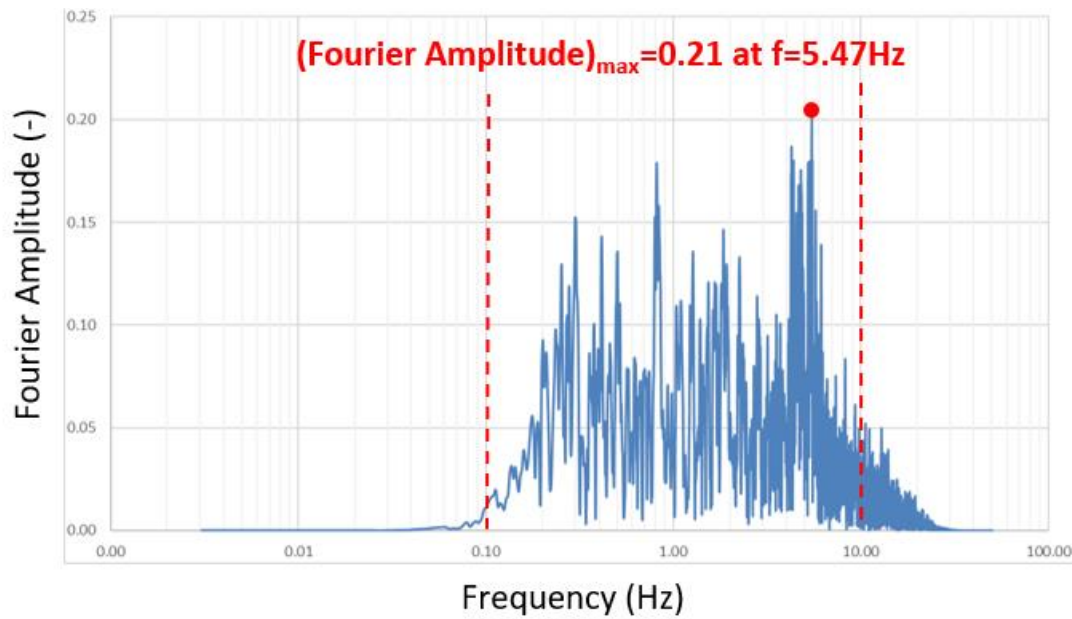
Figure A.13: Frequency amplitude spectrum of the input acceleration ground motion ($PGA = 0.22g$) with Seismosignal software, *(vi)*
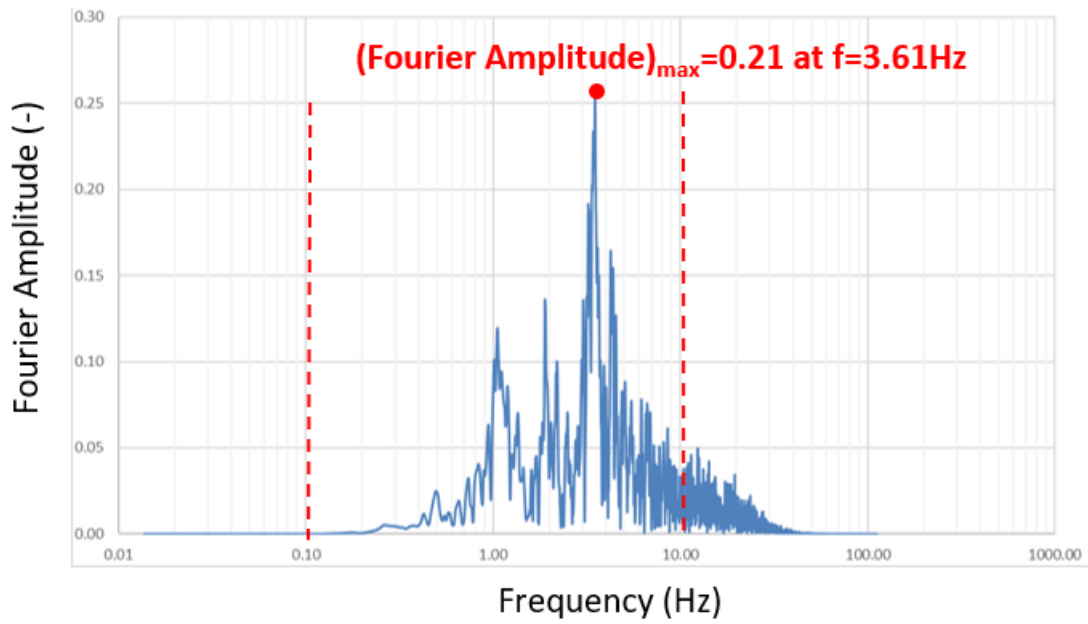
Figure A.14: Frequency amplitude spectrum of the input acceleration ground motion ($PGA = 0.14g$) with Seismosignal software, *(vii)*

A.2 Liquefaction Potential according to NCEER Method

Soil column	Depth (m)	CSR	CRR$_{7.5}$	MSF	K$_\sigma$	CRR	FS	σ$_{vo}$ (kPa)	σ'$_{vo}$ (kPa)	r$_d$	α(z)	β(z)	C$_\sigma$
D$_R$=60%	1	0.130	0.176	0.88	1.21	0.186	**1.43**	17.4	17.4	1.001	-0.027	0.003	0.117
	2	0.221	0.066	0.88	1.12	0.065	**0.29**	32.4	18.96	0.996	-0.0771	0.009	
	3	0.220			1.09	0.063	**0.29**	48.6	28.44	0.989	-0.1339	0.015	
	4	0.218			1.07	0.062	**0.28**	64.8	37.92	0.983	-0.1971	0.022	
	5	0.217			1.06	0.061	**0.28**	81	47.4	0.975	-0.2662	0.030	
D$_R$=30%	6	0.215			1.04	0.060	**0.28**	97.2	56.88	0.968	-0.3408	0.038	0.073
	7	0.213			1.03	0.059	**0.28**	113.4	66.36	0.959	-0.4202	0.047	
	8	0.211			1.02	0.059	**0.28**	129.6	75.84	0.950	-0.5039	0.057	
	9	0.209			1.01	0.058	**0.28**	145.8	85.32	0.941	-0.5913	0.066	
	10	0.207			1.00	0.058	**0.28**	162	94.8	0.931	-0.6818	0.076	
	11	0.211	0.250	0.88	0.99	0.216	**1.03**	195.8	111.32	0.921	-0.7746	0.087	
	12	0.208			0.97	0.213	**1.02**	213.6	121.44	0.910	-0.8692	0.097	
	13	0.206			0.96	0.210	**1.02**	231.4	131.56	0.899	-0.9648	0.107	
	14	0.203			0.95	0.208	**1.02**	249.2	141.68	0.888	-1.0608	0.118	
	15	0.201			0.94	0.206	**1.03**	267	151.8	0.877	-1.1564	0.128	
	16	0.198			0.93	0.204	**1.03**	284.8	161.92	0.865	-1.251	0.138	
	17	0.195			0.92	0.202	**1.03**	302.6	172.04	0.854	-1.3438	0.148	
D$_R$=70%	18	0.193			0.91	0.200	**1.04**	320.4	182.16	0.842	-1.4342	0.158	0.147
	19	0.190			0.91	0.198	**1.04**	338.2	192.28	0.831	-1.5215	0.167	
	20	0.186			0.90	0.197	**1.06**	348	199.2	0.819	-1.6052	0.176	
	21	0.185			0.89	0.195	**1.06**	373.8	212.52	0.808	-1.6845	0.184	
	22	0.182			0.88	0.193	**1.06**	391.6	222.64	0.796	-1.759	0.191	
	23	0.180			0.88	0.192	**1.07**	409.4	232.76	0.785	-1.828	0.198	
	24	0.177			0.87	0.191	**1.08**	427.2	242.88	0.774	-1.8911	0.204	
	25	0.175			0.87	0.189	**1.08**	445	253	0.764	-1.9478	0.210	
	26	0.172	0.433	0.88	0.81	0.308	**1.78**	462.8	263.12	0.754	-1.9977	0.214	
	27	0.170			0.80	0.305	**1.79**	480.6	273.24	0.744	-2.0405	0.218	
	28	0.168			0.80	0.302	**1.80**	498.4	283.36	0.734	-2.0758	0.221	
	29	0.166			0.79	0.299	**1.80**	516.2	293.48	0.726	-2.1034	0.223	
	30	0.164			0.78	0.297	**1.81**	534	303.6	0.717	-2.123	0.224	
	31	0.163			0.77	0.293	**1.80**	564.2	318.68	0.710	-2.1346	0.224	
	32	0.162			0.77	0.291	**1.80**	582.4	328.96	0.702	-2.138	0.223	
D$_R$=80%	33	0.160			0.76	0.289	**1.80**	600.6	339.24	0.696	-2.1332	0.221	0.198
	34	0.159			0.76	0.286	**1.80**	618.8	349.52	0.690	-2.1203	0.219	
	35	0.158			0.75	0.284	**1.80**	637	359.8	0.685	-2.0993	0.215	
	36	0.157			0.74	0.282	**1.80**	655.2	370.08	0.680	-2.0705	0.211	
	37	0.156			0.74	0.280	**1.80**	673.4	380.36	0.677	-2.0339	0.205	
	38	0.155			0.73	0.278	**1.79**	691.6	390.64	0.674	-1.99	0.199	
	39	0.155			0.73	0.276	**1.78**	709.8	400.92	0.672	-1.9389	0.193	
	40	0.154			0.72	0.274	**1.77**	728	411.2	0.671	-1.8811	0.185	
	41	0.154			0.72	0.272	**1.76**	746.2	421.48	0.671	-1.817	0.177	

Table A.15: Liquefaction susceptibility analysis for the hydraulic fill of $D_R = 30\%$ and the whole soil column using the NCEER method

		α_max=0.14g			α_max=0.16g			α_max=0.20g			α_max=0.22g		
Soil column	Depth (m)	CSR	CRR	FS	CSR	CRR	FS	CSR	CRR	FS	CSR	CRR	FS
D_R=60%	1	0.13	0.19	**1.43**	0.13	0.19	**1.43**	0.13	0.19	**1.43**	0.13	0.19	**1.43**
	2	0.16	0.09	**0.58**	0.18	0.09	**0.51**	0.22	0.09	**0.41**	0.25	0.09	**0.37**
	3	0.16	0.09	**0.57**	0.18	0.09	**0.49**	0.22	0.09	**0.40**	0.24	0.09	**0.36**
	4	0.15	0.09	**0.56**	0.18	0.09	**0.49**	0.22	0.09	**0.39**	0.24	0.09	**0.35**
	5	0.15	0.08	**0.55**	0.17	0.08	**0.48**	0.22	0.08	**0.39**	0.24	0.08	**0.35**
D_R=40%	6	0.15	0.08	**0.55**	0.17	0.08	**0.48**	0.22	0.08	**0.38**	0.24	0.08	**0.35**
	7	0.15	0.08	**0.55**	0.17	0.08	**0.48**	0.21	0.08	**0.38**	0.24	0.08	**0.35**
	8	0.15	0.08	**0.55**	0.17	0.08	**0.48**	0.21	0.08	**0.38**	0.23	0.08	**0.35**
	9	0.15	0.08	**0.55**	0.17	0.08	**0.48**	0.21	0.08	**0.38**	0.23	0.08	**0.35**
	10	0.15	0.08	**0.55**	0.17	0.08	**0.48**	0.21	0.08	**0.38**	0.23	0.08	**0.35**

Table A.16: Liquefaction susceptibility analysis for the hydraulic fill of $D_R = 30\%$ using the NCEER method for seven different earthquake motions.

		α_max=0.14g			α_max=0.16g			α_max=0.20g			α_max=0.22g		
Soil column	Depth (m)	CSR	CRR	FS	CSR	CRR	FS	CSR	CRR	FS	CSR	CRR	FS
D_R=60%	1	0.13	0.19	**1.43**	0.13	0.19	**1.43**	0.13	0.19	**1.43**	0.13	0.19	**1.43**
	2	0.16	0.13	**0.82**	0.18	0.13	**0.72**	0.22	0.13	**0.57**	0.25	0.13	**0.52**
	3	0.16	0.12	**0.80**	0.18	0.12	**0.70**	0.22	0.12	**0.56**	0.25	0.12	**0.51**
	4	0.16	0.12	**0.78**	0.18	0.12	**0.68**	0.22	0.12	**0.55**	0.24	0.12	**0.50**
	5	0.15	0.12	**0.77**	0.18	0.12	**0.67**	0.22	0.12	**0.54**	0.24	0.12	**0.49**
D_R=50%	6	0.15	0.12	**0.76**	0.17	0.12	**0.67**	0.22	0.12	**0.54**	0.24	0.12	**0.49**
	7	0.15	0.12	**0.76**	0.17	0.12	**0.67**	0.22	0.12	**0.53**	0.24	0.12	**0.48**
	8	0.15	0.11	**0.76**	0.17	0.11	**0.66**	0.21	0.11	**0.53**	0.24	0.11	**0.48**
	9	0.15	0.11	**0.76**	0.17	0.11	**0.66**	0.21	0.11	**0.53**	0.23	0.11	**0.48**
	10	0.15	0.11	**0.76**	0.17	0.11	**0.66**	0.21	0.11	**0.53**	0.23	0.11	**0.48**

Table A.17: Liquefaction susceptibility analysis for the hydraulic fill of $D_R = 50\%$ using the NCEER method

		α_max=0.14g			α_max=0.16g			α_max=0.20g			α_max=0.22g		
Soil column	Depth (m)	CSR	CRR	FS	CSR	CRR	FS	CSR	CRR	FS	CSR	CRR	FS
D_R=60%	1	0.13	0.19	**1.43**	0.13	0.19	**1.43**	0.13	0.19	**1.43**	0.13	0.19	**1.43**
	2	0.16	0.18	**1.16**	0.18	0.18	**1.02**	0.23	0.18	**0.81**	0.25	0.18	**0.74**
	3	0.16	0.18	**1.12**	0.18	0.18	**0.98**	0.22	0.18	**0.78**	0.25	0.18	**0.71**
	4	0.16	0.17	**1.10**	0.18	0.17	**0.96**	0.22	0.17	**0.77**	0.25	0.17	**0.70**
	5	0.16	0.17	**1.08**	0.18	0.17	**0.94**	0.22	0.17	**0.75**	0.24	0.17	**0.69**
D_R=60%	6	0.15	0.16	**1.06**	0.18	0.16	**0.93**	0.22	0.16	**0.75**	0.24	0.16	**0.68**
	7	0.15	0.16	**1.06**	0.17	0.16	**0.92**	0.22	0.16	**0.74**	0.24	0.16	**0.67**
	8	0.15	0.16	**1.05**	0.17	0.16	**0.92**	0.22	0.16	**0.73**	0.24	0.16	**0.67**
	9	0.15	0.16	**1.05**	0.17	0.16	**0.92**	0.21	0.16	**0.73**	0.24	0.16	**0.67**
	10	0.15	0.15	**1.04**	0.17	0.15	**0.91**	0.21	0.15	**0.73**	0.23	0.15	**0.66**

Table A.18: Liquefaction susceptibility analysis for the hydraulic fill of $D_R = 60\%$ using the NCEER method

Soil column	Depth(m) (m)	σ'$_v$ (kPa)	p' (kPa)	σ'$_h$ (kPa)	γ$_{unsat}$ (kN/m³)	ρ (kg/m³)	m (m)	G$_{o,ref}$ (kPa)	G$_o$ (kpA)	v$_s$ (m/s)	v$_{s,average}$ (m/s)	f$_{max}$ (Hz)	Δl$_{max}$ (m)	Δt$_{max}$ (s)
	0	0	0	0					0	102				
D$_R$=60%	0,5	9	7	4	17,4	1,77	0,5125	100800	18472	102	109	11	1,23	0,011
	1	17	13	7					26350	122				
	1,5	14	11	6					14144	93				
	2	19	14	9					16333	99				
	2,5	24	18	11					18260	105				
	3	28	21	13					20003	110				
	3,5	33	25	15					21606	114				
	4	38	28	17					23098	118				
	4,5	43	32	19					24499	122				
	5	47	36	22					25824	125				
	5,5	52	39	24					27085	128				
D$_R$=30%	6	57	43	26	16,2	1,65	____	____	28289	131	129	11	1,47	0,011
	6,5	62	46	28					29444	134				
	7	66	50	30					30555	136				
	7,5	71	53	32					31628	138				
	8	76	57	35					32665	141				
	8,5	81	60	37					33670	143				
	9	85	64	39					34647	145				
	9,5	90	68	41					35596	147				
	10	95	71	43					36521	149				
	10,5	100	75	45					37423	151				
	11	104	78	47					38303	152				
	11,5	116	87	49					76182	205				
	12	121	91	51					77759	207				
	12,5	127	95	53					79302	209				
	13	132	99	55					80813	211				
	13,5	137	102	57					82294	213				
	14	142	106	59					83747	215				
	14,5	147	110	62					85173	217				
	15	152	114	64					86574	218				
	15,5	157	118	66					87951	220				
	16	162	121	68					89305	222				
	16,5	167	125	70					90638	224				
	17	172	129	72					91949	225				
	17,5	177	133	74					93241	227				
	18	182	137	76					94514	228				
D$_R$=70%	18,5	187	140	79	17,8	1,81	0,4813	107600	95768	230	229	11	2,61	0,011
	19	192	144	81					97005	231				
	19,5	197	148	83					98225	233				
	20	202	152	85					99429	234				
	20,5	207	156	87					100618	235				
	21	213	159	89					101792	237				
	21,5	218	163	91					102951	238				
	22	223	167	93					104096	240				
	22,5	228	171	95					105228	241				
	23	233	175	98					106347	242				
	23,5	238	178	100					107454	243				
	24	243	182	102					108548	245				
	24,5	248	186	104					109630	246				
	25	253	190	106					110701	247				
	25,5	258	194	108					111761	248				
	26	263	197	110					112811	249				
	26,5	272	204	105					116790	251				
	27	278	208	107					117776	252				
	27,5	283	212	109					118753	253				
	28	288	216	111					119720	254				
	28,5	293	220	113					120677	255				
	29	298	224	115					121625	256				
	29,5	303	227	117					122564	257				
	30	308	231	119					123495	258				
	30,5	314	235	121					124417	259				
	31	319	239	122					125331	260				
	31,5	324	243	124					126236	261				
	32	329	247	126					127134	262				
	32,5	334	251	128					128024	263				
	33	339	254	130					128907	264				
D$_R$=80%	33,5	344	258	132	18,2	1,86	0,45	114400	129782	264	265	11	3,01	0,011
	34	350	262	134					130650	265				
	34,5	355	266	136					131511	266				
	35	360	270	138					132366	267				
	35,5	365	274	140					133213	268				
	36	370	278	142					134054	269				
	36,5	375	281	144					134889	270				
	37	380	285	146					135717	270				
	37,5	386	289	148					136540	271				
	38	391	293	150					137356	272				
	38,5	396	297	152					138166	273				
	39	401	301	154					138971	274				
	39,5	406	305	156					139770	274				
	40	411	308	158					140563	275				
	40,5	416	312	160					141351	276				
	41	421	316	162					142134	277				

Table A.19: Calculation of the average shear wave velocity, maximum element size and maximum time step for the hydraulic fill with $D_R = 30\%$ and for the whole soil column.

Calculation of CRR$_{7.5}$

The CRR in Figure 2.14a can analytically be expressed by the following equation proposed by Rauch (1998) (Youd & Idriss, 2001):

$$CRR_{7.5} = \frac{1}{34 - (N_1)_{60}} + \frac{(N_1)_{60}}{135} + \frac{50}{[(10 \cdot (N_1)_{60}) + 45]^2} - \frac{1}{200} \quad (A.1)$$

Calculation of r$_d$

The stress reduction coefficient r_d is unity at surface and reduces with depth to account for the subsurface ability to deform. The variations of r_d with depth for earthquakes of different magnitude are depicted in Figure 2.8 based on expressions proposed by (Idriss, 1999):

$$r_d = exp[a(z) + \beta(z) \cdot M] \quad (A.2)$$

$$a(z) = -1.012 - 1.126 \sin\left(\frac{z}{11.73} + 5.133\right) \quad (A.3)$$

$$\beta(z) = 0.106 + 0.118 \sin\left(\frac{z}{11.28} + 5.142\right) \quad (A.4)$$

K$_\alpha$ correction factor
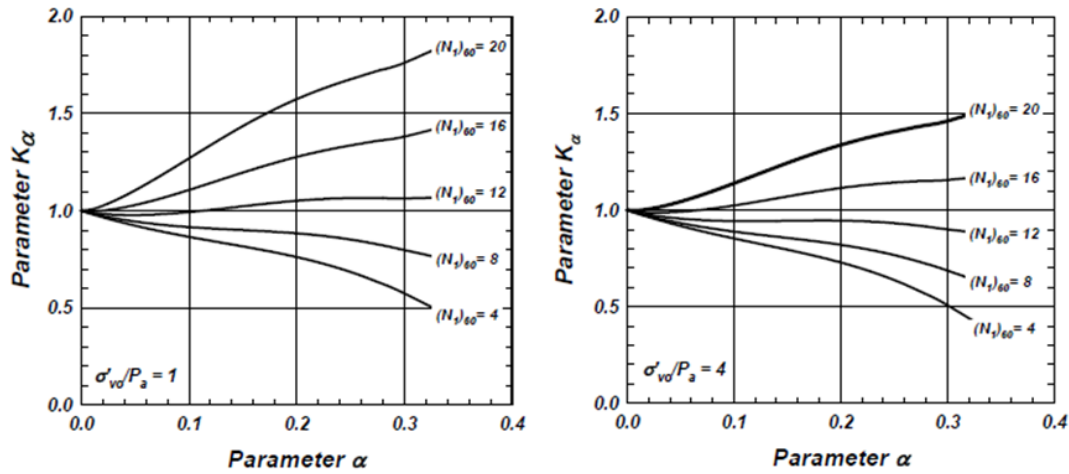
Figure A.20: K$_\alpha$ factor for sands of different relative densities and overburden stresses for an increasing static shear stress ratio (Boulanger, 2003a)

Moreover, Boulanger (2003a) introduced the following relationship to capture these effects:

$$K_a = a + be^{\frac{-\xi_R}{c}} \quad (A.5)$$

$$a = 1267 + 636a^2 - 634e^a - 632e^{-a} \quad (A.6)$$

$$b = e^{-1.11 + 12.3a^2 + 1.31ln(a+0.0001)} \quad (A.7)$$

$$c = 0.138 + 0.126a + 2.52a^3 \quad (A.8)$$

where a is the static shear stress ratio, ξ_R is the relative state index which is further elaborated in Chapter 2.8.2.

Correlation between CRR from lab tests to field conditions

$$CRR_{(K_o \neq 1)} = \frac{1 + 2K_o}{3} CRR_{(K_o = 1)} \qquad (A.9)$$

$$CRR_{SS} = \left(\frac{1 + 2(K_o)_{SS}}{3}\right) CRR_{TX} \qquad (A.10)$$

$$CRR_{field} = 0.9 \left(\frac{1 + 2(K_o)_{field}}{3}\right) CRR_{TX} \qquad (A.11)$$

$$CRR_{field} = 0.9 \left(\frac{1 + 2(K_o)_{field}}{1 + 2(K_o)_{SS}}\right) CRR_{SS} \qquad (A.12)$$

Correlation between earthquake magnitude Mw and number of equivalent stress sycles

Figure A.21: Correlation between earthquake moment magnitude M and number of equivalent stress cycles

A.3 Results for the dynamic analysis with consolidation regarding the generation of excess pore pressures

Figure A.22: Excess pore pressure ratio development in the hydraulic fill of $D_R = 30\%$ for dynamic analysis with consolidation – Comparison with the corresponding dynamic analysis without consolidation

- *(vi)* f_{fund}=5.47Hz, α_{max}=0.22g

- **k=10^{-6}m/s**

$r_u{}^{max}$	0.37	0.39	1.00	1.00	1.00	1.00	1.00

- **k=10^{-5}m/s**

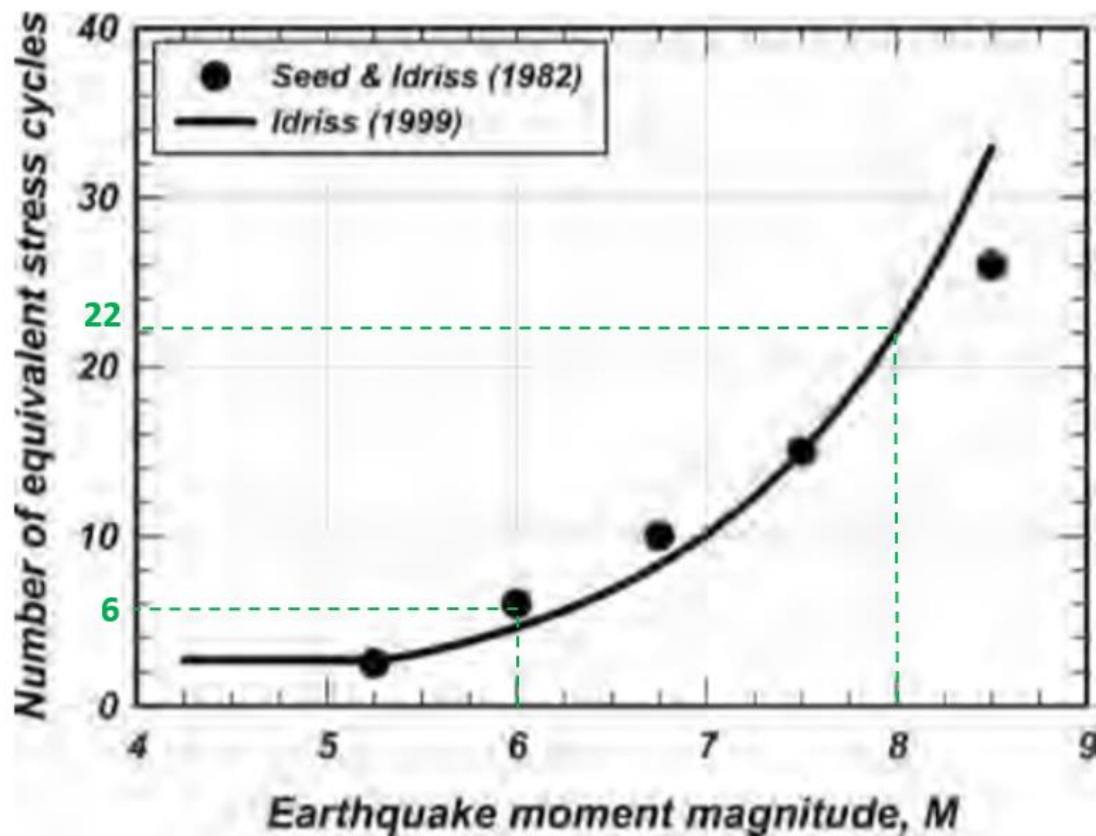| $r_u{}^{max}$	0.37	0.44	1.00	1.00	1.00	1.00	1.00	1.00	1.00	1.00

GWL
1m
D_R=30%
11m

t	11s	14s	16s	19s	22s	27s	100s

t	11s	14s	16s	19s	22s	30s	41s	49s	70s	100s

- **k=10^{-4}m/s**

$r_u{}^{max}$	0.55	0.61	1.00	1.00	1.00	1.00

- **k=10^{-3}m/s**

$r_u{}^{max}$	0.65	0.73	1.00	1.00	1.00

GWL
1m
D_R=30%
11m

t	11s	14s	16s	19s	22s	100s

t	11s	14s	16s	19s	100s

- *Dynamic analysis without consolidation*

$r_u{}^{max}$	0.21	0.27	0.30	0.89	1.00	1.00

t	22s	24s	27s	30s	32s	100s

Figure A.23: Excess pore pressure ratio development in the hydraulic fill of $D_R = 30\%$ for dynamic analysis with consolidation – Comparison with the corresponding dynamic analysis without consolidation

- *(vii)* f_{fund}=3.60Hz, α_{max}=0.14g

- **k=10^{-6}m/s**

$r_u{}^{max}$	0.20	0.31	0.36	1.00	1.00	1.00

- **k=10^{-5}m/s**

$r_u{}^{max}$	0.22	0.33	0.39	1.00	1.00	1.00	1.00

GWL
1m
D_R=30%
11m

t	24s	27s	30s	32s	57s	100s

t	24s	27s	30s	32s	35s	57s	100s

- **k=10^{-4}m/s**

$r_u{}^{max}$	0.31	0.48	0.59	1.00	1.00	1.00	1.00	1.00	1.00

- **k=10^{-3}m/s**

$r_u{}^{max}$	0.39	0.66	0.80	1.00	1.00	1.00

GWL
1m
D_R=30%
11m

t	24s	27s	30s	32s	38s	41s	57s	60s	100s

t	8s	11s	14s	16s	19s	100s

- *Dynamic analysis without consolidation*

$r_u{}^{max}$	0.26	0.36	0.47	1.00	1.00	1.00

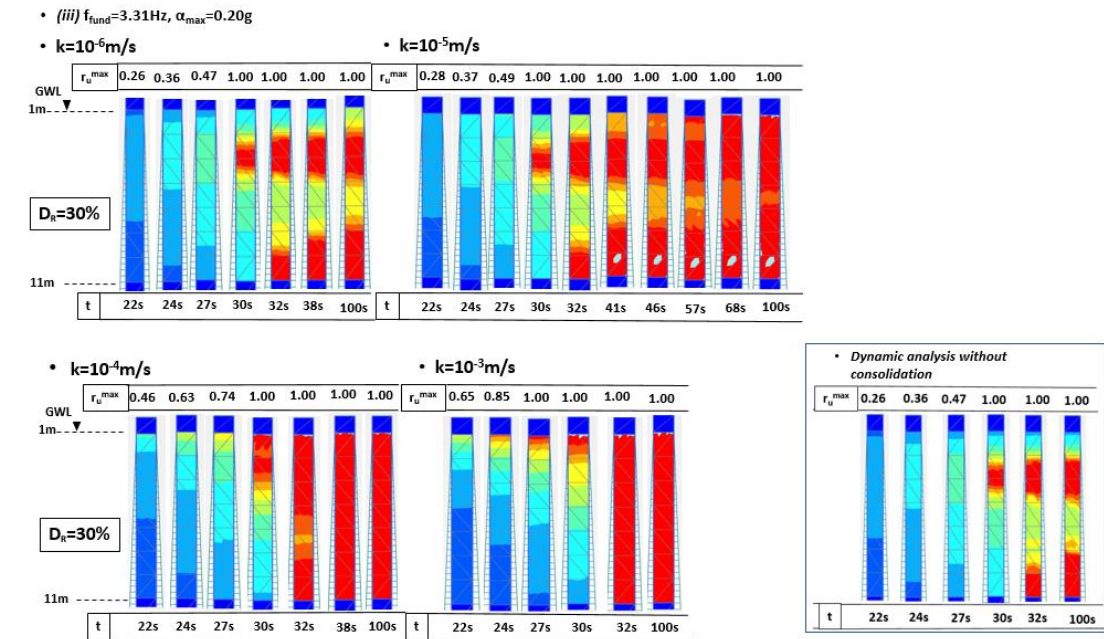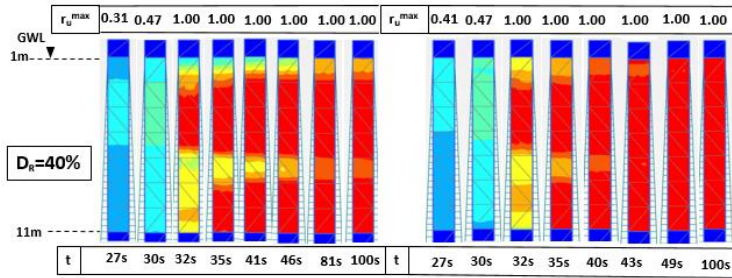| t	22s	24s	27s	30s	32s	100s

Figure A.24: Excess pore pressure ratio development in the hydraulic fill of $D_R = 30\%$ for dynamic analysis with consolidation – Comparison with the corresponding dynamic analysis without consolidation
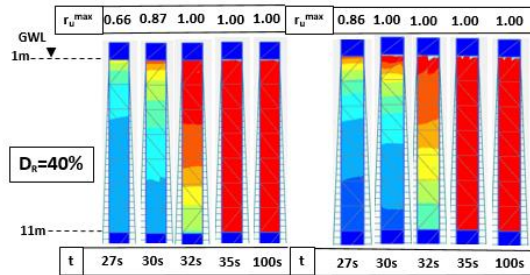
- *(iii)* f_{fund}=3.31Hz, α_{max}=0.20g

- k=10^{-6}m/s

- k=10^{-5}m/s

- k=10^{-4}m/s

- k=10^{-3}m/s

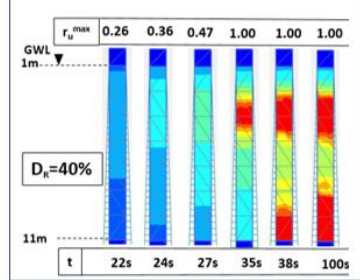- *Dynamic analysis without consolidation*

Figure A.25: Excess pore pressure ratio development in the hydraulic fill of $D_R = 40\%$ for dynamic analysis with consolidation – Comparison with the corresponding dynamic analysis without consolidation

- *(vii)* f_{fund}=3.60Hz, α_{max}=0.16g

- k=10^{-6}m/s

- k=10^{-5}m/s

- k=10^{-4}m/s

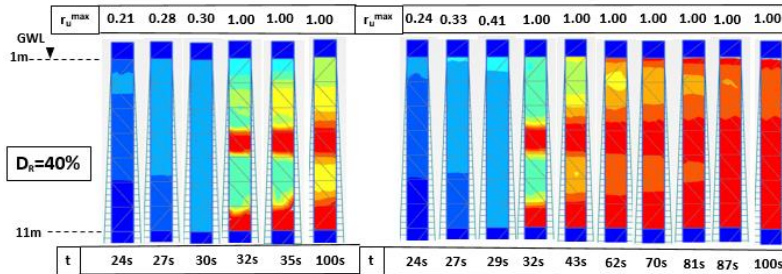- k=10^{-3}m/s

- *Dynamic analysis without consolidation*

Figure A.26: Excess pore pressure ratio development in the hydraulic fill of $D_R = 40\%$ for dynamic analysis with consolidation – Comparison with the corresponding dynamic analysis without consolidation
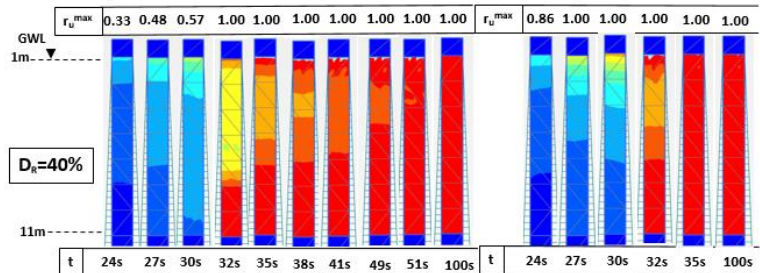
- *(iv)* f_{fund}=0.40Hz, α_{max}=0.16g

Figure A.27: Excess pore pressure ratio development in the hydraulic fill of $D_R = 50\%$ for dynamic analysis with consolidation – Comparison with the corresponding dynamic analysis without consolidation

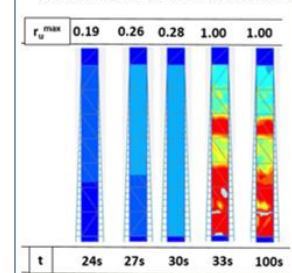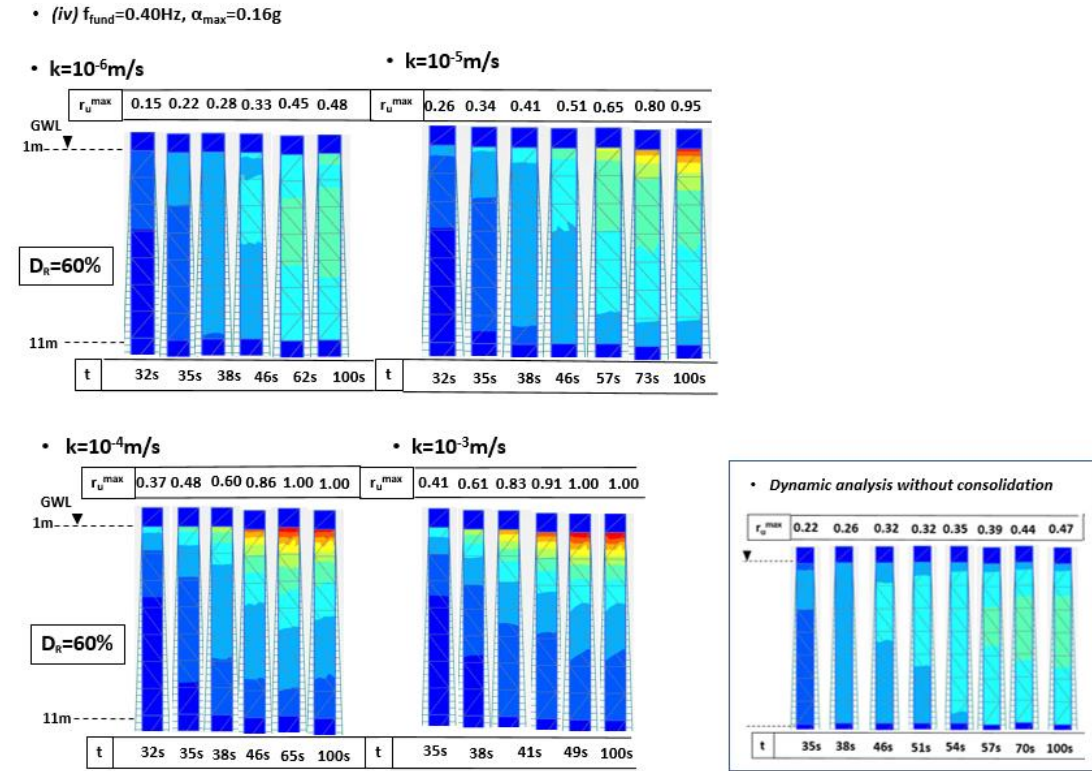- *(ii)* f_{fund}=0.37Hz, α_{max}=0.16g

Figure A.28: Excess pore pressure ratio development in the hydraulic fill of $D_R = 60\%$ for dynamic analysis with consolidation – Comparison with the corresponding dynamic analysis without consolidation

- *(iv)* $f_{fund}=0.40Hz$, $\alpha_{max}=0.16g$

- $k=10^{-6}m/s$ - $k=10^{-5}m/s$

| $r_u{}^{max}$ | 0.15 | 0.22 | 0.28 | 0.33 | 0.45 | 0.48 | $r_u{}^{max}$ | 0.26 | 0.34 | 0.41 | 0.51 | 0.65 | 0.80 | 0.95 |

GWL 1m — ∇

$D_R=60\%$

11m

| t | 32s | 35s | 38s | 46s | 62s | 100s | t | 32s | 35s | 38s | 46s | 57s | 73s | 100s |

- $k=10^{-4}m/s$ - $k=10^{-3}m/s$

| $r_u{}^{max}$ | 0.37 | 0.48 | 0.60 | 0.86 | 1.00 | 1.00 | $r_u{}^{max}$ | 0.41 | 0.61 | 0.83 | 0.91 | 1.00 | 1.00 |

GWL 1m — ∇

$D_R=60\%$

11m

| t | 32s | 35s | 38s | 46s | 65s | 100s | t | 35s | 38s | 41s | 49s | 100s |

- *Dynamic analysis without consolidation*

| $r_u{}^{max}$ | 0.22 | 0.26 | 0.32 | 0.32 | 0.35 | 0.39 | 0.44 | 0.47 |

| t | 35s | 38s | 46s | 51s | 54s | 57s | 70s | 100s |

Figure A.29: Excess pore pressure ratio development in the hydraulic fill of $D_R = 60\%$ for dynamic analysis with consolidation – Comparison with the corresponding dynamic analysis without consolidation

APPENDIX B

Dafalias & Manzari, 2004 - Model Formulation

B.1 Elastic/Plastic part

In the triaxial formulation (Dafalias & Manzari, 2004), the elastic and plastic strain increments are given by the following equations:

$$d\varepsilon_q^{el} = \frac{dq}{3G}, \qquad d\varepsilon_v^{el} = \frac{dp'}{K} \qquad (B.1)$$

$$d\varepsilon_q^{pl} = \frac{d\eta}{H}, \qquad d\varepsilon_v^{pl} = d|d\varepsilon_q^{pl}| \qquad (B.2)$$

where G is the elastic shear modulus, K is the elastic bulk modulus, H is the plastic modulus and d is the dilatancy which will be described later on.
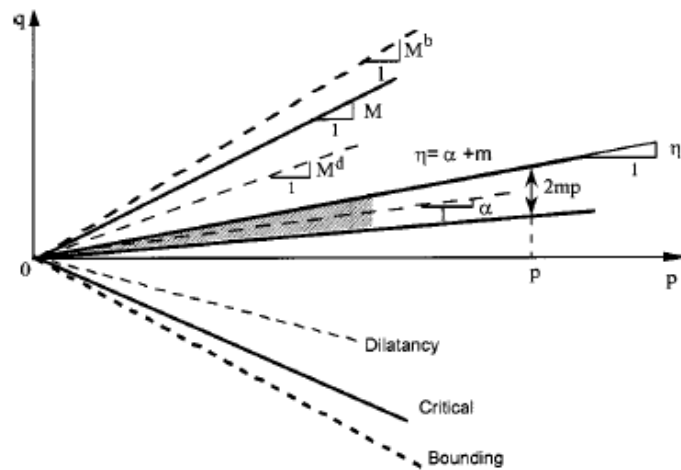

Figure B.1: Schematic illustration of yield, bounding and dilatancy lines in the q-p space

The parameters G and K are dependent on both the current stress state and the density of the soil according to:

$$G = G_o p_A \sqrt{\frac{p}{p_A}} \cdot \frac{(2.97 - e)^2}{1 + e} \qquad (B.3)$$

$$K = \frac{2(1 + v)}{3(1 - 2v)} G \qquad (B.4)$$

where p is the current means stress and e is the void ratio. Moreover, G_o is a constant, v is the Poisson's ratio and p_A is the atmospheric pressure. It is clear that e.g for dense sands, a lower void ratio (e) results in a higher value of G in eq.(B.3) which through eq.(B.4) gives a larger bulk modulus K.

B.2 Critical state behaviour

The soil at critical state is described by the following relation (Li & Wang, 1998):

$$e_c = e_o - \lambda_c \left(\frac{p_c}{p_A}\right)^{\beta} \qquad (B.5)$$

where e_c is the void ratio at critical state and λ_c, β are constants.

The state parameter Ψ which represents a generalization of the current state with respect to the critical state is introduced by (Been & Jefferies, 1985) as:
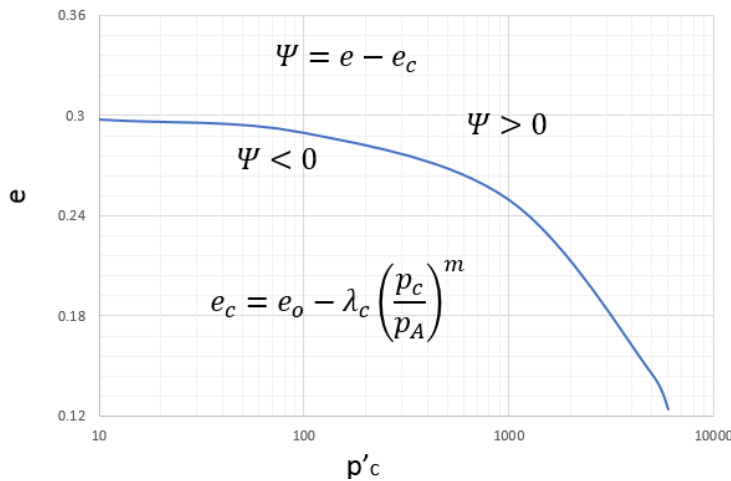
$$\Psi = e - e_c \qquad (B.6)$$

Figure B.2: Demonstration of the critical state line (Li & Wang, 1998).

In general, loose sands have Ψ>0 and may be susceptible to liquefaction whereas dense sands have Ψ<0 and are less prone to liquefaction.

B.3 Bounding, Dilatancy & Critical surfaces

The model embodies bounding (M^b), dilatancy (M^d) and critical surfaces (M) (Figure B.1). During the loading process the quantities M^b and M^d are varying with the material state in order to have $M^b = M^d = M = 0$ when $e = e_c$. Moreover, for a denser-than-critical state ($\Psi < 0$) one has $M^d < M < M^b$ while for a looser-than-critical state ($\Psi > 0$) one has $M^d > M > M^b$. This can be seen from the following expressions (Li & Dafalias 2000):

$$M^b = Mexp(-n^b\Psi) \qquad (B.7)$$

$$M^d = Mexp(n^d\Psi) \qquad (B.8)$$

where n^b, n^d are constants. It is clear that, from eq.(B.7) and eq.(B.8) as $\Psi \to 0 => M^b, M^d \to M$.

The bounding surface (M^b) represents the onset of softening behaviour and the progressive soil shearing towards critical state. In dense sands, the stress state is reaching the bounding surface to represent the explicit peak in hardening which is followed by sudden softening. On

the other hand, in loose sands, the bounding surface lies on or close to the critical surface (M) so as to show hardening behaviour towards failure without any dilation.

The dilatancy surface (M^d) represents the boundary between contractive and dilative volumetric behaviour, also called as phase transformation line (PT). In dense sands, this surface lies below the critical surface (M) in which the dilation leads to a peak behaviour. On the other hand, in loose sands, the dilatancy surface lies close or on to the critical surface because there is no dilation.

The critical state surface (M) represents the stress ratio at which $= e_c$ $(\Psi = 0)$. After this state is reached, the soil deforms continuously under constant volume.

B.4 Yield surface

The yield surface is defined by the following equation:

$$f = |\eta - a| - m = 0 \qquad (B.9)$$

which represents a wedge in the $q - p$ space (Figure B.1). The parameters a and m stand for the center and the size of the yield surface respectively.

B.5 Plastic modulus & Hardening/Softening rule

The plastic modulus H depends on the difference between the bounding stress ratio (M^b) and the current stress ratio (η) according to the following equation:

$$H = h(M^b - \eta) \qquad (B.10)$$

which represents triaxial loading in compression. In triaxial extension, the plastic modulus is rewritten as $H = h(M^b + \eta)$.

The hardening coefficient h is given by the following equation:

$$h = \frac{b_o}{|\eta - \eta_{in}|}, \qquad b_o = G_o h_o (1 - c_h e) \left(\frac{p}{p_A}\right)^{-1/2} \qquad (B.11)$$

Moreover, h_o and c_h are scalar parameters, η_{in} is the value of η at the beginning of loading and is updated when a loading reversal occurs. It is clear that e.g for dense sands, a lower void ratio (e) results in a higher value of b_o which through eq.(B.11)$_1$ gives a larger plastic modulus H in eq.(B.10).

According to the dilatancy theory (Rowe, 1962), the dilatancy (d) is determined by the 'distance' of the dilatancy stress ratio (M^d) and the current stress ratio (η) as:

$$d = A_d(M^d - \eta) \qquad (B.12)$$

where A_d is a function of state. In triaxial extension, the dilatancy is rewritten as $d = h(M^b + \eta)$.

If $(M^d - \eta) < 0$, d is also negative and plastic volumetric dilation occurs. If $(M^d - \eta) > 0$, d is also positive and plastic volumetric contraction occurs.

The hardening, softening and failure responses are represented through the plastic modulus H in which $H > 0$, $H < 0$ and $H = 0$ respectively in eq.(B.10). For example, when $\eta > M^b$, softening response occurs with the current stress-ratio η moving outside the bounding surface. This results in negative $(M^b - \eta)$ as the bounding surface contracts until critical state is reached whereby $\eta \to M^b \to M$ as $\Psi \to 0$.

B.6 Effective stress reduction due to increased dilatancy

After decomposing the total volumetric strain into elastic and plastic part for undrained loading:

$$d\varepsilon_v = d\varepsilon_v^{el} + d\varepsilon_v^{pl} = 0 \xrightarrow{(2.27)_2 ,(2.28)_2}$$

$$\frac{dp'}{K} + d\left|d\varepsilon_q^{pl}\right| = 0 \xrightarrow{(2.28)_1} \frac{dp'}{K} + d\left|\frac{d\eta}{H}\right| = 0 =>$$

$$dp' = -d\left|\frac{d\eta}{H}\right| K \qquad (B.13)$$

APPENDIX C

PM4Sand Model Formulation

C.1 Critical State Soil Mechanics Framework

The PM4Sand model is implemented according to critical state soil mechanics framework (Bolton, 1986). In this formulation, the relative state parameter ξ_R (Boulanger, 2003a) is used instead of the parameter Ψ (Been & Jefferies, 1985). The ξ_R is the state parameter Ψ in eq.(B.6) normalized by the difference between the maximum void ratio (e_{max}) and the minimum void ratio (e_{min}) that are used to define relative density (D_R). This provides improved correlation regarding the shearing behaviour of sands (Konrad, 1988).

The idea behind using the concept of relative state parameter ξ_R (defined in terms of relative density) instead of the parameter Ψ (defined in terms of void ratio) is straightforward. For a geotechnical engineer it is more convenient to refer to relative density (D_R) rather than void ratio (e) in order to distinguish between loose and dense sands.

The determination of the CSL requires extended experimental data along with the e_{max}, e_{min} and the in-situ void ratio. Moreover, in this formulation, the out-of-plane stress is ignored in the calculations (e.g of the mean stress) which makes the realistic representation of the CSL complicated.

Therefore, the critical state line is 'empirically' determined according to the following equation:

$$D_{R,CS} = \frac{R}{Q - ln\left(100\frac{p'}{p'_A}\right)} \qquad (C.1)$$

The relative state parameter ξ_R is simply defined as the difference between the relative density at critical state ($D_{R,CS}$) and the current relative density (D_R) as:

$$\xi_R = D_{R,CS} - D_R \qquad (C.2)$$

Regarding eq.(C.1) and eq.(C.2): p' is the current mean effective stress and p_A is the atmospheric pressure. The parameters Q and R were shown by (Bolton, 1986) to be about 10 and 1.0 respectively, for quartzitic sands. The parameter Q defines the mean stress level at which the CSL shifts sharply downwards due to considerable particle crushing (Boulanger, 2003a). By increasing the value of R to 1.5 a better approximation is provided for Direct Simple Shear (DSS) tests (Boulanger & Ziotopoulou, 2015). An example of the critical state line in the D_R-p plane with the parameters $Q = 10$ and $R = 1.5$ and the effect of changes in Q and R on the critical state line are illustrated in Figure C.1a and Figure C.1b correspondingly.
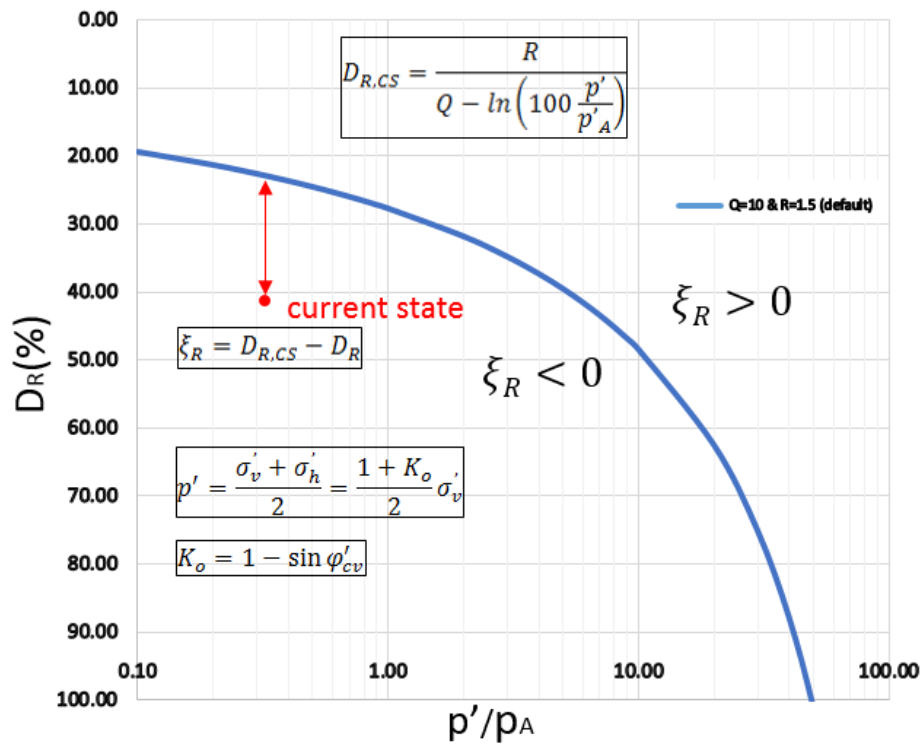
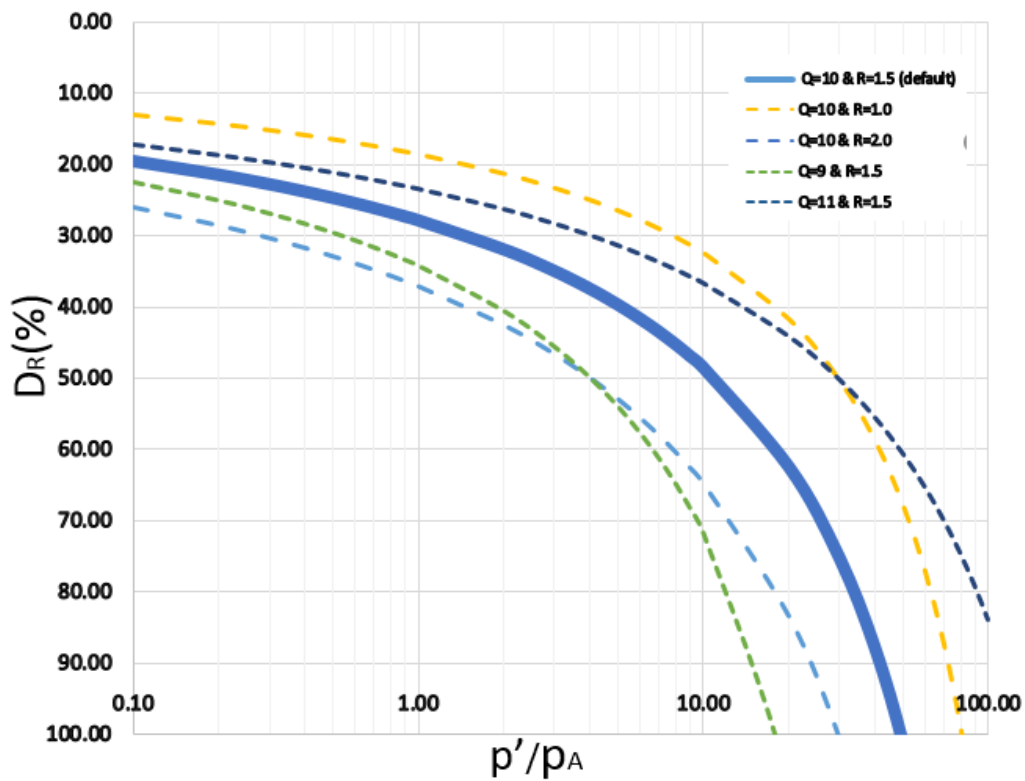Figure C.1 a: Illustration of the CSL in the D_R-p' space for Q=10 and R=1.5

Figure C.1 b: Influence of Q and R on the position of the CSL

C.2 Bounding, Dilatancy and Critical Surfaces

The model incorporates bounding, dilatancy and critical surfaces following the form (Dafalias & Manzari, 2004). The bounding M^b, dilatancy M^d and critical state M ratios are given by the following formulas:

$$M^b = M exp(-n^b \xi_R) = 2 \sin(\varphi_{peak}) \qquad (C.3)$$

$$M^d = M exp(n^d \xi_R) = 2 \sin(\varphi_d) \qquad (C.4)$$

$$M = 2 \sin(\varphi_{cv}) \qquad (C.5)$$

where φ_{peak} is the peak friction angle, φ_d is the friction angle at the onset of dilatancy, φ_{cv} is the critical state effective friction angle, M^b is the value of $r = s/p$ at peak strength, M^d is the value of r at the onset of dilation, M is the value of r at critical state strength.

The parameters M^b and M^d are defined by the model parameters n^b and n^d in relation to M. During shear loading, $\xi_R \to 0$ (shearing towards critical state line) while $M^b, M^d \to M$.

C.3 Yield Surface

The yield surface is illustrated as a small cone in the deviatoric stress space (Figure C.2)$_2$ and is formulated as:

$$f = \sqrt{(s - p\alpha):(s - p\alpha)} - \sqrt{1/2}\, pm = 0 \qquad (C.6)$$

The back-stress ratio tensor α denotes the centre of the yield surface in the deviatoric stress ratio space and the parameter m defines the size of the yield surface. The above expression can be rewritten in terms of stress ratio (r) as:

$$f = \sqrt{(r - \alpha):(r - \alpha)} - \sqrt{\frac{1}{2}}\, m = 0 \qquad (C.7)$$

In that way, the yield function can be visualized as the distance between the stress ratio r and the back-stress ratio α (Figure C.2)$_2$. In the current simplified model, the stresses from multiaxial formulation (chapter 2.7.2) are generalized in terms of in-plane stress as:

$$\boldsymbol{\sigma} = \begin{pmatrix} \sigma_{xx} & \sigma_{xy} \\ \sigma_{xy} & \sigma_{yy} \end{pmatrix} \qquad (C.8)$$

$$p = \frac{\sigma_{xx} + \sigma_{yy}}{2} = \frac{1 + K_o}{2}\sigma_{yy} \qquad (C.9)$$

$$\boldsymbol{s} = \boldsymbol{\sigma} - p\boldsymbol{I} = \begin{pmatrix} \sigma_{xx} - p & \sigma_{xy} \\ \sigma_{xy} & \sigma_{yy} - p \end{pmatrix} \qquad (C.10)$$

$$\boldsymbol{r} = \frac{\boldsymbol{s}}{p} = \begin{pmatrix} \dfrac{\sigma_{xx} - p}{p} & \dfrac{\sigma_{xy}}{p} \\ \dfrac{\sigma_{xy}}{p} & \dfrac{\sigma_{yy} - p}{p} \end{pmatrix} \qquad (C.11)$$
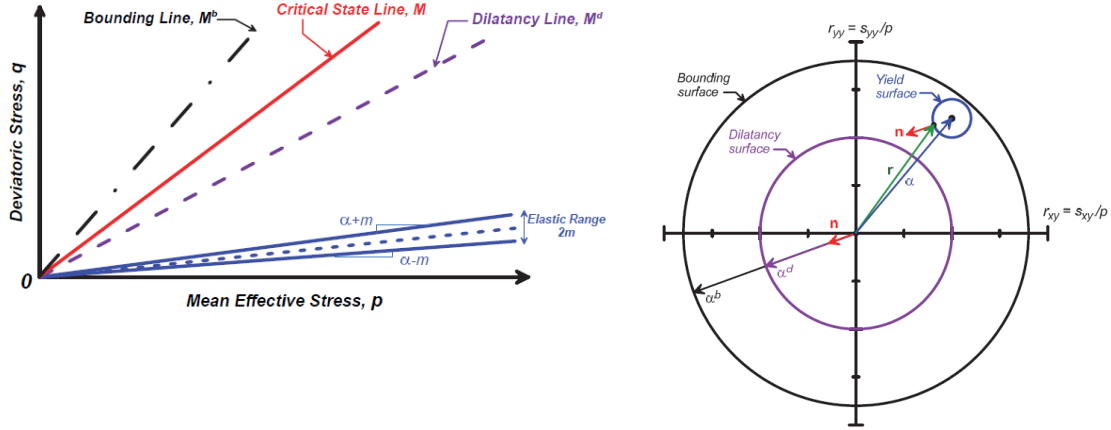
Figure C.2: Illustration of bounding, critical, dilatancy and yield lines for a dense-of-critical state in q-p' space (left) (Dafalias & Manzari, 2004) and in r_{xy}-r_{yy} stress-ratio space (right) (Boulanger & Ziotopoulou, 2015).

The bounding and dilatancy surfaces (Appendix B.3) are defined in terms of the image back-stress ratios α^b and α^d as:

$$\alpha^b = \sqrt{\frac{1}{2}}[M^b - m]\boldsymbol{n} \qquad (C.12)$$

$$\alpha^d = \sqrt{\frac{1}{2}}[M^d - m]\boldsymbol{n} \qquad (C.13)$$

where $\boldsymbol{n}$ denotes the deviatoric unit normal to the yield surface as:

$$\boldsymbol{n} = \frac{\boldsymbol{r} - \boldsymbol{\alpha}}{\sqrt{\frac{1}{2}}m} \qquad (C.14)$$

C.3 Fabric effects

The fabric-dilatancy tensor proposed by (Dafalias & Manzari, 2004) in eq.(2.29) is modified for the present model as:

$$d\boldsymbol{z} = -\frac{c_z}{1 + \langle\frac{z_{cum}}{2z_{max}} - 1\rangle}\frac{\langle-d\varepsilon_v^{pl}\rangle}{D}(z_{max}\boldsymbol{n} + \boldsymbol{z}) \qquad (C.15)$$

where:

$$dz_{cum} = |d\boldsymbol{z}| \qquad (C.16)$$

This modification was included so as the tensor $\boldsymbol{z}$ to evolve with plastic shear strain ($\langle-d\varepsilon_v^{pl}\rangle/D$) rather than plastic volumetric strain ($\langle-d\varepsilon_v^{pl}\rangle$) that occurs during dilation only

$(D < 0)$.   Moreover, the influence of fabric history and the cumulative fabric term are included in the present formulation.

In eq.(C.16), z_{cum} is the cumulative value of absolute changes of the fabric tensor $\mathbf{z}$ which increases with increasing plastic deviatoric strains. The rate of evolution of $\mathbf{z}$ in eq.(C.15) is decreasing with increasing values of z_{cum}, which disables the undrained cyclic stress-strain response to lock-up into a repeating stress-strain loop and enables the progressive accumulation of shear strains (Boulanger & Ziotopoulou, 2015).

C.4 Stress reversal and Initial Back-Stress ratio Tensors

The present model keeps track of the initial back stress ratio (a_{in}) in order to include the effects of loading history. This ratio is updated at the reversal in loading direction which is identified whenever the following condition holds:

$$(a - a_{in}):\mathbf{n} < 0 \qquad\qquad (C.17)$$

At the reversal, the initial stress ratio a_{in} is updated to the current one α. The initial stress ratio is subdivided into three initial stress ratios, namely the apparent (α_{in}^{app}) , true (α_{in}^{true}) and the previous initial stress (α_{in}^{p}) (eq.(C.32)). This is done in order to avoid the over-stiffening effect at small loading reversals (Boulanger & Ziotopoulou, 2015).

C.5 Elastic Components of the Model

The elastic strain increments are given by (Dafalias & Manzari, 2004) according to the following equations:

$$d\mathbf{e}^{el} = \frac{ds}{2G}, \qquad d\varepsilon_v^{el} = \frac{dp}{K} \qquad\qquad (C.18)$$

The elastic bulk modulus K is related to the shear modulus G through the Poisson's ratio v as:

$$K = \frac{2(1 + v)}{3(1 - 2v)} G \qquad\qquad (C.19)$$

The elastic shear modulus (G) is computed according to:

$$G = G_o p_A \sqrt{\frac{p}{p_A}} C_{SR} \left(\frac{1 + \frac{z_{cum}}{z_{max}}}{1 + \frac{z_{cum}}{z_{max}} C_{GD}} \right) \qquad\qquad (C.20)$$

where G_o the small strain shear modulus coefficient influenced by environmental factors, p_A is the atmospheric pressure,

It is important to note that in this formulation the elastic shear modulus G is not dependent on the void ratio (e) as initially proposed by (Dafalias & Manzari, 2004). The void ratio (e) was omitted because: i) the effects of void ratio variations in G are small relatively to the

corresponding effects of confining stress, ii) the calibration of G according to shear wave velocity profiles is accomplished by using only the constant G_o instead of using both G_o and e (Boulanger & Ziotopoulou, 2015).

Moreover, the elastic shear modulus G is dependent on stress ratio effects and fabric history. The stress ratio effects are captured by the C_{SR} factor (Yu & Richart, 1984) according to the following equation:

$$C_{SR} = 1 - C_{SR,o} \left(\frac{M}{M^b} \right)^{m_{SR}} \qquad (C.21)$$

$C_{SR,o}$ and m_{SR} are set to 0.5 and 4 internally which keeps the effect of stress ratio (r) smala on elastic modulus at low stress ratios, but lets the effect increase to a 60% reduction when the stress ratio is on the bounding surface ($r \rightarrow M^b$) (Boulanger & Ziotopoulou, 2015).

The effect of fabric history on the elastic shear modulus G is captured by the last bracketed term in eq.(C.20). As the plastic shear strains are increasing , z_{cum} is also increasing which results in the progressive degradation of the shear modulus G. This term was added to take into account progressive destruction of any minor cementation bonds with increasing plastic shear strains that resulted in a decreased G after an earthquake event (Boulanger & Ziotopoulou, 2015).

Similarly, the elastic bulk modulus K which is directly proportional to G in eq.(C.31) is also degrading with an increasing z_{cum}. This reduces the rate of strain-hardening at large shear strains after the phase transformation line is reached and enables the model to approximate the hysteretic stress-strain response of a soil as it liquefies (Boulanger & Ziotopoulou, 2015).

Moreover, C_{GD} is a factor accounting for the shear modulus degradation at large values of z_{cum} (set internally as 2). The parameter z_{max} is calculated at the initiation of loading by considering the initial relative state parameter ξ_{Ro} as:

$$z_{max} = 0.7 exp(-6.1\xi_{Ro}) \leq 20 \qquad (C.22)$$

C.6 Plastic Components of the Model

The increment of plastic volumetric strain along with the plastic deviatoric strain increment is given as:

$$d\varepsilon_v^{pl} = \langle L \rangle D \qquad (C.23)$$

$$d\boldsymbol{e}^{pl} = \langle L \rangle \boldsymbol{R}' \qquad (C.24)$$

where L is the loading index, D is the dilatancy, **R** is the direction of d**e**^{pl}, **R'** is the deviatoric component of **R**. Under the assumption of no Lode angle dependency, the tensors **R** and **R'** are:

$$\boldsymbol{R} = \boldsymbol{n} + \frac{1}{3}D\boldsymbol{I} \qquad (C.25)$$

$$R' = R - \frac{1}{3}DI \qquad\qquad (C.26)$$

where **n** is the unit normal to the yield surface (Figure C.2). Note that, the aforementioned assumption implies also that **R'=n**.

The dilatancy D (without fabric effects) is given by the following equation:

$$D = A_{do}\left[(a^d - a):n\right] \qquad\qquad (C.27)$$

The loading index L, as derived from (Dafalias & Manzari, 2004) is:

$$L = \frac{1}{K_p}\frac{\partial f}{\partial \sigma}:d\sigma = \frac{1}{K_p}[n:ds - n:rdp] =$$

$$= \frac{2Gn:de - n:rKd\varepsilon_v}{K_p - 2G - KDn:r} \qquad\qquad (C.28)$$

where K_p is the plastic modulus.

By using the calculated loading index, the stress increment can be calculated as:

$$d\sigma = 2Gde + Kd\varepsilon_v I - \langle L\rangle\langle 2Gn + KDI\rangle \qquad\qquad (C.29)$$

Plastic Modulus & Hardening/Softening rule

This model accounts for hardening and softening by kinematic rotation of the yield surface in the stress space. This rotation is accomplished by updating the back-stress ratio (a) which defines the centre of the yield surface.

The evolution of the back-stress-ratio $d\alpha$ is given:

$$d\alpha = \langle L\rangle\frac{2}{3}h(a^b - a) \qquad\qquad (C.30)$$

where h is the hardening coefficient.

The plastic modulus is modified in this formulation and given by the following equation:

$$K_p = Gh_o \frac{\sqrt{(a^b - a):n}}{\left[exp\left((a - a_{in}^{app}):n\right) - 1\right] + C_{\gamma 1}} C_{rev}$$

$$\cdot \frac{C_{ka}}{1 + C_{kp}\left(\frac{Z_{peak}}{Z_{max}}\right)\langle(a^b - a):n\rangle\sqrt{1 - C_{zpk2}}} \qquad (C.31)$$

where:

$$C_{rev} = \frac{(a - a_{in}^{app}):n}{(a - a_{in}^{true}):n} \quad for \quad (a - a_{in}^{app}):n \le 0$$

$$\text{otherwise} \qquad C_{rev} = 1 \qquad (C.32)$$

The main difference compared to (Dafalias & Manzari, 2004) is that the plastic modulus degradation is directly dependent on fabric changes instead of effective stress reduction in eq.(B.11) as a result of increased dilatancy through eq.(2.30). In particular, the last term in eq.(C.34) causes a reduction in K_p whenever the fabric is favorable ($\mathbf{z}:n > 0$) and for increasing plastic shear strains.

Similarly to (Dafalias & Manzari, 2004), the plastic modulus K_p is proportional to G and to the distance between the current stress state (α) and its image on bounding surface (a^b) and inversely proportional to the difference between α and the initial back stress ratio a_{in}^{app} (eq.(C.31)).

The initial back-stress ratio a_{in} is varying between the apparent back-stress ratio a_{in}^{app} and the true back-stress ratio a_{in}^{true} through the parameter C_{rev} in order to avoid the over-stiffening of the stress-strain response. In particular, the response is stiffer when $a_{in} = a_{in}^{true}$ (larger K_p) while a softer response is the case when $a_{in} = a_{in}^{app}$ (lower K_p). In this way, the model allows for the reloading stiffness to be larger ($a_{in} = a_{in}^{true}$) until the stress state exceeds the previous initial back-stress ratio ($a_{in} = a_{in}^{app}$) to avoid the over-stiffening effect (Boulanger & Ziotopoulou, 2015).

The parameter h_o is used to adjust the ratio between plastic and elastic modulus. This parameter is internally set as a function of apparent relative density D_{Ro} as:

$$h_o = \frac{(0.25 + D_{Ro})}{2} \geq 0.3 \qquad (C.33)$$

The parameter $C_{\gamma 1}$ is a constant which is set as $h_o/200$ to avoid division by zero.

Plastic volumetric contraction

Plastic volumetric contraction occurs whenever $(a_d - a):n > 0$. Then from eq.(C.27), D is also positive and given by the following equation:

$$D = A_{dc}[(a - a_{in}):n + C_{in}]^2 \frac{(a^d - a):n}{(a^d - a):n + C_D} \qquad (C.34)$$

$$with \quad D \leq 1.5 A_{do} \frac{(a^d - a):n}{(a^d - a):n + C_D} \qquad (C.35)$$

The effect of fabric on plastic volumetric contraction is captured by the following expression:

$$A_{dc} = \frac{A_{do}(1 + \langle \mathbf{z}:n \rangle)}{h_p C_{dz}} \qquad (C.36)$$

where A_{dc} is increasing with the evolution of z and therefore enhancing the plastic volumetric contraction.

Moreover, C_D is set internally as 0.16, C_{in} is increasing with the evolution of z to enhance the contraction rate at the start of an unloading cycle and C_{dz} improves modelling of the cyclic strength of denser sands (Boulanger & Ziotopoulou, 2015).

The parameter A_{do} can be expressed according relationship to the dilatancy (Bolton, 1986) as:

$$\varphi_{peak} - \varphi_{cv} = -0.8\psi \qquad (C.37)$$

where φ_{peak} is the peak friction angle of shearing resistance, φ'_{cv} the constant volume friction angle and ψ the dilatancy angle. By further analysing eq.(2.87):

$$A_{do} = 2.5 \frac{\sin^{-1}\left(\frac{M^b}{2}\right) - \sin^{-1}\left(\frac{M}{2}\right)}{M^b - M^d} \qquad (C.37)$$

The parameter h_p is a function of the contraction parameter h_{po} and the relative state parameter ξ_R :

$$h_p = h_{po}exp(-0.7 + 7(0.5 - \xi_R)^{2,5}) \qquad for\ \xi_R \leq 0.5$$

$$h_p = h_{po}exp(-0.7) \qquad\qquad for\ \xi_R > 0.5 \qquad (C.38)$$

in which the parameter h_{po} can be calibrated to achieve specific CRR values.

From the aforementioned equations, the dilatancy D is proportional to the difference $a^d - a$, to the parameter A_{do} and to favorable fabric ($z: n > 0$) and inversely proportional to the parameter h_{po}.

Plastic volumetric dilation

Plastic volumetric dilation occurs whenever $(a_d - a): n < 0$. Then from eq.(C.27), D is also negative. In this formulation, the rotated dilatancy surface M^{dR} is introduced to capture the effect of fabric evolution on plastic volumetric dilation in order to accommodate earlier dilation at low stress ratios under certain loading paths (Boulanger & Ziotopoulou, 2015). The rotated surface (Figure C.3) is determined as:

$$M^{dR} = \frac{M^d}{C_{rot1}} \qquad (C.39)$$

$$\alpha^{dR} = \sqrt{\frac{1}{2}}[M^{dR} - m]\boldsymbol{n} \qquad (C.40)$$

where C_{rot1} is a function of fabric and loading reversals.

Then the dilatancy D is calculated in two different ways: for rotated dilatancy surface and for non-rotated dilatancy surface according to:

$$D_{rot} = A_d \frac{\langle -\boldsymbol{z}:n \rangle}{\sqrt{2}z_{max}} \cdot \frac{\left(a^{dR} - a\right):\boldsymbol{n}}{C_{DR}} \qquad (C.41)$$

$$D_{non-rot} = A_d\left(-\langle -\left(a^d - a\right):\boldsymbol{n}\rangle\right) \qquad (C.42)$$

$$if \ D_{non-rot} < D_{rot} => D = D_{non-rot}$$

$$else \ D = D_{non-rot} + (D_{rot} - D_{non-rot})\frac{\langle M^b - M^{cur}\rangle}{\langle M^b - M^{cur} + 0.01\rangle} \qquad (C.43)$$
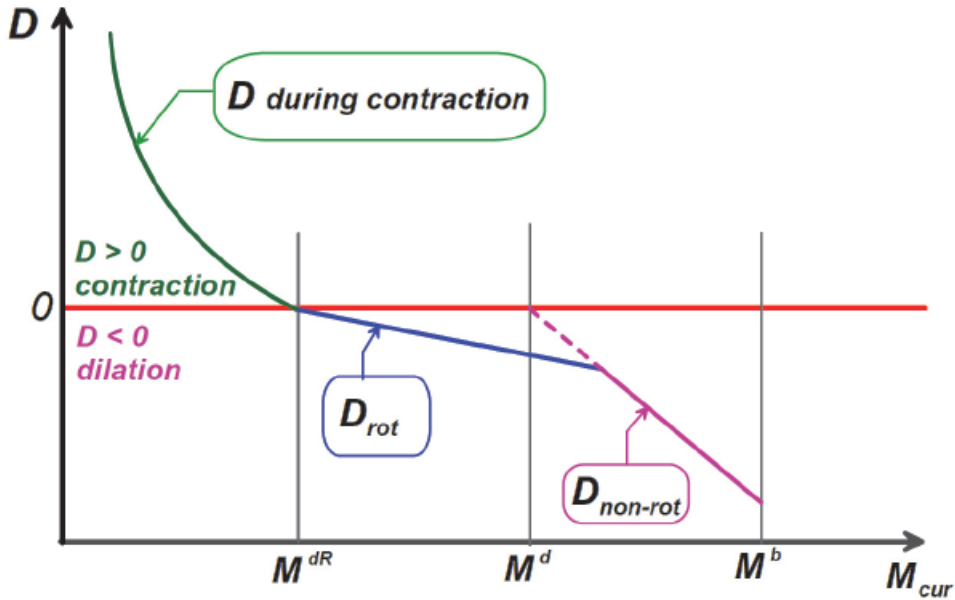

Figure C.3: Schematic illustration of the calculation of dilatancy D based on the stress state with regards to the M^{dR}, M^d and M^b surfaces during a half-cycle of loading that goes from contraction to dilation (Boulanger & Ziotopoulou, 2015).

The parameter A_d is calculated as:

$$A_d = \frac{A_{do}(C_{zin2})}{\left(\frac{z_{cum}^2}{z_{max}}\right)\left(1 - \frac{\langle -\boldsymbol{z}:n \rangle}{\sqrt{2}z_{peak}}\right)^3 (C_\varepsilon)^2 (C_{pzp})(C_{pmin})(C_{zin1}) + 1} \qquad (C.44)$$

where the first term (in the denominator) accounts for the progressive accumulation of strains under symmetric loading by decreasing the dilatancy, the second term facilitates strain-hardening when the plastic shear strain reaches the prior peak value, the third term C_ε is a calibration constant that control the rate of plastic shear strain accumulation, the fourth term C_{pzp} causes the effects of fabric on dilation to be diminished whenever the current value of p is approaching the value of p_{zp}, the fifth term C_{pmin} provides a minimum amount of shear

resistance for a soil after it has temporarily reached an excess pore pressure ratio of 100%, the sixth term C_{zin1} facilitates strain-hardening when stress reversals are not causing fabric changes (Boulanger & Ziotopoulou, 2015).

C.7 Primary Model parameters

The apparent relative density can initially be estimated from CPT or SPT correlations by the following correlations (Idriss & Boulanger, 2008):

$$D_R = \sqrt{\frac{(N_1)_{60}}{C_d}} \qquad (C.45)$$

$$D_R = 0.465 \left(\frac{q_{c1N}}{C_{dq}}\right)^{0.264} - 1.063 \qquad (C.46)$$

where D_R is expressed as a ratio rather than a percentage.

The values of C_d and C_{dq} can be taken according to (Idriss & Boulanger, 2008) as C_d=46. and C_{dq}=0.90.

In case laboratory tests are available, the relative density can be defined from the following expression:

$$D_R = \frac{e_{max} - e}{e_{max} - e_{min}} \qquad (C.47)$$

where e_{max} and e_{min} are the maximum and the minimum void ratio and e is the void ration at the current state.

The apparent relative density influences the stress-strain responses through the elastic shear modulus G in terms of stress ratio effects (C.20-C.21). In particular, D_R is directly proportional to C_{SR} (the ratio M/M^b is decreasing with an increasing D_R). Therefore, higher values of D_R will result in larger shear modulus G.

The above correlations are used to provide a reasonable estimate for the apparent D_R so that the corresponding model response is also reasonable.

The shear modulus coefficient G_0 can be calibrated to match estimated or measured shear wave velocities along a soil profile, according to:

$$G = \rho(v_s)^2 \qquad (C.48)$$

Alternatively, G_o can be related over a range of typical densities by the following expression proposed by Boulanger & Ziotopoulou (2017).

$$G_o = 167\sqrt{(N_1)_{60} + 2.5} \qquad (C.49)$$

C.8 Secondary Model Parameters

Bounding surface parameter n^b: This parameter affects the distance of the bounding surface to the critical state through eq.(C.3) and thus the rate with which the bounding surface (M^b) is approaching the critical surface (M). For a lower n^b the bounding surface lies closer to the critical surface. Consequently, the bounding surface is approaching the critical surface faster after $\mathbf{r} \rightarrow M^b$.

The bounding surface parameter controls the dilatancy and thus the peak effective friction angle. Its default value is 0.50 but for looser-than-critical states a value of $n^b/4$ is used.

Dilatancy surface parameter n^d: This parameter affects the distance of the dilatancy surface to the critical state in eq.(2.57) and represents the stress ratio ($\mathbf{r}$) in which contraction transitions to dilation. Its default value is 0.10 but for looser-than-critical states a value of $4n^d$ is used.

Atmospheric pressure p_A: Default value of 101.3 kPa is used

Maximum and minimum void ratios, e_{max} and e_{min}: Influences the computation of relative state parameter ξ_R and how volumetric strains are translated into changes ξ_R. The default values used are 0.8 and 0.5 respectively. These parameters are most likely not refined for practical problems as the calibration of other parameters will have a bigger impact on monotonic or cyclic strengths.

Critical state friction angle ϕ'_{cv}: Defines the position of the critical surface (M) and its default value is 33°.

Poisson's ratio v: Default value of 0.3 is used

Critical state line parameters Q and R: These parameters determine the critical state line in Figure 2.27 through eq.(2.48). Default values of 10 and 1.5 are used respectively to better approximate Direct Simple Shear (DSS) tests results (Boulanger & Ziotopoulou, 2015).